

https://dspace.org/

Sedimentology and geochronology of the fossil bearing upper member of Malapa site in the Cradle of Humankind (South Africa, Johannesburg)

Maphanda, Dakalo Portia

2023-08

University of the Witwatersrand, Johannesburg

https://hdl.handle.net/10539/41787

Maphanda, Dakalo Portia. (2023). Sedimentology and geochronology of the fossil bearing upper member of Malapa site in the Cradle of Humankind (South Africa, Johannesburg). [Master's dissertation, University of the Witwatersrand, Johannesburg]. https://hdl.handle.net/10539/41787

Downloaded from a DSpace repository. https://dspace.org/

Sedimentology and geochronology of the fossil-bearing upper member of Malapa site in the Cradle of Humankind (South Africa, Johannesburg)

Dakalo Portia Maphanda

ORCID ID: 0000-0003-0693-1837



Dissertation submitted to the Faculty of Science, University of the Witwatersrand, Johannesburg, South Africa in fulfillment of the requirements for the degree of Master of Science in Palaeontology

in

Geology

Supervisor: Dr Zubair Jinnah

Co-supervisor: Dr Tebogo Vincent Makhubela and Dr Paloma de la Peña

Evolutionary Studies Institute, University of the Witwatersrand, Private Bag 3, WITS 2050, Johannesburg, South Africa.

August 2023

DECLARATION

I know plagiarism (using someone else's work without their permission and /or without acknowledging the original source) is wrong.

I declare that this dissertation is my own, unaided work except where I explicitly indicated otherwise. This dissertation is being submitted for the Degree of Master of Science in Palaeontology at the University of the Witwatersrand, Johannesburg. It has not been submitted before for any degree or examination at any other University. I have followed the required conventions in referencing the thoughts and ideas of others.

Signature: Dakalo P. Maphanda **Date:** 2023/08/19

ACKNOWLEDGEMENT

Firstly, I would like to thank God for the spiritual strength to finish this dissertation. Without God, I would not have made it to this final stage. I would like to thank my supervisors Dr Paloma de la Peña, Dr Zubair Jinnah, and Dr Tebogo Makhubela. Thank you, Paloma, for your unrelenting guidance and support, you continually cared about me and my work, which gave me the confidence to finish the dissertation. Thank you Tebogo and Zubair for the scientific knowledge advancement and swift feedback. My sincere gratitude to you Tebogo for investing the time in the SEM-EDS training and guidance. Thank you, Zubair for entertaining my random office visits to discuss the project and giving me ideas.

I am grateful to the University of the Witwatersrand and the University of Johannesburg technical staff for making thin sections used in this study. I would like to thank Mr Louis Mudalahothe for training me to use Earthlab to crush and prepare XRF samples. I would like to extend my gratitude to the University of Johannesburg Spectrum Analytical Services staff for assistance with sample preparation and measurement for X-ray fluorescence and scanning electron microscopy.

I would like to thank Robert Bolhar for his immeasurable help with the LA-ICP-MS measurement and data reduction, I could not have done this without his help. I would also like to thank Dr Stephan Winkler at the Accelerator mass spectrometry (AMS) and isotope research, Helmholtz-Zentrum Dresden-Rossendorf, Germany for the cosmogenic nuclide burial dating sample processing and beryllium-10 (^{10}Be) and aluminium-26 (^{26}Al) measurements on the AMS.

I would like to greatly appreciate my friends and family. They kept me sane with long phone calls, lunches and simply listening to my rambles. Thank you, Bibi Ayesha Jogee, for not only being a friend to me but being my academic peer consultant and teaching me software tricks to make my

work go faster. You kept me laughing, motivated, and happy and I am deeply grateful for that. I would like to thank all the geoscience postgraduates I encountered in the past two years and had a laugh with, those moments didn't go unnoticed.

Lastly, I would like to thank the National Research Foundation and the DSI-NRF Centre of Excellence in Palaeosciences for the financial assistance provided to finish this project.



ABSTRACT

Malapa is a palaeoanthropological site in the Cradle of Humankind in South Africa. It is known for preserving two partial skeletons of *Australopithecus sediba*. These skeletons are encased in Pleistocene cave deposits that are subdivided into six sedimentary facies i.e., A-F. There are two pits exposed at the site i.e., the main pit (pit 1) and pit 2. Sedimentary facies A-E are deposits from the main pit, and facies F occurs in both pit 1 and 2. Pit 2 deposits were previously classified as a homogenous deposit of facies F. Recent excavation campaigns carried out in 2019 and 2020 exposed new deposits adjacent to the deposits in pit 2. The purpose of this study was to enhance the geological understanding of the deposits at Malapa by investigating the newly exposed deposits. We found that facies F deposits are not as homogenous as previously thought, based on grain size, textural variation, and general appearance of the deposit. The newly exposed deposits and facies F were collectively called the upper member as they entail the deposits investigated in this study. Facies F and the newly exposed deposits were then targeted for sampling to investigate the petrography of the deposits. The study also investigated the stratigraphic position of the upper member in relation to facies A-F from the main pit by attempting to resolve an age of the deposits. The study utilized a sedimentary analysis approach by combining petrographic descriptions, mainly SEM-EDS and XRF to confirm the existence of multiple facies in the upper member. The results show that the upper member comprises facies B, C, F and a newly defined facies G. Facies G contains more chert and quartz clasts than any facies described in the previous studies. It only has calcite in the form of a micrite matrix supporting chert, quartz, or Mn-Fe-coated grains. Considering that the six facies from previous studies are chronologically well constrained, the age of facies G was also investigated. Two flowstones were used to estimate the maximum age of the clastic sediments. Flowstone 2 was situated between the clastic sediments of facies B, C and F so

it represents a maximum age for sediments below it and the minimum age for those above it. Flowstone 2 is the same as the Flowstone 2 sampled by a previous study where it returned a well-constrained age of 2.06 ± 0.021 Ma. Flowstone 3 was determined to be a clast that could have collapsed from the cave roof and was situated in previously unstudied sediments. The sediments were determined to be Facies C deposits close to Pit 1. We attempted to date Flowstone 2 by U-Pb LA-ICP-MS but attained an age of 3.72 ± 0.77 Ma (Pliocene in age), inconsistent with previous dating and unrealistic in the context of the Malapa. Flowstone 3 produced a U-Pb age of 7.50 ± 0.37 Ma (Miocene in age). The U-Pb flowstone ages have large errors. Flowstone 2 has an error of ~21% of the age and flowstone 3 has an error of ~5%. Both flowstone ages have too large an error to be considered useful to constrain the age of the upper member. A second dating approach was then used on the clastic sediments themselves using cosmogenic nuclide burial dating. The method yielded more well-constrained ages of 1.59 ± 0.44 Ma. This is an isochron burial age that suggests that the upper member is much younger than the deposits in the main pit, but the isochron burial age is in agreement with the literature U-Pb ages from the flowstones. This is because 1.59 + 0.44 = 2.03 Ma which coincide with the U-Pb ages of the flowstones in the main pit and pit 2. The age of the samples from facies G have an average age of 1.52 ± 0.088 Ma which makes facies G the youngest in stratigraphy.

TABLE OF CONTENTS

ACKNOWLEDGEMENT i

ABSTRACT i

List of tables xiv

CHAPTER 1: INTRODUCTION 1

1.1 Site description 1

1.2 Aims and research questions 4

1.3 Hypotheses 4

CHAPTER 2: STUDY BACKGROUND 9

2.1 Geological setting 9

2.2 Geological information review in the Cradle 15

2.3 Dating of deposits in the Cradle 29

CHAPTER 3: MATERIALS AND METHODS 36

3.1 Samling methods and materials 36

3.2 Petrology methods 41

3.2.1 X-ray fluorescence analysis 41

3.2.2 Scanning Electron Microscopy- Energy Dispersive Spectroscopy (SEM-EDS) 42

3.2.3 Petrography 42

3.3 Uranium lead (U-Pb) dating 43

3.4 Cosmogenic nuclide burial dating ($^{26}Al/ ^{10}Be$) 44

CHAPTER 4: PETROLOGY AND GEOCHEMISTRY RESULTS 46

4.1 Sample descriptions 46

4.2 SEM-EDS results 67

4.3 XRF analysis results 76

CHAPTER 5: GEOCHRONOLOGY RESULTS 94

5.1 Flowstone 2F 94

5.2 Flowstone 3F 96

5.3 Cosmogenic nuclide burial dating results 98

CHAPTER 6: DISCUSSION 101

6.1 Newly exposed deposits: interpretations 101

6.2 Facies G 107

6.3 Geochronology interpretations 107

6.3.1 U-Pb 107

6.3.2 $^{10}Be/^{26}Al$ 110

CHAPTER 7: CONCLUSION 111

REFERENCES 112

ANNEXURES 139

Annexure A: Analytical protocol for U-Pb-LA-ICP-MS at Wits 139

References for the protocols 141

Annexure B: Harker diagram data format 142

List of Figures

Figure 1: Geological map showing the six facies already established at Malapa and the two flowstones used for the geochronology. The map also shows the sample locations used for Uranium-lead dating and palaeomagnetic analysis (Pickering et al., 2011a)..... 2

Figure 2: Stratigraphic column of Malapa showing Facies A-F and palaeomagnetic and U-Pb results. Flowstone one underlies facies A and B preserving a normal polarity near the base and reverse polarity in all other parts. This was intepreted as the Huckleberry Ridge Subchron (Dirks et al., 2010). Facies C, D and E recorded a normal polarity and was interpreted as the beginning of Olduvai Subchron (Dirks et al., 2010).The rock types observed are grainstone and sandstone. The figure is modified from Makhubela and Mavuso (2022). See Table 1 for a detailed facies descriptions. 3

Figure 3: Photogrammetry photo of the newly exposed fossiliferous and barren deposits at Malapa. A) The newly exposed deposits and B) Pit 2 which was targeted to sample facies F. The photo shows where petrographic samples and cosmogenic nuclide samples were taken together with the two flowstones used for U-Pb dating in this study relative to the main pit. The main pit terminates by block 2 as ascribed by Pickering et al. (2011a). Photogrammetry photo credit: Paloma de la Peña. 6

Figure 4: Geographical map showing the location of the Cradle and the 12 of some of the well-studied paleoanthropological sites within the Cradle. The study area i.e., Malapa is shown by the star symbol while the rest of the sites are shown by dots. Map created by Dakalo Maphanda. 10

Figure 5: SEM image showing four types of Mn-Fe-oxyhydroxides coating as described by Makhubela (2014). A - C shows type 1, D - F shows type 2, G – I shows type 3, and J – L shows type 4. “Qtz” stands for quartz. 29

Figure 6: Photogrammetry photo of the newly exposed fossiliferous and barren deposits at Malapa. A) The newly exposed deposits and B) Pit 2 which was targeted to sample facies F. This image shows the concentration of 8 samples taken in Pit 2 and 6 samples taken in the recently excavated area (A). 36

Figure 7: Composite image showing areas where individual samples were sampled. For a 3-D visualization, revisit figure 3. A and C- are samples of MLP1F and MLP2F respectively. B, D - P are samples MLP1P, MLP2P - MLP14P and Q-S are MLPFE1, MLPFF1, and MLPFF2 respectively. Looking at images N, J and B, it is obvious that these sediments are different. N is a fine-grained deposit with dolomite blocks, J is medium-coarse grained clastic deposit and B is composed of peloids. Image created by Dakalo Maphanda. Photos cred: Paloma de la Peña..... 40

Figure 8: Flow diagram showing generalized and simplified steps of the sample preparation and processing for cosmogenic nuclide analysis (Makhubela et al., 2021). 44

Figure 9: Petrographic images of MLP1P in cross polarized light (XPL) showing the type of grains in A. B shows the blocky sparite texture cementing the micritic peloids. The peloids in this sample are semi-uniform in shape with some void spaces between them as shown in

F. In parts of the sample, the peloids start to disintegrate as shown in E. C shows a peloid grain with a nucleus that is almost rhombic. 47

Figure 10: XPL micrographs of MLP2P showing the textures in the sample. A-C shows peloidal texture with some peloids fully disintegrated to form micrite groundmass. Calcite occurs in two forms in the sample i.e., as veins (F) and as patches of blocky cement (C-D). Other grains such as chert (G, H), quartz (I) Mn-nodules(H), and aggregate grins (E) are also shown. 48

Figure 11: Petrographical images of MLP3P showing a peloidal texture, and micrite groundmass forming as peloids disintegrate (B). C-E shows in the plane polarized light micrograph, the peloid with a nucleus, the relationship between peloids and disintegrating peloids. The calcite forms a sparite cement, but it occurs as a partial isopachous matrix around and in between peloids. 49

Figure 12: Micrographs of MLP4P showing a poorly sorted sample that is predominately composed of coarse clasts of chert, quartz, Mn-Fe oxides, and a fine groundmass of micrite. A, B, and E show the grain types in ppl, and C and D show the coating of chert in XPL. ... 50

Figure 13: Petrographical images of MLP4P. This sandstone is matrix supported as shown in (C). The most abundant grain is chert and micrite clasts which are rounded and coated (D, E). The sample has voids more than the previous sample (A). Some remnant peloidal textures can be seen with quartz inclusions (I). Micrographs G & E (PPL) and A, B, C, D, F, H, I, and J (XPL). 51

Figure 14: Micrograph of MLP6P showing a binary texture. This binary sample of Calcareous sandstone as shown in A, B, and E is texturally challenging as it is made up of two phases.

Most of the grain types can only be seen at low magnification (1 mm and less) (D- K). All images (A- K) are in XPL except for E which is in PPL..... 53
Figure 15: Micrographs of MLP7P showing micrite texture. This is a fine-grained micritic limestone sample as shown in A (PPL) and B (XPL) is composed of quartz grains (C &F), calcite grains (D), and calcite cement (E)..... 54
Figure 16: Micrographs of MLP8P. This sample has the coarsest grains in all the samples as seen from A and B. This sample has no peloids, it has thin calcite veins cutting through quartz and chert grains as seen in images C and D. Calcite cement is found in between certain grains with micrite being the matrix (E). A(PPL) and B-E (XPL)..... 55
Figure 17: Micrographs of sandy limestone sample. Most of the grain textures are observed at <500 μm scale. This is where the zoning of grains can be seen (E and F). Remnants of calcite blocky cement can be seen (D) and most of the peloids are <500 μm to a millimeter in size (A, B, C, G). From the micrographs, it is clear that detrital grains such as chert are not abundant compared to chemical grains. A, C, D, and G are in XPL, and B, E, and F are in PPL. 56
Figure 18: Petrographical imges of MLP10P, the calcreous sandstone. A few Mn-Fe-oxides have completely become Mn-Fe-nodules (B) instead of just being a coat around the grains as observed in D. Even quartz and chert grains that are less than one millimeter in size are coated with the Mn-Fe-oxides. A and C are in PPL and B and D are in XPL. 57
Figure 19: Micrographs of MLP11P showing Mn-F e-oxide grain textures. MLP11P is a calcareous sandstone full of coated grains. The Mn-Fe-oxides are spherical in shape as many have become predominately Mn-nodules (A & B). In the bottom left of image F, micrite can be seen at the edges of the peloidal nodule. Calcite cement (sparite) cements all the coated

chert, quartz, Mn-Fe-oxides grains, and calcite grains. A, D, E, and F are in PPL and B & C are in XPL..... 58
Figure 20: Micrographs of MLP12P showing grain texture. MLP12P is a sandy limestone sample. Although looking at the thin section, one might be tempted to say this is a fine-grained sample because the micrite matrix is abundant. The matrix may be fine-grained, but the clasts are larger than 2 mm in most cases. Peloids in this sample are very few and can only be seen in <500 μm grain size. A is in XPL and B & C are in PPL..... 59
Figure 21: Micrographs of MLP13P. MLP13P is a poorly sorted calcareous sandstone. Calcite cement in this sample forms as patches and usually coats void spaces as can be from B and D. Chert grains in this sample are small and thinly coated (C). A, B, C, and D are in XPL and E is in PPL. 60
Figure 22: MLP14P image showing that MLP14P is a binary sample that has small peloids, although more abundant than MLP12P, they still do not compare to peloids encountered in MLP1P, MLP2P, and MLP3P in terms of grain size and sphericity. A, B, C, and D are in PPL, and E, F, G, H, I, and J are in XPL. 62
Figure 23: Composite image of MLPFE1. This figure shows the type of grains in MLPFE1. The void spaces in this sample seem to be connected (F). Compared to literature descriptions, this sample had few peloids which were so small that they were observed in a micrite clast. This sample is not well-sorted like the descriptions in the literature, it is poorly sorted. 63
Figure 24: Composite image showing texture for MLPFF1 and MLPFF2. The two samples (MLPFF1 and MLPFF2) are not fine-grained like those studied in the literature. Chert grains were the most common clast observed with little to no peloids observed in both samples. Both samples do have a detrital element by containing quartz and chert grains. 64

Figure 25: Image of sample MLP1F showing observed fabrics. MLP1F fabrics shown A (PPL) and B (XPL). 65
Figure 26: Image of MLP3F, it shows the flowstone as a plain flowstone with only one fabric identified, columnar open shown in A (PPL) and B (XPL) 66
Figure 27: SEM micrographs showing per sample what type of Mn-Fe-oxyhydroxide is in each sample. Sample MLP1P (A) and MLP7P (F) have no coated grains. MLP4P (C) shows various types of coating including type 4. Type 2 coating is depicted by MLP2P (B), and type 1 can be seen from sample MLP6P (E). 69
Figure 28: Continuation of figure 27 showing the rest of the samples and the types of coating that occur in each. From this figure, type 3 coating is observed in sample MLP8P (A) and MLPFE1 (F). Samples like MLP8P (A), MLP9P (C), MLP10P (D) and MLP14P (E) are dominated by type 2 coating. 70
Figure 29: Composite image showing EDS elementary map composite picture (A) and point and ID image (B) of sample MLP4P and MLP9P respectively. A total of seven points were picked at different “sites” in the sample targeting different grains for the elements identified (B). The resulting spectrums are shown in Figure 31. The individual element maps that show the element that is mapped per grain to produce the composite image (A) are discussed in Figure 30. 71
Figure 30: Individual elementary maps of MLP4P that make up the composite image of Figure 29A. The element picked up in MLP4P is aluminum (Al), oxygen (O), calcium (Ca), and silicon (Si), manganese (Mn), and iron (Fe). From these images, besides the high content of Si, Mn is more abundant than Fe which means the Mn-Fe-oxyhydroxides have a high content of manganese oxide than iron oxide. 73

Figure 31: The point and ID spectrums (MLP9P electron image 1, see Figure 29B) show that manganese, oxygen, iron, and aluminum are the most abundant respectively. It also shows that in coated grains, Mn weighs the most with up to 60%. 73

Figure 32: MLP4P matrix elementary maps (B- F) and composite image (A). This figure shows a vein and all the compositional elements of the vein. The vein is made primarily from calcium..... 74

Figure 33: MLP4P micrite matrix elementary maps (B-F) results including a layered image (A). 75

Figure 34: Harker diagrams of Al_2O_3 plotted against all other major oxides detected by the XRF and reported without global standards. These Harker diagrams exclude the global standards to assess the relationship between the samples individually. The legend is read as follows: The calcareous sandstones (CS), the sandy limestones (SL), the micritic limestones (ML), and the muddy limestones (ML) in yellow and peloidal limestone (PD). The samples grouped as calcareous sandstones using petrographic descriptions show an interesting distribution. The calcareous sandstones seem to be closely related by having compositions that are similar and different at the same time. MLP5P (in the blue rectangle) despite being petrographically a sandstone, chemically has more CaO% than SiO_2 and low Al_2O_3. 84

Figure 35: Harker diagrams of Al_2O_3 plotted against all other major oxides detected by the XRF and reported by global standards. All samples from this study have Al_2O_3 content of between 1- 4%. The calcareous sandstones (CS), the sandy limestones (SL), the micritic limestones (ML), and the muddy limestones (ML) in yellow and peloidal limestone (PD) all show significant depletion on all major oxides compared to the global standards. The global standards have a low CaO/Al_2O_3 ratio, MnO/Al_2O_3 ratio, and relatively low MgO/ Al_2O_3

ratio compared to this study' samples. The global standards also have a high SiO_2/ Al_2O_3 ratio, K_2O/Al_2O_3 ratio, Fe_2O_3 ratio, and TiO_2 ratio. 85
Figure 36: Harker diagrams of SiO_2 plotted against all other major oxides detected by the XRF and reported with global standards. The trend observed mostly in these Harker diagrams with SiO2 in the x-axis is a scattered trend. There isn't a strong correlation between the samples themselves and the global standards. The samples are depleted compared to global standards as can be seen from these plots as well. Notice MLP11P having the highest MnO/ Al_2O_3 of all samples and the global standards. MLP12P also contains more MgO than the global standards and the study samples. 86
Figure 37: Harker diagrams of Al_2O_3 plotted against all other major oxides detected by the XRF reported by sandstone standards. The calcareous sandstones from this study are enriched in CaO and MnO but are depleted in Al_2O_3, SiO_2, P_2O_5, MgO and K_2O.The samples do not resemble either the Average Early Proterozoic Sandstone (AEPS) or the Average Late Proterozoic Sandstone (ALPS). 88
Figure 38: Harker diagrams of SiO_2 plotted against all other major oxides detected by the XRF reported by sandstone standards. The depletion trend can be seen more clearly when SiO_2 is plotted against all other oxides. Clearly the standards have more SiO_2 than all the samples, and only have one sandstone from this study containing more MgO than them..... 89
Figure 39: Harker diagrams of Al_2O_3 plotted against all other major oxides detected by the XRF reported by Clarke and Washington (1924) average composition of shale, limestone, and sandstone standards. The diagram also reports on the average shale calculated from this data presented a s a standard by Clarke and Washington (1924). This figure shows that the study samples are more similar to limestone in terms of most oxides than the sandstone and the

two shales. In terms of TiO_2 and MgO, MnO and Fe_2O_3, the samples are more chemically similar to both sandstones and limestones. A sample that is more similar compositionally to the limestones average of Clarke and Washington (1924) is MLP1P, in all major oxides except for the MgO and P_2O_5 they are siting almost on top of each other in the diagram.... 90

Figure 40: Harker diagrams of SiO_2 plotted against all other major oxides detected by the XRF reported by Clarke and Washington (1924) average composition of shale, limestone, and sandstone standards. The study samples are depleted in SiO2 and slightly depleted in all other oxides except for CaO of which they are enriched compared to the four averages. The depletion trend is seen in both presentation of the data..... 91

Figure 41: Harker diagrams of Al_2O_3 plotted against all other major oxides detected by the XRF reported by average compositions of shale in the Cradle. Despite the standard data coming from the regional area, the samples are not chemically correlated with the standards. The study samples are depleted in Al2O3 compared to the Cradle averages. The averages show a depletion in CaO, MnO and a slight depletion in Fe_2O_3 compared to the study samples. The calcareous shales of the Malmani Subgroup (CSMG) are the most chemically different in all the data represented in this Harker diagram. 92

Figure 42: Harker diagrams of SiO_2 plotted against all other major oxides detected by the XRF reported by average compositions of shale in the Cradle. The trends are better seen when SiO_2 is the controlling factor. The three averages contains similar amounts of CaO and MnO Wt%, that is why they are sitting on top of each other..... 93

Figure 43: Image depicting the date of MLP1F which was determined using LA-ICP-MS via the isochron method. The age is 3.72 Ma with an error of ± 0.77. The MSWD is higher than 1 which means this age is overdispersed concerning the stated analytical uncertainties..... 95

Figure 44: Image showing the date of MLP2F which was determined using LA-ICP-MS via the isochron method. The age is 7.50 Ma with an error of ± 0.37. The MSWD is also greater than 1, this indicates that the ages are also overdispersed concerning the stated analytical uncertainties. 97

Figure 45: Image showing the isochron cosmogenic burial age calculated from sample MLP1CN – MLP6CN. The age is 1.59 ± 0.44 Ma. 100

Figure 46: Photogrammetry photo encompassing the upper member deposits, Pit 1 and Pit 2 at Malapa. The image shows where each sample comes from and which facies they fall under. The photo also shows where the cosmogenic samples were samples relative to the petrographic samples. Three facies already described at Malapa are present in the upper member deposits i.e., facies B, C and F. Facies G is found all over the upper member and in area A, it occurs right at the edge of the dolomitic walls. Photogrammetry photo cred: Paloma de la Peña. 103

Figure 47: Summary stratigraphic column drawn to demonstrate that facies are repeating as we approach the dolomitic walls. More than one facies was exposed at a time. 107

List of tables

Table 1: Table containing facies A- F description summary compiled using Dirks et al. (2010) and Pickering et al. (2011a). This summary details petrographic descriptions, field observations and interpretations (sedimentary environment). Facies A- F are interpreted as water-laid deposits with little post-depositional compaction indicated by loose packing of framework grains in sandstones (Dirks et al., 2010). 6

Table 2: Summary of Malmani Subgroup formations in terms of lithology and measured thickness. 11

Table 3: Summary table showing the geological formation that each site occurs in and cave-specific well-known findings. Data from: Clarke, 1977; Partridge, 1978; Brain, 1981; Berger et al., 1993; Clarke, 1994; Keyser et al., 2000; Kuman and Clarke, 2000; Susman et al., 2001; de Ruiter, 2003; Partridge et al., 2003; Pickering et al., 2007; Steininger et al., 2008; de Ruiter et al., 2009; Berger et al., 2010; Dirks et al., 2010; Pickering et al., 2011a; Adams, 2012; Gommery et al., 2012; Clarke, 2013; Herries and Adams, 2013; Herries et al., 2013; Herries et al., 2014; Adams et al., 2016; Leece et al., 2016; Braga et al., 2017; Dirks et al., 2017; Edwards et al., 2019; Herries et al., 2020; Martini et al., 2021. 12

Table 4: Table that contains the geological information descriptions of the 11 caves. The descriptions are listed per member/ facies in the site. Each description is sourced from different journals to make a synthesized description and the journals used are listed in the "references" column. 20

Table 5: This table shows the seventeen samples used in this study and the type of lithology they are. The lithologies were defined using field observations and petrographic descriptions presented in chapter 3. MLPFE1, MLPFF1 and MLPFF2 were identified by Dirks et al. (2010) Pickering et al. (2011a) 38

Table 6: Table presenting results in Wt% of major oxides detected by the XRF for all petrographic samples. 76

Table 7: Table containing the major oxides reported in Wt% of the shale average three global standards i.e., UCC, NASC and PAAS. The major oxides reported coincide with the major oxides measured on the study samples. The table is modified from Ray and Paul (2021) Data

source: Taylor and McLennan (1985); Pourmand et al. (2012); Rudnick and Gao (2014). AEPS and ALPS data is from Ronov and Migdisov (1971). ACSD (average composition of sedimentary rock) and CWS (Clarke and Washington shale) are just table convenience acronyms used to represent data from Clarke and Washington (1924) including shale, sandstone, and limestone average composition data. 78

Table 8: Table containing major oxides in Wt% of the carbonaceous shale from the Malmani Subgroup (CSMG), Pretoria Group shale (PSG) and the black shales of the Chuniespoort Group (BSCG) in the Cradle. The acronyms are table specific and used in Harker diagrams below in the legend. Data source: Schreiber (1990); Reimer (1992); Meyer and Robb (1996); Erikson et al. (1994)..... 80

Table 9 : Table containing cosmogenic burial dating result for the six samples. N10 represents cosmogenic concentrations of ^{10}Be and N26 represents concentrations of ^{26}Al. 99

Table 10: Table containing the cosmogenic nuclide data measured from the six samples. 99

CHAPTER 1: INTRODUCTION

1.1 Site description

Malapa is a palaeoanthropological site discovered in 2008 in the Grootvleispruit valley of the Cradle of Humankind (Cradle) UNESCO World Heritage Site and is best known for the discovery of two partial skeletons of a species called *Australopithecus sediba* (Berger et al., 2010; Dirks et al., 2010; Kibii et al.,2011; Kivell et al., 2011; Pickering et al., 2011a; Zipfel et al., 2011; Berger, 2012; DeSilva et al., 2013; Williams et al., 2013; Churchill et al., 2018; Holliday et al., 2018). Malapa has two pits exposed at the site, pit 1 which is the main pit where the partially complete skeletons were found and pit 2, which is a shallow pit (Fig. 1). After initial excavations in 2008, five distinct sedimentary facies were established in pit 1: A to E from the base to the top of the cave deposits (Dirks et al., 2010). With later excavations in 2010, facies were then revised by Pickering et al. (2011a), who added and described the sixth distinct sedimentary facies i.e., F in pit 2. Two flowstones were mapped between the six facies and dated using the Uranium-lead (U-Pb) multicollector inductively coupled plasma mass spectrometry (MC-ICPMS) technique. Flowstone 1 (pit 1) described by Dirks et al. (2010) yielded two ages measured in two separate labs using the isochron (2.024 ± 0.062 Ma) and concordia (2.026 ± 0.021 Ma) method. Flowstone 2 (pit 2) yielded an age of 2.06 ± 0.140 Ma using an isochron method denoting a maximum age for the fossils (Pickering et al., 2011a). See Fig. 2 for a stratigraphical column and related ages of Malapa.

Dirks et al. (2010) constrained the age of deposition of *Australopithecus sediba* to 1.95-1.78 Ma using palaeomagnetic analysis on Facies C-E sediments and the flowstone. Pickering et al. (2011a) further constrained the age to 1.977 Ma using U-Pb and Palaeomagnetic data combined. Dirks et al. (2010) also used cosmogenic nuclide isotope ^{10}Be to constrain the erosion level and determine

the cave's original depth. The results show that surface erosion rate was at 3-5 m/Ma and approximately 8 m of overburden removed resulting in the deroofing of the cave in the past 2 Ma since the *Australopithecus sediba* fossils were deposited (Dirks et al., 2010). A better erosion rate of 0.86 ± 0.54 m/Ma was determined using the surrounding resistant chert dykes with an incision rate of approximately 8 m/Ma (Dirks et al., 2016). Using these new erosion rates, Dirks et al. (2016) suggested that the Malapa cave was 7-16 m deep when *Australopithecus sediba* fossils were deposited.

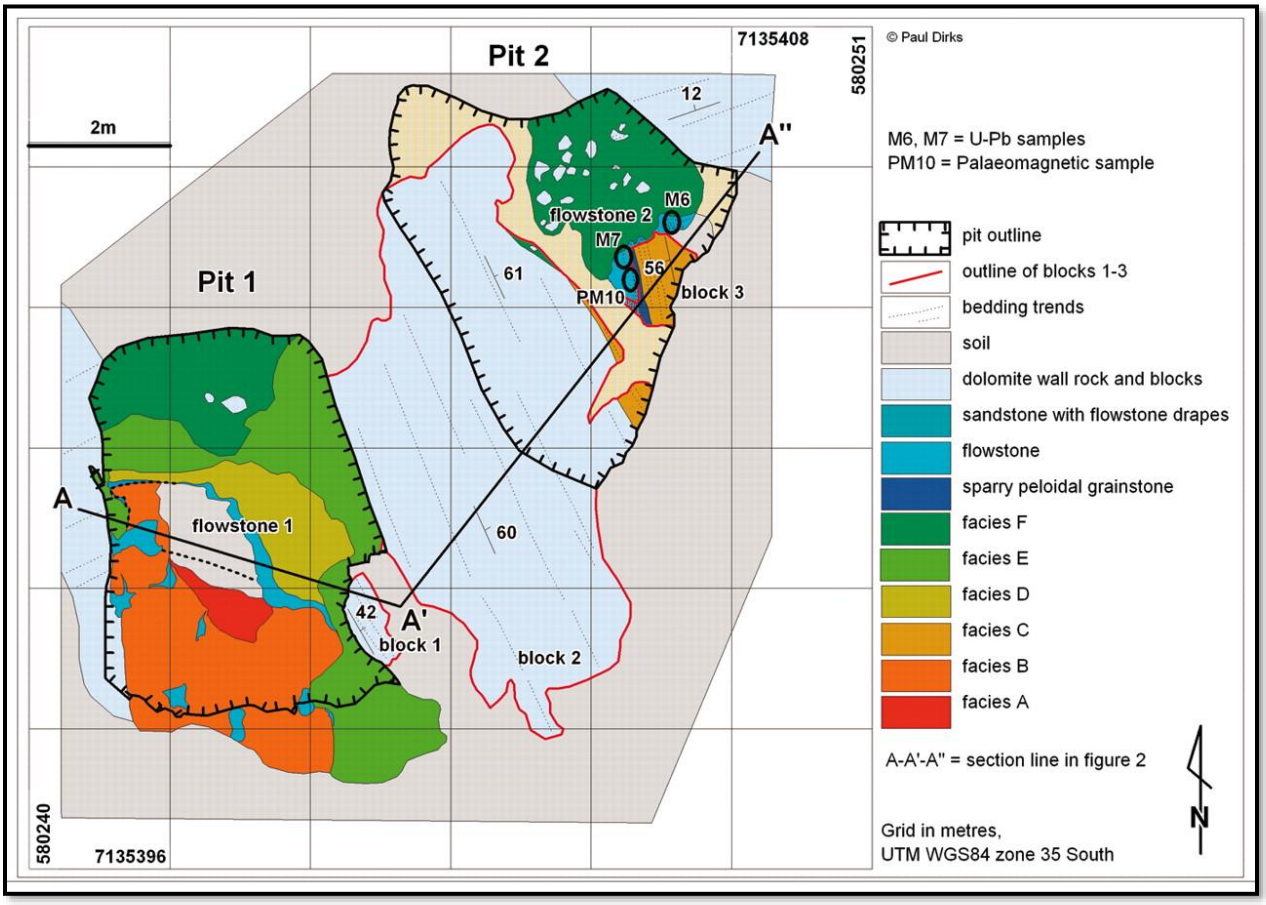


Figure 1: Geological map showing the six facies already established at Malapa and the two flowstones used for the geochronology. The map also shows the sample locations used for Uranium-lead dating and palaeomagnetic analysis (Pickering et al., 2011a).

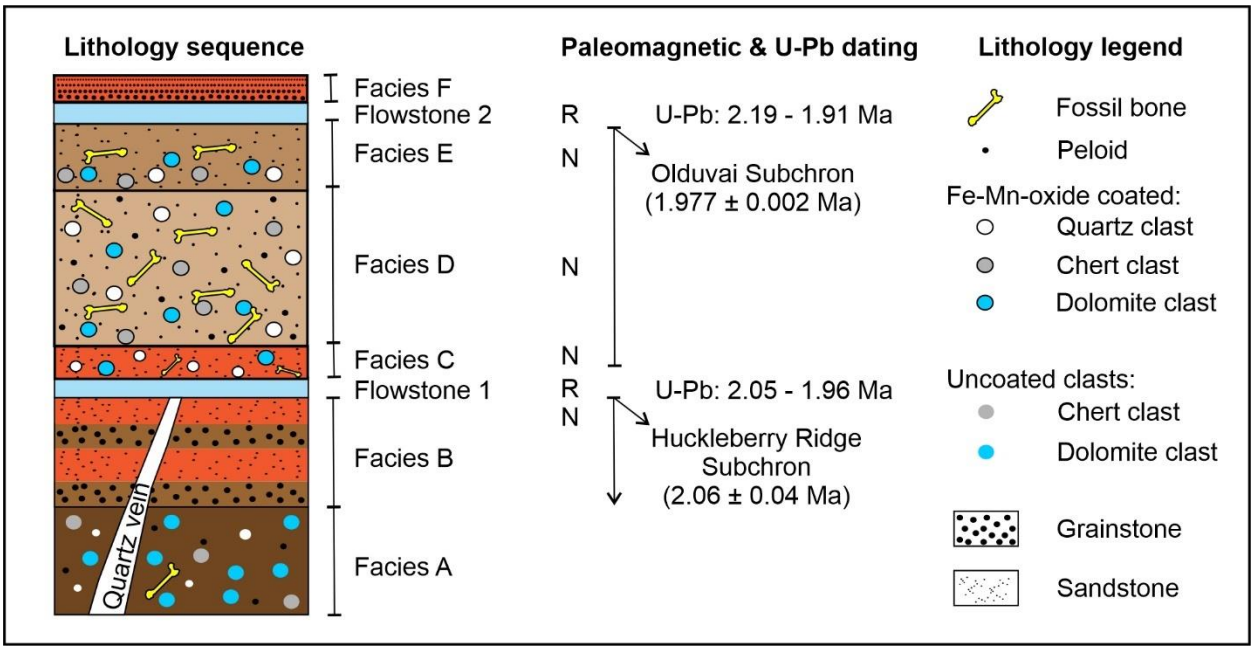


Figure 2: Stratigraphic column of Malapa showing Facies A-F and palaeomagnetic and U-Pb results. Flowstone one underlies facies A and B preserving a normal polarity near the base and reverse polarity in all other parts. This was intepreted as the Huckleberry Ridge Subchron (Dirks et al., 2010). Facies C, D and E recorded a normal polarity and was interpreted as the beginning of Olduvai Subchron (Dirks et al., 2010).The rock types observed are grainstone and sandstone. The figure is modified from Makhubela and Mavuso (2022). See Table 1 for a detailed facies descriptions.

Recent excavations at the Malapa site conducted in 2019 and early 2020 have exposed new fossiliferous and barren deposits (Fig. 3). These deposits also include pit 2 where Facies F has been described by Pickering et al. (2011a). The deposits were not exposed during earlier studies by Dirks et al. (2010) and Pickering et al. (2011a). The exposure of these deposits raised questions about their position in the stratigraphy and the chronology of the Malapa deposits. This study presents petrographic descriptions and ages of the cave sediments of these deposits. The age of

these deposits can be used to constrain the ages of possible hominin fossils and other undescribed fossils within the deposits.

1.2 Aims and research questions

This study aims to enhance the geological understanding of the Malapa site. Pickering et al. (2011a) described facies F in pit 2 and noted it represented the uppermost facies in the lithological sequence at Malapa. Facies F in pit 2 was targeted and sampled to assess if it is homogenous throughout pit 2 and if it is present in the newly exposed deposits. This study asked three research questions:

- Are the newly exposed strata composed of one of the facies already established at Malapa i.e., A-F, or multiple and different facies?
- What is the chronology of the newly exposed deposits?
- Are the newly exposed strata Early- Middle Pleistocene like the lower units found in Pit 1? Or are they Late Pleistocene?

1.3 Hypotheses

- The newly exposed deposits are composed of Facies F which was described by Pickering et al. (2011a), meaning the newly exposed deposits comprise of newly exposed Facies F deposits that are Early Pleistocene.

- The newly exposed deposits are a series of different facies belonging to facies A-F and Early Pleistocene in age.

- The newly exposed deposits are composed of new facies that have not been described and are probably younger in age (Middle-Late Pleistocene)

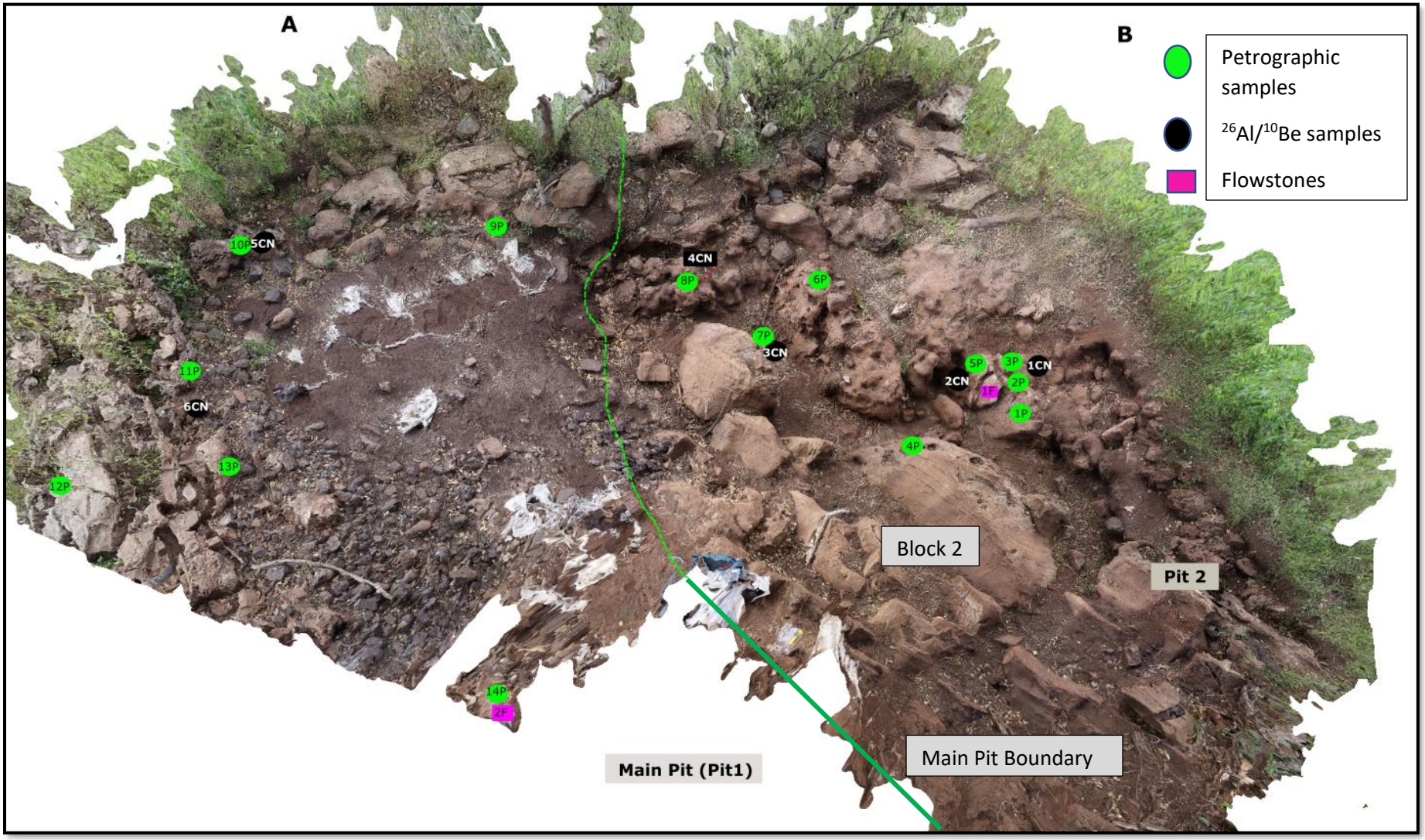

A
B
Petrographic samples
$^{26}Al/^{10}Be$ samples
Flowstones
9P
10P
5CN
4CN
8P
6P
7P
3CN
11P
6CN
5P
3P
1CN
2CN
1F
2P
1P
4P
13P
12P
Block 2
Pit 2
14P
2F
Main Pit (Pit1)
Main Pit Boundary

Figure 3: Photogrammetry photo of the newly exposed fossiliferous and barren deposits at Malapa. A) The newly exposed deposits and B) Pit 2 which was targeted to sample facies F. The photo shows where petrographic samples and cosmogenic nuclide samples were taken together with the two flowstones used for U-Pb dating in this study relative to the main pit. The main pit terminates by block 2 as ascribed by Pickering et al. (2011a). Photogrammetry photo credit: Paloma de la Peña.

Table 1: Table containing facies A- F description summary compiled using Dirks et al. (2010) and Pickering et al. (2011a). This summary details petrographic descriptions, field observations and interpretations (sedimentary environment). Facies A- F are interpreted as water-laid deposits with little post-depositional compaction indicated by loose packing of framework grains in sandstones (Dirks et al., 2010).

Facies	Description	Sedimentary environment
A	➢ Clastic sediment: dark-colored, coarse-grained, and moderately sorted. ➢ Abundant rounded grains of chert, quartz, and dolomite (0.5- 6mm) ➢ Framework grains: ooids, peloids, bone fragments, minor feldspar, mica schist, and Fe-oxide-coated grains ➢ Cement: blocky sparite	➢ Water-laid ➢ Deposition: Fluvial channel

B	➢ Alternating peloidal grainstone and clastic sandstone ➢ Grainstone: >50% rounded peloids (0.4-1mm), fewer bone fragments, fenestrae along bedding planes. ➢ Framework grains: Angular quartz (0.02-.10mm, abundant) and Fe-oxide-coated ➢ Cement: blocky sparite and micaceous mud matrix ➢ Sandstone: Abundant bone material, rounded Fe-oxide-coated grains, and insect burrows. ➢ Small stalagmite bosses growing on a grainstone substrate, and isolated dolomite blocks (<40 cm). ➢ Sandstone framework grains: ooids, shale, rounded chert/quartz	➢ Deposition: Muddy cave floor, along with local speleothem deposition
C	➢ Homogenous Facies B peloidal grainstone variation lacking clastic intercalations ➢ Layering defined by abundant fenestrae ➢ Framework grains: ~50% spherical mud pellets, ~15% voids and ~35% sparite ➢ Cement: coarse-grained isopachous sparite ➢ Grains toward the top of the layer: limestone, abundant Fe-coated grains, subrounded quartz, bone fragments, and shale	➢ Environment: Accumulated mud as pellets on the base of cave chambers ➢ Fenestrae present: organic-rich mud

D	➢ Sandstone: coarse-grained and poorly sorted ➢ Cement: blocky sparite and isopachous overgrowths in larger pore spaces ➢ Framework grains: dolomite, chert, peloids, quartz, and less common: shale, microcline, and ooids (0.5-2.5mm in size) ➢ Rounding: angular vein quartz crystals, well-rounded ooids, and peloids forming irregular patches	➢ Deposition: Water-logged mass flow
E	➢ Calcareous sandstone ➢ Finer grained, more sorting and rounding, and darker colored than Facies D ➢ Basal layer: well-sorted, coarse-grained sandstone and has a local sharp contact with Facies D ➢ Basal layer grains: 0.6-1.5mm large Fe-oxide-coated chert and quartz with peloid aggregates. ➢ Abundant fossil bone but less than Facies D	➢ Deposition: change from high-velocity mass flow (high flow regime to lower flow regime) to the alluvial flow of variable strength
F	➢ Defined by alternating peloidal grainstone and sandy peloidal grainstone. ➢ Fine-grained massive graistone ➢ Does not contain sandstone intercalations and speleothem build-ups ➢ Higher content of fossil material and large blocks of dolomite than Facies B	➢ Water-logged sediments

CHAPTER 2: STUDY BACKGROUND

2.1 Geological setting

The Cradle is a United Nations Educational, Scientific and Cultural Organization (UNESCO) World Heritage Site encompassing 47 000 hectares of land located 40 km northwest of Johannesburg in South Africa (Fig. 4). In addition to Malapa, the Cradle is home to several other palaeoanthropological sites such as Sterkfontein, Swartkrans, Kromdraai, Gladysvale, Rising Star caves, Bolts Farm, Minnaars, Coopers, Drimolen, Gondolin, and Haasgat (Brain and Sillent, 1988; Berger et al., 1993; Partridge et al., 2003; Pickering et al., 2007; Dirks and Berger, 2013; Gibbon et al., 2014; Berger et al., 2015; Braga et al., 2017; Edwards et al., 2019; Herries et al., 2020). These sites are known for containing fossil-bearing deposits that have preserved several species of hominin remains, archaeological remains, and other associated faunal assemblages (Curnoe et al., 2001; Partridge et al., 2003; Esterhuysen, 2007; Pickering et al., 2007; Herries et al., 2009; Sutton et al., 2009; Berger et al., 2010; Dirks et al., 2010; Pickering et al., 2010; Herries and Shaw, 2011; Pickering et al., 2011a, b; Berger et al., 2015; Dirks et al., 2015; Granger et al., 2015; Dirks et al., 2017; Hawks et al., 2017; Caruana and Stratford, 2019; Caruana et al., 2019; Pickering et al., 2019; Herries et al., 2020).

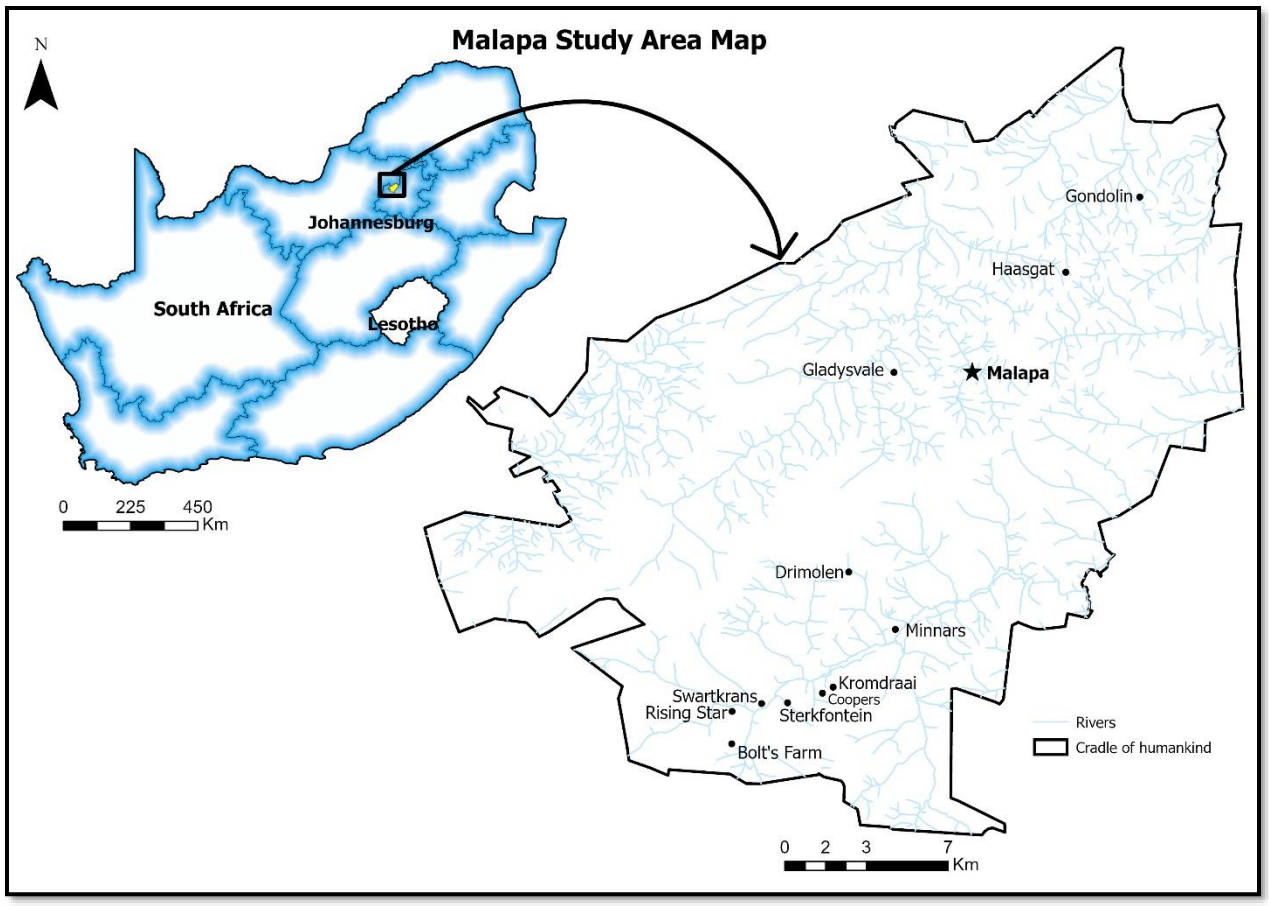


Figure 4: Geographical map showing the location of the Cradle and the 12 of some of the well-studied paleoanthropological sites within the Cradle. The study area i.e., Malapa is shown by the star symbol while the rest of the sites are shown by dots. Map created by Dakalo Maphanda.

The paleoanthropological sites in the Cradle are dolomitic karstic caves formed in the Malmani Subgroup dolomitic sequences of the lower Neoarchaean levels to Palaeoproterozoic (2.65–2.05 Ga) dolomites (Eriksson et al., 1995; Eriksson & Altermann, 1998; Eriksson et al., 2006). The Malmani Subgroup is 1200m thick and falls under the Chuniespoort Group in the Transvaal Supergroup (Button, 1973; Eriksson et al., 2006). The Malmani subgroup is subdivided into five formations based on chert content, absence or presence of stromatolite structures, and the variation degree of stromatolite structures (SACS, 1980; Eriksson & Truswell, 1974; Obbes, 1995; Eriksson

& Altermann, 1998). The lowermost formation, the Oaktree formation, is succeeded by the Monte Christo, Lyttelton, Eccles, and the uppermost Frisco formation (Obbes, 1995; Obbes, 2000; Eriksson et al., 2006). For further information about the Transvaal supergroup, see SACS, 1980; Andreoli, 1988; Eriksson & Reczko, 1995; Obbes, 2000; Alexandre et al., 2006; Ingram and van Tonder, 2011; Grab and Knight, 2015. Table 2 summarizes the five formations.

Table 2: Summary of Malmani Subgroup formations in terms of lithology and measured thickness (Wright et al. (2000).

Formation	Member	Lithology	Thickness (m)
Frisco		Chert-free dark-brown dolomite	30
	Leeuwenkloof	Giant chert breccia	
Eccles		Chert-rich light-grey dolomite	490
Lyttelton		Chert-free dark-brown dolomite	290
	Crocodile River	Chert-rich grey-brown dolomite	
	Rietspruit	Chert-rich & colour-banded dolomite	
Monte Christo	Mooiplaats	Chert-rich light-grey dolomite	740
	Rietfontein	Chert-free light-grey dolomite	
Oaktree		chert- free dark-brown dolomite	330

Sites such as Sterkfontein, Swartkrans, Kromdraai, Gladysvale, Malapa, Rising Star caves, Bolts Farm, Minnaars, Coopers, Drimolen, Gondolin, and Haasgat are found within the five formations (table 3). All the sites previously mentioned except Bolt's farm and Minnaars contain early hominin taxa unearthed at the Cradle i.e., *Australopithecus sediba*, *Australopithecus africanus*, *Paranthropus robustus*, and early *Homo* (Dart, 1925; Broom, 1938; Clarke et al., 1970; Berger et al., 2010). Table 3 summarises where each site occurs within the five formations of the Malmani Subgroup and reports on some of the well-known finds within each site.

Table 3: Summary table showing the geological formation that each site occurs in and cave-specific well-known findings. Data from: Clarke, 1977; Partridge, 1978; Brain, 1981; Berger et al., 1993; Clarke, 1994; Keyser et al., 2000; Kuman and Clarke, 2000; Susman et al., 2001; de Ruiter, 2003; Partridge et al., 2003; Pickering et al., 2007; Steininger et al., 2008; de Ruiter et al., 2009; Berger et al., 2010; Dirks et al., 2010; Pickering et al., 2011a; Adams, 2012; Gommery et al., 2012; Clarke, 2013; Herries and Adams, 2013; Herries et al., 2013; Herries et al., 2014; Adams et al., 2016; Leece et al., 2016; Braga et al., 2017; Dirks et al., 2017; Edwards et al., 2019,2020; Herries et al., 2020; Martini et al., 2021.

Cave name	Geologic formation	Well-known findings	Dating	References
Malapa	Lyttelton	*Australopithecus sediba*	2.024 ± 0.062 2.06 ± 0.140	Dirks et al. (2010) Pickering et al. (2011a)
Sterkfontein	Oaktree/Monte Christo contact	*Australopithecus africanus* (Mrs. Ples), *Homo habilis*, *Paranthropus robustus*	1.784±0.090 to 2.800 ± 0.140	Pickering and Kramers (2010) Granger et al. (2015, 2022)

Swartkrans	Oaktree/Monte Christo contact	Early *Homo*, *Paranthropus robustus* (largest specimen recovered)	1.706 ±0.069 to 2.249 ±0.077	Pickering et al. (2019) and references there in
Kromdraai	Oaktree/Monte Christo contact	*Paranthropus* and early *Homo*	1.95to 1.77 Ma	Thackery et al. (2002)
Gladysvale	Eccles	*Australopithecus africanus* and early *Homo*	2.4Ma	Herries et al. (2013)
Rising Star	Monte Christo (lower parts)	*Homo naledi*	200 ±70ka to 253 ± 61ka	Dirks et al. (2015,2017) Robbins et al. (2021)
Cooper's	Monte Christo	*Paranthropus robustus*	1.375 ± 0.113	Pickering et al. (2019)

Drimolen	Monte Christo	*Paranthropus robustus* (Most complete skull found yet), *Homo erectus* and early *Homo*	1.789±0.104 to 2.673 ±0.103 2.04 ± 0.24	Pickering et al. (2019) Herries et al. (2020)
Minnaar's	Oaktree/Monte Christo contact	Bovidae, Equidae and Canids	Biochronology	Gommery et al. (2012)
Bolt's farm	Oaktree/Monte Christo contact	Primates and Dinofelis	1.752±0.149 to 2.668 ±0.304	Edwards et al. (2019)
Gondolin	Eccles	*Paranthropus robustus*		Herries (2022)
Haasgat	Eccles	*Australopithecus africanus* and *Homo*	1.686±0.236	Pickering et al. (2019)

The major fossil-bearing sites alongside other sites in the Cradle occur along ESE and NNE fractures, and lithological boundaries (Dirks and Berger, 2013). The study area (Malapa) is situated at the north end of a series of North-South trending caves in the Grootvleispruit valley and is stratigraphically bound to the top 40m of the Lyttelton Formation (Dirks et al., 2010; Dirks et al., 2016). Malapa lies near the base of an originally ~50 m deep, strata-bound, and fracture-controlled cave system that was eroded by a valley incision (Dirks et al., 2010; Dirks and Berger, 2013; Dirks et al., 2016). Malapa represents an erosion remnant of an in-filled and de-roofed cave (Dirks et al., 2010).

2.2 Geological information review in the Cradle

In this section, general descriptions of the deposits of the eleven previously mentioned sites in the Cradle (Fig. 4) were compared with deposits at Malapa to see variations in cave sediments. Because the fossil-bearing sites in the Cradle have a high degree of clustering, are distributed along lithological boundaries and the landscape evolved over time (Dirks and Berger, 2013), the sediment fill is variable. For context, it is relevant to discuss what cave sediments are and how they are incorporated within cave systems; particularly clastic sediments and speleothems because those are the only type of cave sediments in the Cradle (Pickering et al., 2011b). Speleothem is a term used for secondary precipitated minerals in caves composed mainly of calcite, aragonite, and gypsum (White, 2012). With petrographic descriptions being one of the study scopes, this general information is relevant in understanding stratigraphy of the newly exposed deposit and making interpretations.

Cave sediments have no universally recognized classification scheme but can be categorized into chemical and clastic sediments (Springer, 2005; White, 2007). These sediments are the most useful hydrogeological and paleoclimatic record proxies (White, 2007). Cave sediments have different

provenances: there are some that are locally derived e.g., material from collapsed cavern roofs, some are chemical deposits in cave void spaces e.g., calcite and gypsum speleothems, and some are transported by underground streams such as sand and silt (Bosch & White, 2004). Cave deposits vary in grain size and composition; clasts range from sand, silt, and clay-sized particles to cobbles and gravel and even as large as meter-sized boulders (Wiersma et al., 2020).

Clastic sediments are eroded particles from pre-existing rock that have been mechanically moved and subsequently deposited (Springer, 2005; White, 2007). These can be divided into allochthonous sediments, materials brought into the cave from outside, and autochthonous sediments locally derived materials within the cave (White, 2007). Allochthonous sediment composition depends on rock type and other available material in the drainage basin in which the cave is embedded (White, 2007). These allogenic sediments, archaeological material and bones are generally deposited by a fluvial channel or by colluviation resulting in multiple facies that relate to change in flow energy (Murszewski et al., 2020). Detrital grains make up most clastic particles in cave sediments and are brought into caves by various transport mechanisms such as wind, streams, and mass wasting (Springer, 2005, 2012). Clastic sediment deposits in caves typically include multiple distinct beds in terms of age, depositional process, appearance, and origins (Herman et al., 2012; Springer, 2005). Information retained from sedimentary structures, facies analyses, stratigraphy, and sedimentary textures can be used to infer how individual clastic sediments were transported and deposited into the cave (Springer, 2005). Clastic sediments in caves weather slowly and therefore are important repositories of artifacts and organic remains (Springer, 2005; Ghinassi et al., 2009). Facies differing in lithologies often grade into each other and may even occur in separate locations in the site thus producing synchronous lithological units (Latham et al., 1999; Forbes and Bestland, 2007; Murszewski et al., 2020). Also, chronologically

different facies may form under identical depositional environments and be lithologically similar (Murszewski et al., 2020).

Traditional stratigraphic laws and precepts can be applied generally in caves but there are cases where sedimentary laws such as the law of original horizontality, the law of superposition, and crosscutting relationships are violated (Springer, 2005). The law of superposition states, vertically stacked sediments become younger with increasing height and the law of original horizontality states that layers of sediments are originally deposited horizontal under the action of gravity. Law of original horizontality in caves is mostly violated as deposits form mainly as breccias from debris flows especially near the entrances of caves (Fairchild and Baker, 2012; O'Connor et al., 2017). These deposits are not deposited as horizontal layers as the law states. Also, because of this nature of deposition, oldest layers are not always at the base and young ones at the top as the law of superposition states. The law of Superposition is the most common law violated in cave clastic sediments. This law may not hold in caves as clastic sediments accumulate as debris cones and may have flowstones partition the deposit. These violations are not frequent and standard interpretations should be used in most cases when dealing with clastic sediments in caves (Springer, 2005).

Stratigraphy of a cave can be properly defined in terms of sedimentary facies, which are defined as a distinctly unique body of sediment that can be identified based on appearance, composition, and texture or sediment sizes. According to Springer (2005), sedimentary facies are used widely for interpreting depositional chronologies. Palaeocave stratigraphy formation is influenced by many complex processes including post depositional processes i.e., geogenic (chemical, and biogenic) and mechanical) (Goldberg, 2000; Murszewski et al., 2020). Chemical processes include cementation and dissolution, while mechanical processes include erosion, reworking and

remobilisation of sediments and lastly biogenic processes include biological activity such as burrowing (Murszewski et al., 2020).

Speleothems and clastic sediments are the only type of cave deposits in the Cradle as previously mentioned. Speleothem development results from the downward mobilization of carbonic acid from the surface through the dolomitic country rock (Herman et al., 2012; Murszewski et al., 2019). This results in calcium carbonate minerals precipitating due to CO_2 degassing once the solution reaches caverns (Harmon et al., 2004; Fairchild et al., 2006; Murszewski et al., 2019). Fairchild et al. (2006) noted that speleothem growth is expected to be related to CO2 availability in underground water and environmental moisture. Speleothems fabrics are a result of the addition of carbonate layers as it grows and exhibits a wide range of internal fabrics (Hirschey, 2015). These fabrics are described by Frisia et al. (2000), Frisia and Borsato (2010) and Frisia (2015), see table 1 from Pickering and Edwards (2021) for speleothem fabric summary. Speleothems are classified (unofficially) based on flow characteristics that deposited them (White, 2019). Stalagmites and stalactites are forms created by dripping water and flowstones forms are created by flowing water (White, 2019).

In the Cradle, speleothems occur as layers of flowstones, stalactites or stalagmites usually flowing down sediments and dolomitic walls vertically and sometimes horizontally (Pickering et al., 2011b). They are often interbedded with chaotic bedded clastic sediment in the form of breccias (Pickering et al., 2011b). The bulk of the flowstones (and other speleothems) often form as basal flowstones that covers the dolomite bedrock, roof, and wall collapse (Pickering et al., 2019). Clastic sediments occur as breccias that formed as autochthonous and allochthonous sand to clay-sized debris mixed with gravel to boulder- sized breakdown material from cave walls and ceilings (Dirks and Berger., 2013). Although clastic sediments in most sites in the Cradle occur as breccias,

there are sites where well-stratified cave fill is observed such as Gladysvale and Rising Star cave, and to some degree, almost all other sites. Clastic sediments accumulated on talus cones as sheet wash and debris flow and got cemented by carbonate-rich waters dripping from the cave celling (Dirks and Berger., 2013). The deposits in the Cradle, especially the hominin-bearing deposits; developed in similar environment settings that include debris cone accumulation beneath a vertical cave void (Pickering et al., 2007; Pickering and Kramers, 2010; Dirks and Berger, 2013). Most of the cave sites mentioned previously comprise a basal layer of a speleothem and several clastic sediment units that are separated by erosional hiatuses or flowstone layers (Pickering et al., 2011b). These unconformities reflect an episodic cave fill typical of the Cradle deposits (Dirks and Berger., 2013; Herries et al., 2020). Different sites have classified the clastic sediments using a member system (e.g., Sterkfontein, Swartkrans, Kromdraai: Partridge, 1978; Brain, 1993; de Ruiter et al., 2009; Pickering et al., 2011b; Bruxelles et al., 2016), or facies (e.g., Malapa, Gladysvale, Rising Star Cave: Dirks et al., 2010; Pickering et al., 2011a; Dirks et al., 2015; Wiersma et al., 2020).

Below is a table summary with petrographic descriptions of Sterkfontein, Swartkrans, Kromdraai, Gladysvale, Malapa, Rising Star caves, Bolts Farm, Minnaars, Coopers, Drimolen, Gondolin, and Haasgat. Swartkrans, Sterkfontein, Cooper's cave, Gladysvale, Rising Star cave, Kromdraai, Drimolen and Malapa preserves mostly in-situ deposits whereas Bolt's farm, Minnaars, Gondolin and Haasgat preserves ex-situ deposits exposed by lime mining and some important in-situ deposits as well. These petrographic descriptions help in providing an understanding of the broader and site-specific depositional environments and allow for correlation between different facies of different sites. This is particularly important to this study in assessing the uniqueness of the newly exposed deposits as opposed to those already established at Malapa and those observed in other sites of similar setting and age.

Table 4: Table that contains the geological information descriptions of the 11 caves. The descriptions are listed per member/ facies in the site. Each description is sourced from different journals to make a synthesized description and the journals used are listed in the "references" column.

Cave name	General descriptions	Petrographic descriptions	References
Sterkfontein	➢ Stratigraphy: formed by a simple solution excavation of dolomite host rock along fracture systems (Pickering et al. (2011b) ➢ Fossil-bearing sediments exposed underground and at the surface. ➢ Six members (M1-M6) of calcified breccias of dolomite, chert, and surface soil, post-member 6 and Lincoln cave deposits. Pickering and Kramers (2010) suggested a change to facies A-E ➢ Generally, members are composed of manganese-rich dark brown residual clastic fill which contains clay pellets, large chert, and dolomite blocks.	➢ M1: Dark brown non-fossiliferous, manganese-rich clastic sediment residual fill. It contains gravel-sized angular chert/dolomite clasts and calcite interbeds. Depositional environment: debris accumulation over non-permanent cave opening. ➢ M2: Reddish-brown talus deposit, horizontally bedded with abundant speleothems fragments and bones. ➢ M3: Reddish-brown muddy sandstone with basal flowstone and angular gravel sized fragments and bones. ➢ M4: Calcified massive breccia, reddish brown and clast-rich loamy deposit with inclusions of pebble-boulder sized rock debris. ➢ M5: Reddish-brown breccia with more sandy loam, stone tools, and some bones. ➢ M6: Darker, less-calcified reddish-brown clastic deposit with a basal flowstone.	Partridge and Watt (1991) Martini et al. (2003) Pickering and Kramers (2010) Pickering et al. (2011b) Stratford et al. (2014) Makhubela and Mavuso (2022)
Swartkrans	➢ Stratigraphy: formed by several cycles of deposition and erosion ➢ Five members with six discrete fossiliferous deposits	➢ Member 1: LB represents a steep dipping talus cone that is infilled with poorly calcified fossiliferous, Orange-colored stony breccia. HR is a fossil-rich pink breccia that infills the outer cave. ➢ Member 2: Comprises of outer brown breccia and inner stratified brown breccia. These deposits are heavily calcified, fossil rich	Brain (1976) Butzer (1976) Brain (1993) Brain et al. (2004)

	➢ Member 1 represents the oldest known strata. It has two depositional subunits i.e., the Hanging Remnant (HR) and the Lower Bank (LB)	including hominids and archaeological artefacts. The outer cave deposits are reddish brown that are poorly sorted clay-sand-silt sediments. The inner cave deposits are reddish brown and moderately sorted composed of clay-sand-silt sediments and moderately recrystallized calcite. ➢ Member 3: A partially preserved deposit, moderately fossiliferous including few hominids fossils, lithic artefacts and cut, utilized, and burnt bone. ➢ Member 4: This member is rich in Middle Stone Age lithic artefacts and may lack fossil bone. ➢ Member 5: This is an infilled channel deposit	Sutton et al. (2009) Pickering et al. (2011b, 2012)
Kromdraai	➢ Un-roofed cave split into Kromdraai A (KA) with no hominins and Kromdraai B (KB) with archaeological and faunal samples primarily derived from three distinct depositional phases and Kromdraai C (KC). ➢ Stratigraphy: Successive stages of filling and progressive dismantling of a single initial cave. ➢ Includes several successive cycles of erosions, mineralization, depositions, and demineralization. ➢ KB comprise of 5 members (Partridge (1982)) and Bruxelles et al. (2016) proposed 7 members; all upper contacts are considered eroded or disconformable and interpreted as a depositional hiatus. ➢ Braga et al. (2022) proposed new stratigraphy of unit A, O and P.	➢ Member 1: Dark grey stony breccia composed of altered and unaltered chert blocks and dolomite fragments covered in inure iron-manganese rich matrix. Chanel cut deposit. ➢ Member 2: Regular bedded orange breccia with blunted to angular chert and dolomite fragments. Has several fine-grained zones and matrix. Chanel cut deposit. ➢ Member 3: Sedimentary structureless pink sandstone with calcite pieces. Angular chert fragments and dolomite blocks are rare to find. Mudflow deposit ➢ Member 4: Has three sub members i.e., pink bedded breccia and sandstone, massive pink sandstone that becomes stonier towards the distal end and breccia with more abundant sandy breccia. Composed of dolomite, siliceous breccia fragments, conglomerate chert with gravel and rarely calcite. ➢ Member 5: Orange sandstone with small pieces of weathered breccia and ferruginous fragments inclusions. Composed of small, rounded chert and cubic ferruginous clasts with no dolomite blocks ➢ Member 6: Orange to brown breccia with weathered chert and ferruginous fragments only	Partridge (1978) Partridge (1982) Braga et al. (2016, 2022) Bruxelles et al. (2016)

		➢ Member 7: Bedded Orange sandstone with gravel layers. Finely laminated sandstone with calcite veins and chert plus ferruginous cubes as detrital grains	
Drimolen	➢ Deposits at Drimolen Makondo, Drimolen Main Quarry and Porcupine Cave ➢ Contains both calcified and decalcified deposits with three macro-scale depositional facies identified (facies 1-3). ➢ The three facies have six sub-facies (a-f) mapped and described between facies 1 and facies.	➢ F1: Talus cone breccia (TCB), composed of a calcified, un-sorted sub-angular dolomite, chert, quartz, and few micaceous clasts that are heavily stained by iron and manganese oxides. It is mostly clast-supported with some area being matrix-supported. The matrix is reddish-brown sandy-silty loam matrix. It has 4 sub-facies (a-d) ➢ F2: Reworked talus cone breccia (SBC), composed of very poorly sorted deposits of TCB in terms of composition. The deposits are cemented by subhedral calcite, and the grains and clasts are coated with iron-manganese (Fe-Mn) rich coating around their boundaries. Presence of rounded-sub-rounded iron nodules. It has sub-facies e-f. ➢ F3: Fluvial sandstone-siltstone deposits (SSS), composed of moderately to well-sorted angular-sub-rounded quartz with fewer chert and dolomite. The matrix is the same as TCB and SBC. It contains fossil bone.	Keyser et al. (2000) Herries et al., 2020 Murszewski et al. (2020)

Cooper's cave	➢ Stratigraphy: comprise of three spatially distinct infills of fossil-bearing sediments i.e., Copper's A, B and D ➢ The deposits are referred to as CA, CB, and CD and they are situated partway between Kromdraai and Sterkfontein. CD is the most studied one and hence will be presented here. ➢ CD has calcified deposits in form clastic breccias which later decalcified and formed loose sediments and soils. CD has two area with cave fill named CD west and East deposits. ➢ Stratigraphy is defined in terms of three section (section 1-3) which are in turn used to make facies A-C.	➢ CD East: Composed of facies A, B and C. ➢ Facies A comprises of massive sediments of dolomite clasts, fossil bone and a reddish-brown sandy matrix. ➢ Facies B consists of bone-rich sandy matrix which is reddish-brown in color, dolomite roof blocks and more teeth, fossil bones and smaller dolomite clasts. ➢ Facies C consists of sandy sediment, brownish red in color and has distinct layering. Facies C has abundant microfaunal fossils. ➢ CD West: It has similar deposits to CD East. Facies A is much coarser than in the East. Facies B has less fossil content than in the East. Facies C is composed of layered fine-grained material that washed further inside the cave. Macrofossils are found in facies A and B.	Berger et al. (2003) Steininger et al. (2008) de Ruiter et al. (2009) Pickering et al. (2011b)
Gladysvale	➢ Deposits: Well-stratified cave fill with abundant intercalated flowstones ➢ Stratification is based on the presence of intercalated flowstones that forms 17 flowstone-bounded units (FBU) ➢ Divided into units, three exposed strata and four types of clastic sediments identified i.e., facies A-D and facie E comprise of all speleothems	➢ Facies A: is a massive, clast supported and extensively weathered deposit with large subrounded dolomite blocks containing chert bands with no minimal matrix. The matrix between boulders of facies A-D is a decalcified medium-grained sand that is reddish-brown in color. ➢ Facies B: composed of pale reddish-brown to moderate brown sediments. The deposit a massive and clast-poor with no internal layering. It contains dolomite clasts, subrounded-subangular chert, oncoids and subangular speleothem clasts. The matrix is a quartz-rich sand that is fine-medium grained. This unit is mostly decalcified. ➢ Facies C: contains well-calcified pale reddish brown to moderate brown sediments that are matrix supported in a fine-medium	Pickering et al. (2007)

		grained sand. The sediments are well preserved, poorly to well-layered with horizontal and lenticular laminations, and has abundant fossil bone. ➢ Facies D: generally, clast-poor, grayish brown to brownish-gray fine-grained muddy sediments. Characterized by fine horizontal laminations making a microstratigraphy that preserved few bones very well. It consists of abundant subrounded to subangular chert and dolomite clasts and very small clasts of calcite	
Rising Star cave	➢ Comprises of Dinaledi (main fossil-bearing), Postbox, Superman and Dragon's Back chambers to name a few. ➢ Deposits are mostly unlithified mud clast breccias (UMCB), lithified mud clast breccias (LMCB), laminated orange sands (LOS), massive orange sands (MOS), polymictic breccia (CPB) and laminated orange-red mud (LORM). ➢ There are three stratigraphic units and two facies described by Dirks et al. (2015) at Dinaledi Chamber. Unit 1 represents a laminated maroon mudstone. Unit 2 represents older mud clast breccias and unit 3 are cave floor sediments of youngest mud clast breccias. Unit 1 and unit 3 were subdivided into Unit 1a- 1c and Unit 3a- 3b respectively. ➢ In summary, both breccias and well-stratified sediments are found at Rising Star Cave	➢ Facies 1: Horizontally laminated, unlithified orange mud with low sand content. It is composed of fine sericite clay, secondary Mn-Fe- oxide concretions with minor silt-sized dolomite and chert grains. Facies 1 has two sub-facies described i.e., facies 1a and 1b. Facies1a are autochthonous suspension deposits that horizontally laminated that are associated with a low-energy depositional environment. Facies 1b is defined by an orange-brown mudstone that is interlaminated with thin lenses of fine to medium-grained sand. The sand contains abundant micromammal fossils, angular-subrounded grains of quartz and chert. ➢ Facies 2: Unconsolidated to consolidated Orange-brown mud clast breccia in a mud matrix. The mud clast breccia is not layered, massive, surrounded by brown mud matrix. It has localized patches of sparry carbonate cement. The deposit is composed of angular dolomite and chert clast that are pebble to cobble-sized and weakly consolidated angular orange-brown mud fragments. ➢ UMCB, LMCB, LORM, LOS, MOS and CPB are sediment types described in Wiersma et al. (2020) and Robbins et al. (2021). These are a different nomenclature to the facies and units of Dirks et al. (2015, 2017). These lithofacies are a type locality and has not been described anywhere else in the Cradle. The new nomenclature still corresponds to the nomenclature of Dirks et al. (2015, 2017) for example UMCB facies are sub-unit 3b deposits. Please see consulted literature for more information.	Dirks et al. (2015) Dirks et al. (2017) Wiersma et al. (2020) Robbins et el. (2021)

Gondolin	➢ Gondolin has deposits in four localities (Gondolin 1-4, i.e., GD1-GD4) ➢ Fossils are preserved in red siltstone matrix. GD1 and GD2 (in-situ deposits) are the two main localities and are stratigraphically discontinuous. ➢ The cave system consists of complex mix of grey breccia, conglomerates, and fine-grained clastic sediments which are partially decalcified. ➢ Herries et al. (2006) noted the deposits to be rather heavily calcified and composed of siltstones, conglomerates, breccia, and abundant speleothems.	➢ Stratigraphy at Gondolin starts with a basal breccia sourced from collapse of the dolomite ceiling. The breccia contains large blocks of dolomite with void spaces that are filled with smaller blocks and is mainly cemented by calcite flowstone. ➢ The Conglomerate Unit: this fining upwards unit with evidence of sorting deposit consists of average clast sized that are angular and has a distinct rounding at the edges. They are interpreted to be deposited as bedload deposits of a stream. ➢ The Finer Clastic Unit: This consists of fossiliferous finer sediments such as siltstones, grits and sandstones that are capped by a flowstone. The clastic sediments in this unit are interpreted as having accumulated on a debris cone corner. ➢ GD1: Consists of a complex mix of conglomerates, grey breccias and other decalcified fine-grained clastic sediments. This are analogous to the Conglomerate Unit. ➢ GD2: Consists of calcified red siltstone with matrix that preserves dense bone accumulation in a breccia with a basal spleothem breccia and laminated flowstones that also caps the deposit.	Menter et al. (1999) Herries et al. (2006) Adams et al. (2007) Herries and Adams (2013)
Haasgat	➢ Haasgat contains ex-situ and in-situ deposits with at least two episodes of cave-fillings. ➢ Sediments such as sand, silt and bones were brought into the lower parts cave by flash floods where they were subsequently cemented by lime-rich solutions to form fossiliferous red siltstone.	➢ Consists of a long tunnel that is filled to the roof with breccia, conglomerate and fine-grained laminated sediments and speleothem. Older phase: red to reddish brown siltstones and mudstones. Limited phase: uncalcified dark brown sediment	Keyser and Martini (1991) Plug and Keyser (1994) Adams (2012) Herries et al. (2014)
Minnaars	➢ The cave inception is discussed in Gommery et al. (2012)	➢ Not much is known about the geological context of Minnar cave as it consists of multiple localities which were hard to find. ➢ There deposits are a combination of in-situ and ex-situ breccia blocks containing primates and other fauna such as bovids and carnivores.	Gommery et al. (2012)

Bolt's Farm	➢ Represents what is accepted to be deposits of various ages formed at the different times but part of the same cave system. It may also represent the infill of several unconnected caves. The deposits are in 23 fossiliferous pits, a mention of all deposits will not be covered in this summary but rather a representative description will be presented. ➢ Edwards et al. (2020) gave facies descriptions for pit 5, 14, 8 also known as the Aves Cave Complex.	➢ Pit 5: consists of sandstones, siltstones and flowstones. ➢ Pit 8: consists of lithified sediments of siltstone, sandstone, large chert blocks and flowstones. ➢ Please see table 1 of Edwards et al. (2020) for the facies description and interpretation for Bolt's farm. Currently the table presents 8 facies (A, B, B1, C, D, E, F, and G). ➢ The facies descriptions differ type of clast, bone content and the matrix. In general Bolt's farm is dominated by laminated brown siltstone that can be sandy or clay rich. The siltstone differs also in bone content which distinguishes each facies from the other.	Edwards et al. (2019) Edwards et al. (2020) Edwards et al. (2023).

In summary, all deposits in the Cradle contain dolomite blocks, fluvial clasts such as quartz and chert, fossils, and flowstones of varying sizes. The deposits either occur as chaotic breccias or as well-stratified deposits and often both occur in one site in various colors and textures e.g., Rising star cave. Beside Gladysvale and Sterkfontein (pellets), no other site mentioned the presence of oncoids, or similar grains such as peloids or ooids which make up most of the grains at Malapa in most facies. Most of the sites in Cradle described in table 4 including Malapa, contain inclusions of Fe-Mn oxides either as nodules or coating around the grains. A study by Makhubela (2014, 2017a) describes these Fe-Mn-oxides based on samples collected from the main pit at Malapa. In the study, they were referred to Mn-Fe-oxyhydroxides. The study showed that Malapa samples contain at least four types of Mn-Fe-oxyhydroxide-rich coating around their grains (Fig. 5). The study noted grains mostly coated are chert and quartz grains. It was also noted in this study that chert and quartz are the most common nuclei in all coated grains. The Mn-Fe-oxyhydroxide coating types were used as a guideline in all the SEM-EDS

samples for this study. This study grouped the coatings into 4 types i.e., type 1 (A-C), type 2 (D- F), type 3 (G- I) and type 4 (J- L) (Fig. 5). Type 1 coating represents samples that are thinly coated, and the coating is not always present around the grain boundaries; type 2 represents the most common coating type- it has a thick concentric coating and (non-) fragmented chert/ quarts grains as a nucleus; type 3 represents fragmented chert and quartz grains infilled with Mn-Fe-oxyhydroxides coating; type 4 represents grains that are entirely composed of the coating.

Majority of the sites have erosion processes removing deposits leaving stratigraphy with gaps or resulting in discontinuous deposits that are hard to date and correlate. Most depositional process observed in the Cradle involves a talus cone collapse with sediment of sand to silt-sized rich in bones (often) washing into the vertical cones. The sediments seem to get to the deep chambers of the cave by a debris flow that sometimes mixes the old deposits with the new deposits. Subsequent erosion of some layers removes depositional context in many ex-situ deposits.

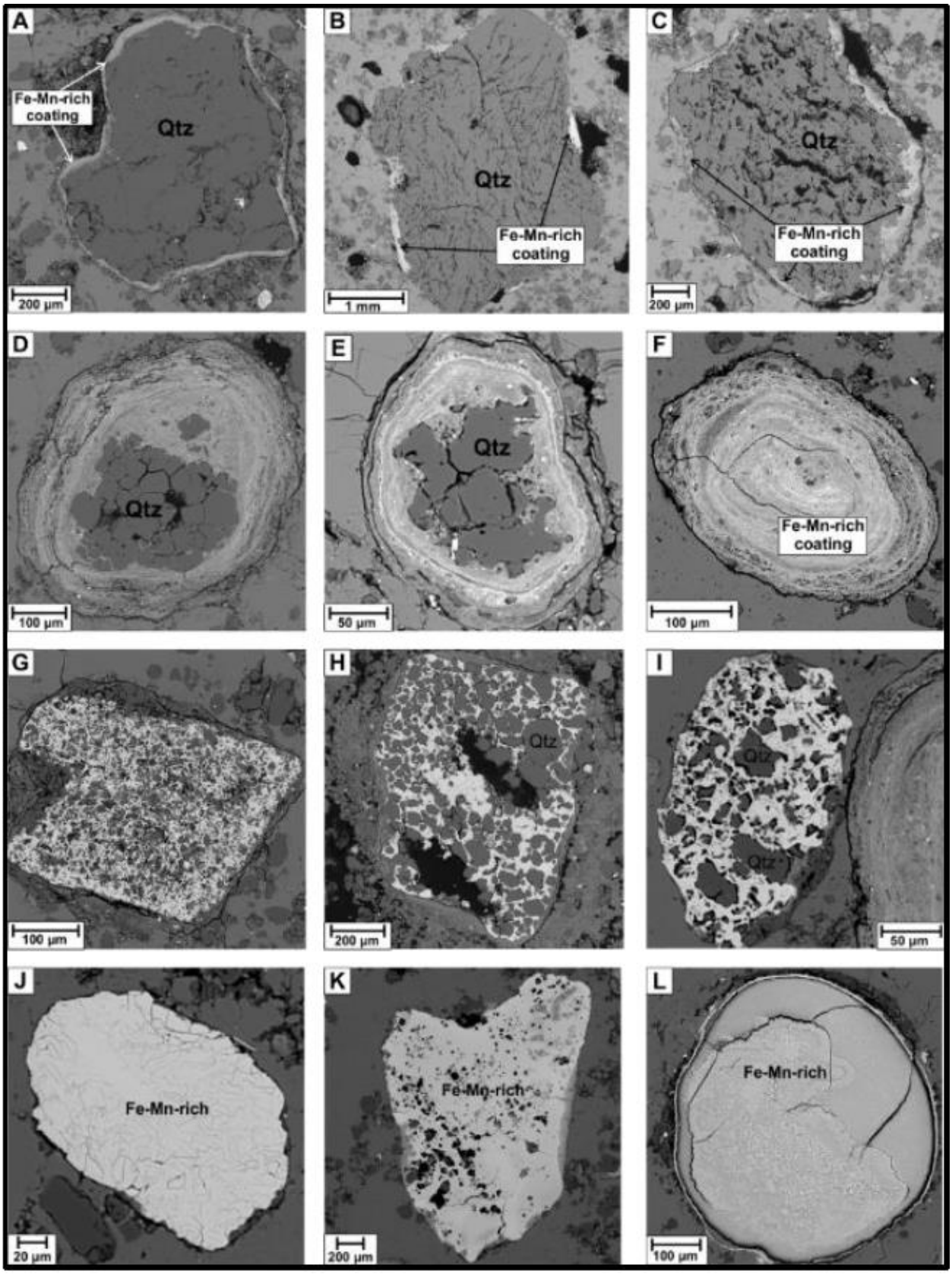

A
Fe-Mn-rich coating
Qtz
200 µm
B
Qtz
Fe-Mn-rich coating
1 mm
C
Qtz
Fe-Mn-rich coating
200 µm
D
Qtz
100 µm
E
Qtz
50 µm
F
Fe-Mn-rich coating
100 µm
G
100 µm
H
Qtz
200 µm
I
Qtz
Qtz
50 µm
J
Fe-Mn-rich
20 µm
K
Fe-Mn-rich
200 µm
L
Fe-Mn-rich
100 µm

Figure 5: SEM image showing four types of Mn-Fe-oxyhydroxides coating as described by Makhubela (2014). A - C shows type 1, D - F shows type 2, G – I shows type 3, and J – L shows type 4. “Qtz” stands for quartz.

2.3 Dating of deposits in the Cradle

Dating cave deposits is not straightforward (Stock et al., 2005), particularly in the Cradle (Partridge et al., 2003; Pickering et al., 2010, 2011a, 2011b; Granger et al., 2015; Dirks et al., 2017) because there are no volcanic tuffs that are easy to date like other hominin-bearing deposits of East Africa for example. The other challenge in dating deposits of the Cradle is the nature of the deposits themselves. The deposits formed by complex karstic processes which occasionally involves a collapse of older sediments into younger chambers within sites resulting in even more complex depositional histories and stratigraphy (Pickering and Kramers, 2010; Stratford et al., 2014). So, the formation processes and sedimentological dynamics in the Cradle have resulted in discontinuous deposits in many sites. It has been historically thought that stratigraphy and chronology cannot be defined for these types of deposits but recent work like those of Pickering et al., 2007, Edwards et al., 2020, 2023 and this very own thesis are challenging that status quo. That said, this does not undermine that even where the stratigraphy is well defined, there is still a challenge of finding datable material. The deposits are further complicated by the mining activities (lime mining) that occurred in the Cradle in the 19th to early 20th century (Thackeray, 2020). This either removed or obscured stratigraphic context leading to reconstructed or assumed stratigraphical context (Murszewski et al., 2020). Hence, the dating of fossil-bearing cave deposits in the Cradle has mostly been done using the biochronology method and paleomagnetism (see Herries, 2003; Herries et al., 2006, 2009, 2010; Adams et al., 2007, 2010). Some of the chronology methods used in the Cradle include U-Pb, Uranium-thorium disequilibrium dating (U/Th),

Uranium-thorium-helium dating ((U, Th)-He), Cosmogenic nuclide burial dating ($^{26}Al/^{10}Be$) burial dating, paleomagnetism, Electron Spin Resonance (ESR) and the argon-argon dating ($^{40}Ar/^{39}Ar$). $^{40}Ar/^{39}Ar$ has not been applied successfully in the Cradle. The principle of dating cave deposits using radiometric methods such as U-Pb, U/Th, (U, Th)-He, and $^{26}Al/^{10}Be$ is to give absolute ages that are well constrained and create temporal correlation data in human evolution related deposits.

The U-series (U-Pb and U/Th) are the most well-suited methods in dating speleothems that provide a precise sample specific chronology (Pickering and Edwards, 2021). The use of U-Pb geochronology in speleothems is a well-established radiometric dating method in the Cradle (Walker et al., 2006; de Ruiter et al., 2009; Dirks et al., 2010; Pickering and Kramers, 2010; Pickering et al., 2011b; Hopley et al., 2019; Pickering et al., 2019; Edwards et al., 2020; Pickering and Edwards, 2021; Edwards et al., 2023). Calcite U-Pb geochronology via MC-ICP-MS method was used at Malapa to constrain the age of *Australopithecus sediba* both in the main pit and pit 2 (Dirks et al., 2010; Pickering et al., 2011a). The U-Pb dating method in the Cradle has short coming and this is primarily due to the requirements of the method. U-Pb dating uses the radioactive decay of uranium and thorium isotopes (^{238}U, ^{235}U, and ^{232}Th) into stable isotopes of lead (^{206}Pb, ^{207}Pb, and ^{208}Pb, respectively) (Parrish, 2014; Parrish, 2015). This method can be applied to any mineral that can retain uranium or thorium in its structure (Parrish, 2014). Common minerals that U-Pb geochronology has been used include zircon, monazite, titanite, baddeleyite, perovskite, apatite, allanite, rutile, xenotime, uraninite, calcite/aragonite, thorite, and pyrochlore (Parish, 2014). One of the most important aspects of checking a mineral's suitability for U-Pb dating is ensuring that it has little to no initial common lead (Parrish, 2015). This ensures that the lead within the mineral is primarily radiogenic when dated. In minerals such as calcite, apatite, and titanite where the ratio

of U/Pb is relatively low, an isochron approach using LA-ICP-MS can be used with a common lead composition correction (Parrish, 2015; Woodhead et al., 2012). Uranium concentrations in calcite can be ca. 10ppb to 10ppm U in comparison to >100ppm U in other uranium-bearing minerals such as zircons (Roberts et al., 2020). In the Cradle specifically, the speleothems have been found to contain much less U (<1 ppm) with aragonite containing more U than calcite (Pickering and Kramers, 2010; Pickering et al., 2011a, 2011b; Robbins et al., 2021; Makhubela and Kramers, 2022; Pickering and Edwards, 2021; Edwards and Pickering, 2022). The Cradle speleothem have also been studied by Pickering and Edwards (2021) in terms of how calcite fabrics affect the ages resulting from using the U-Pb method. The study does conclude that some speleothems do show evidence of diagenesis and they are prune to show "bad ages". To get good accurate ages on speleothems suspected to have undergone diagenesis, especially those as old as the ones found in the cradle, one is advised to do through petrographic studies to identify fabrics. The guidelines and how to interpret such fabrics to relate to diagenesis and how it affects the dates provided can be found in the Frisia (2015) paper. Pickering and Edwards (2021) did prove with an aid of thin section petrography results sampled from the Cradle and Wonderwerk cave (outside the Cradle but sits in the same dolomitic bedrock) that all flowstones in the Cradle have undergone heavy diagenesis. They also argued that although the degree of diagenesis controls the quality of the age given, some speleothems can provide absolute ages with little errors.

Calcite U-Pb geochronology using LA-ICP-MS is preferred on hydrothermal diagenetic calcite because lead and uranium are distributed heterogeneously on the sub-millimeter scale (Roberts et al., 2020). Successful studies using LA-ICP-MS in calcite geochronology have been increasing widely in science, for example; Li et al., 2014; Coogen et al., 2016; Methner et al., 2016; Ring and Gerdes, 2016; Roberts and Walker, 2016; Burisch et al., 2017, 2018; Drake et al., 2017, 2019,

2020; Goodfellow et al., 2017; Nuriel et al., 2017, 2019; Beaudoin et al., 2018; Godeau et al., 2018; Hansman et al., 2018; Hellwig et al., 2018; Drost et al., 2018; Mangenot et al., 2018; Parrish et al., 2018; Walter et al., 2018; Yokoyama et al., 2018; Bertok et al., 2019; Holdsworth et al., 2019; MacDonald et al., 2019; Scardia et al., 2019; Nicholson et al., 2020. For more information on U-Pb dating on speleothems and data generated using LA-ICP-MS, see Paul et al. (2005), Woodhead et al. (2006, 2012) and Woodhead and Petrus (2019). In the Cradle, LA-ICP-MS has and continues to also be used to screen speleothems to discern if the speleothems show potential for dating (Pickering et al., 2011b, 2019; Pickering and Edwards, 2021). LA-ICP-MS is preferred for this purpose because it is faster and the most qualitative way to document U and Pb concentrations and distributions on speleothems (Pickering and Edwards, 2021). The need for this screening arose because flowstones particularly have high impurity content (detrital common lead and Th) which makes it difficult to date (Richard and Dorale, 2003). LA-ICP-MS has had a short coming in dating small speleothems of Wonderwerk cave which may not be in the Cradle but is hosted in the Transvaal dolomitic bedrock.

U/Th is also a successful method used in the Cradle (see Pickering et al., 2007; Dirks et al., 2017; Robbins et al., 2021). Cosmogenic nuclide burial dating is also a well-suited method for dating clastic sediments in the Cradle (Partridge et al., 2003; Dirks et al., 2010, 2016; Gibbon et al., 2014; Granger et al., 2015; Makhubela and Kramers, 2017; Makhubela et al., 2017b; Kuman et al., 2021; Granger et al., 2022). This method has been used to date the fossil-bearing deposits and quantify landscape evolution (Makhubela et al., 2019).

Another method being used in the Cradle currently is the $^{26}Al/^{10}Be$. Cosmogenic nuclides can be used to estimate the length of time that a rock or sediment has been exposed at, or near, the Earth's surface (Gosse and Phillips, 2001; Dunai, 2010; Granger et al., 2013, 2015). *In situ* cosmogenic

nuclides are produced by secondary cosmic radiation that bombard the Earth's surface and interact with the atomic nuclei in minerals. The most used cosmogenic isotopes for geological dating are the stable ^{3}He and ^{21}Ne, and the radioactive ^{10}Be, ^{26}Al and ^{36}Cl (Dunai, 2010). In rocks, most of the cosmic radiation is absorbed within the few upper meters of the surface as the cosmic ray flux decreases exponentially with depth (Gosse and Phillips, 2001). The production rate for a particular cosmogenic nuclide varies with latitude, elevation, depth, and rock density. The concentration of cosmogenic nuclides in a mineral grain (from a rock sample or a fluvial sediment) is a function of the rate with which that grain has been brought to the surface, a process referred to as denudation, and is linked to the rate of erosion (Lal, 1991; Granger and Muzikar, 2001; Gosse and Phillips, 2001). That is, higher concentrations of nuclides imply longer exposure times near the surface and, therefore, slower erosion rates and exposure ages for minerals are inversely proportional. Cosmogenic radionuclides decay at a rate given by their decay constant, and the rates of production and decay can be combined to give the total concentration of cosmogenic radionuclides in a sample, which is a function of age. This allows for burial dating in cases where previously exposed sediment is now buried at depth where production does not take place anymore, but decay is dominant. This method has been used to date fossil bearing deposits (Patridge et al., 2003; Gibbon et al., 2014; Granger et al., 2015; Kramers and Dirks, 2017; Makhubela et a., 2019; Granger et al., 2015, 2022) such as the ones in Malapa. Cosmogenic nuclide has been used in Wonderwerk cave (Shaar et al., 2011) as well. Although the method is gaining momentum in being established as a reliable dating method in the Cradle, it has some shortcomings as well. In most cases in the Cradle, cosmogenic nuclide is used on the clastic sediments where fossil deposits are hosted. For example, this method was used in Sterkfontein to date Member 4 (Granger et al., 2022). Member 4 had already been dated using U-Pb on the flowstones considered to bracket the bottom and top of the

deposit (Pickering and Kramers, 2010; Granger et al., 2015). The proposed relationship of how the flowstone is directly related to the deposit has been put into question and so the interpretation of the dating of Member then relied heavily on cave infill stratigraphy (Granger et al., 2022). The burial age presented by Granger et al. (2022) of 3.41± 0.11 Ma is too different from that presented by Granger et al. (2015) of 2.03 ± 0.06 Ma and by Pickering and Kramers (2010) of 2.65 ± 0.18. The Cosmogenic nuclide age was much older than the ages determined from ESR (fossil teeth), paleomagnetism and U-Pb on flowstones. The age was highly contested with one reason being that the age is subjected to error introduced by reworking of the sediment from higher unconsolidated deposit in the cave (Granger et al., 2022). The claim for such error was dismissed due to lack of evidence to support it but this case study did show the capabilities of the method and how it highly depends on stratigraphic interpretations. Stratigraphic studies of cave infill thus become important in interpreting cosmogenic dates.

Palaeocave allogenic fill in the Cradle is broadly confined between ~3.2 Ma and ~1 Ma (Herries et al., 2013; Gibbon et al., 2014; Pickering et al., 2019). Deposits from the eleven sites listed in table 4 have been dated mostly using paleomagnetism, U-Pb and cosmogenic nuclide burial dating, and the obtained ages in most sites are highly contested. Because the forementioned sites are Plio-Pleistocene in age, listing individual ages and their stratigraphic context will go beyond the scope of this thesis. There are papers to read that summarize individual ages at these sites, especially those that used U-Pb on flowstones such as Pickering et al., 2007; Pickering et al., 2011b; Pickering et al., 2019 and many more. For example, one can find summary of dated members at Drimolen, Bolt's farm, Coopers cave, Haasgat, Malapa, Sterkfontein, and Swartkrans in Pickering and Edwards (2021). Age summary of (i) Gladysvale can be found in Pickering et al. (2007), (ii) Rising Star cave in Dirks et al., 2015; Dirks et al., 2017; Robbins et al., 2021, (iv) Kromdraai in Thackery

et al., 2002; Braga et al., 2017, Forvel and Frerebeau, 2023 (v) Gondolin in Herries, 2022, (vi) Minnars cave in Gommery et al., 2012

CHAPTER 3: MATERIALS AND METHODS

3.1 Samling methods and materials

Field work was undertaken to sample the newly exposed deposit and sampling focused mostly inside Pit 2 to get more samples in that area as per the study objectives. Sampling was done moving from the area demarcated as B to A heading towards the Main pit. This kind of sampling was chosen because in Pit 2, some of the sediments appeared distinct from the reported peloidal grainstone in terms of grain size, colour, constituent type, and overall appearance indicating that facies F may not be homogenous as previously ascribed by Pickering et al. (2011a).

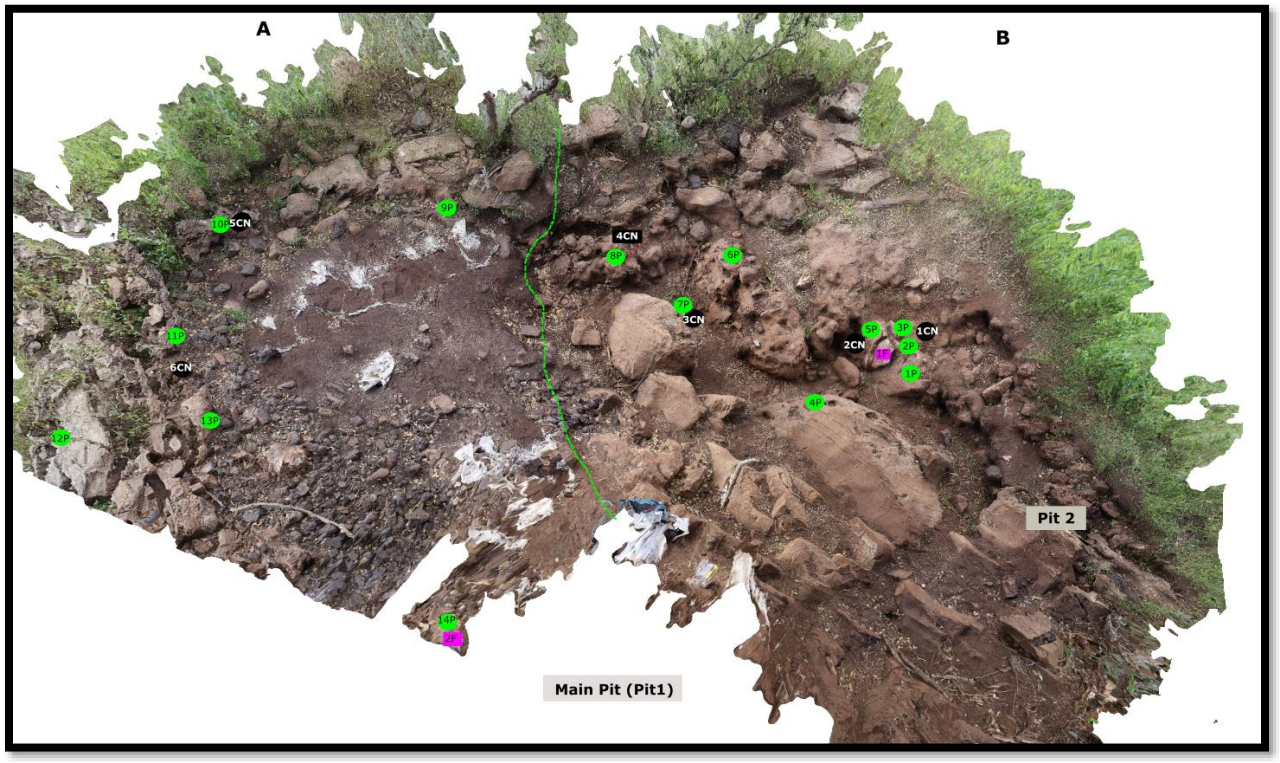


Figure 6: Photogrammetry photo of the newly exposed fossiliferous and barren deposits at Malapa. A) The newly exposed deposits and B) Pit 2 which was targeted to sample facies F. This image

shows the concentration of 8 samples taken in Pit 2 and 6 samples taken in the recently excavated area (A).

The samples used in this study were sampled from the main pit, pit 2, and the newly exposed deposits. A total of seventeen clastic samples were collected for petrographic analysis. To get a fair representation, samples were taken close to each other next to the flowstone 2 to ensure that visible difference in grain size observed in the field was properly represented. The rest of the samples were sampled at intervals the where visible change in grain size or rock type were observed. These samples are hereafter referred to as; MLP1P, MLP2P, MLP3P, MLP4P, MLP5P, MLP6P, MLP7P, MLP8P, MLP9P, MLP10P, MLP11P, MLP12P, MLP13P, MLP14P, MLPFE1, MLPFF1 and MLPFF2 (Fig. 6; Fig 7). Sample MLP1P to MLP8P were collected in pit 2 and MLP9P to MLP14P were collected in the newly exposed deposits area. MLPFE1, MLPFF1, and MLPFF2 were sampled from known facies in the main pit i.e., facies E and F respectively. These samples were used as reference samples only. Two speleothem samples (flowstones) were collected for geochronology, i.e., MLP2F and MLP3F (Fig. 6; Fig 7). Six more samples were collected for the cosmogenic nuclide burial dating method i.e., MLP1CN, MLP2CN, MLP3CN, MLP4CN, MLP5CN, and MLP6CN. Quartz rich sediments were targeted to sample for the cosmogenic nuclide burial dating. Five samples are muddy sandstones with the sixth one is a quartz vein. Table 5 shows sample name and the type of lithology it falls under.

Table 5: This table shows the seventeen samples used in this study and the type of lithology they are. The lithologies were defined using field observations and petrographic descriptions presented in chapter 3. MLPFE1, MLPFF1 and MLPFF2 were identified by Dirks et al. (2010) Pickering et al. (2011a)

Sample name	Lithology	Locality
MLP1P	Peloidal limestone	Pit 2
MLP2P	Muddy limestone	Pit 2
MLP3P	Muddy limestone	Pit 2
MLP4P	Calcareous sandstone	Pit 2
MLP5P	Calcareous sandstone	Pit 2
MLP6P	Calcareous sandstone	Pit 2
MLP7P	Micritic limestone	Pit 2
MLP8P	Sandstone	Pit 2
MLP9P	Sandy limestone	Newly exposed deposits
MLP10P	Calcareous sandstone	Newly exposed deposits
MLP11P	Calcareous sandstone	Newly exposed deposits
MLP12P	Sandy limestone	Newly exposed deposits
MLP13P	Calcareous sandstone	Newly exposed deposits
MLP14P	Peloidal limestone	Newly exposed deposits
MLPFE1	Calcareous sandstone	Pit 1, facies E
MLPFF1	Alternating peloidal grainstone and sandy peloidal grainstone	Pit 1, facies F

MLPFF2	Alternating peloidal grainstone and sandy peloidal grainstone	Pit 1, facies F
MLP2F	Flowstone 2	Pit 2
MLP3F	Flowstone 3	Newly exposed deposits
MLP1CN	Muddy sandstone	Pit 2
MLP2CN	Muddy sandstone	Pit 2
MLP3CN	Muddy sandstone	Pit 2
MLP4CN	Breccia	Pit 2
MLP5CN	Quartz vein	Newly exposed deposits
MLP6CN	Muddy sandstone	Newly exposed deposits

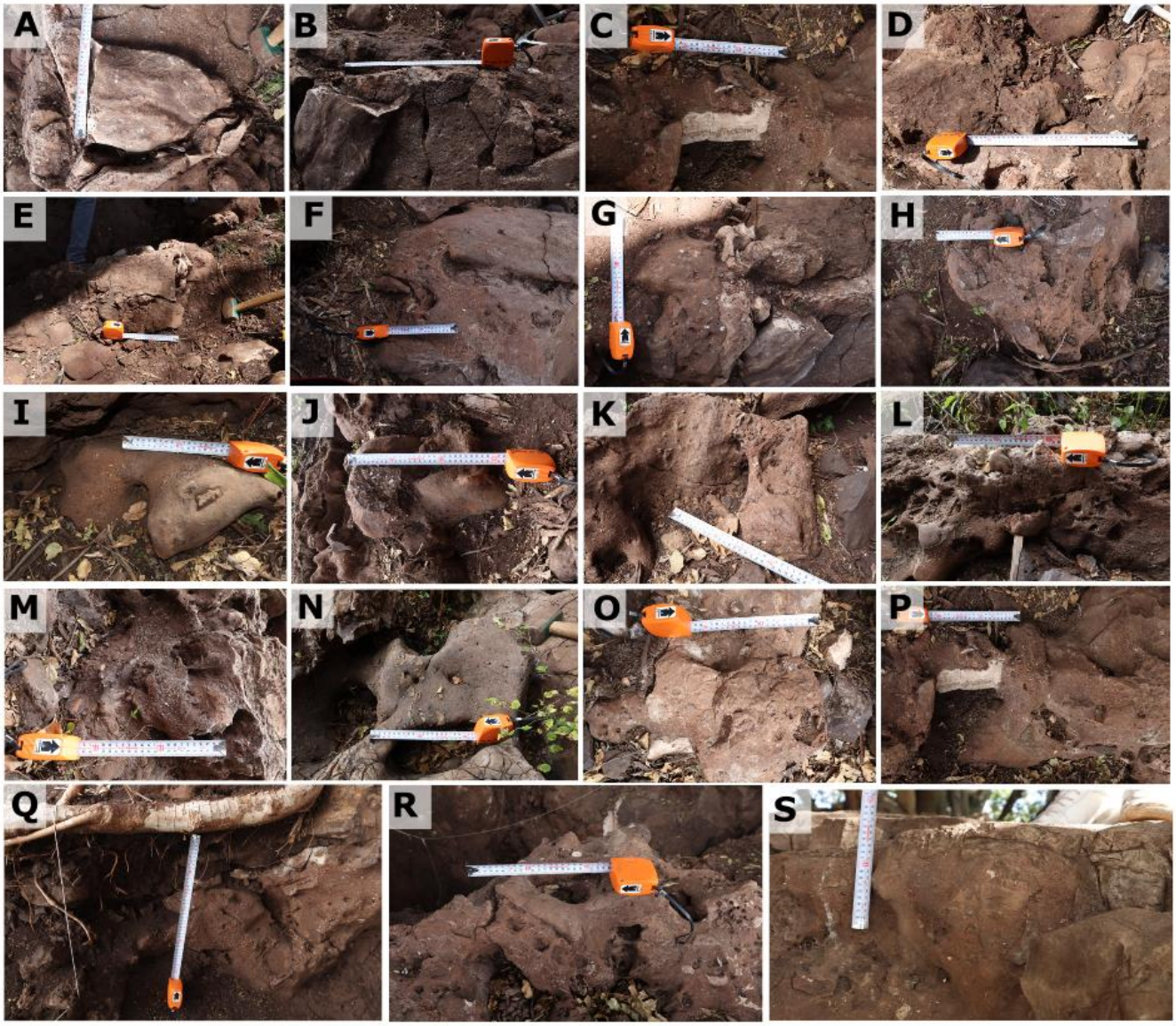


Figure 7: Composite image showing areas where individual samples were sampled. For a 3-D visualization, revisit figure 3. A and C- are samples of MLP2F and MLP3F respectively. B, D - P are samples MLP1P, MLP2P - MLP14P and Q-S are MLPFE1, MLPFF1, and MLPFF2 respectively. Looking at images N, J and B, it is obvious that these sediments are different. N is a fine-grained deposit with dolomite blocks, J is medium-coarse grained clastic deposit and B is composed of peloids. Image created by Dakalo Maphanda. Photos cred: Paloma de la Peña

3.2 Petrology methods

3.2.1 X-ray fluorescence analysis

X-ray fluorescence (XRF) is considered a well-established analytical technique used for determining the bulk chemical composition of a sample (Loubser and Verryn, 2008). This technique can be used on un-prepared samples (a portable XRF spectrometer directly to the sample) or on prepared samples such as loose powders, pressed pellets, and fused beads (Michaud, 2015). It works by measuring emitted fluorescent/ secondary X-rays from a sample that is excited by a primary source (Brouwer, 2006). Each element present in the sample has unique fluorescent X-ray characteristics which form the basis for determining elementary chemistry (Nayak and Singh, 2007). Sample preparation for XRF requires the sample to be crushed, milled in a tungsten/ hardened steel milling pot, and dried where necessary (Loubser and Verryn, 2008).

For this study, all seventeen petrographic samples were prepared at the School of Geography, Archaeology, Environmental Studies (GAES) crushing and milling lab at Wits. The samples were put inside a carbide steel mill for 30 seconds to be ground until they became fine powder. Measurements were carried out at UJ on borate fusion discs using the PANalytical MagiX PRO XRF spectrometer. To prepare the borate fusion discs, approximately 1 g of the finely milled powder of each sample was dried in an oven for 24 hours at 105 ℃. The dried material was ignited in a furnace for 30 minutes at 930 ℃ to measure the loss on ignition (LOI). The LOI material was used to carry out the preparation of the borate fusion discs as follows: 0.7 g of the sample after LOI was mixed with 0.1 g $LiNO_3$. This mixture was further mixed with 6 g of fused anhydrous 50/50 flux (lithium borates with lithium boride: 49.75 % $Li_2B_4O_7$, 49.75 % $LiBO_2$, 0.50 LiBr) and transferred to Pt-Au crucibles. The fusion was carried out by heating to 1050 ℃ using TheOX® electric fusion machine.

3.2.2 Scanning Electron Microscopy- Energy Dispersive Spectroscopy (SEM-EDS)

SEM-EDS is an elemental microanalysis method used to identify and quantify elements in a sample (Newbury and Ritchie, 2013). This analysis is capable of qualitative (elemental identification) and quantitative results with high accuracy and precision (Richie et al., 2012). SEM-EDS work was done at UJ using the Tescan Vega SEM-EDS setup. The thin sections were carbon coated prior to using SEM-EDS to ensure good image quality and sample conductivity. Carbon coating was conducted using a 230 v Agar Turbo carbon coater, model 208C, at a setting of 4.5 V. SEM was used to take backscattered electron (BSE) images with a beam intensity of 13-14 kV and beam accelerating voltage of 20kV. EDS analyses (Point and ID and elemental mapping) were conducted using the Aztec Software (Aztec 2.2. Oxford Instruments Nanotechnology Tools Limited. 2010-2013).

3.2.3 Petrography

Covered, polished thin sections of the petrographic samples were made at the University of the Witwatersrand (WITS) rock cutting laboratory. Polished thick sections (100µm) of flowstones were also made for Laser Ablation Inductively Coupled Plasma Mass Spectrometry (LA-ICP-MS) geochronology analysis. A batch of twelve samples of uncovered and polished thin sections were made at the University of Johannesburg (UJ) for petrography and Scanning Electron Microscopy-Energy Dispersive Spectroscopy (SEM-EDS) analysis. An Olympus BX41 U-25LBD optical microscope was used for petrographical descriptions at WITS. Geochemical analyses to identify the mineral and elementary composition of the samples were carried out using SEM-EDS and X-ray fluorescence Spectroscopy (XRF) at UJ. Samples were described following guidelines that can be found in “Petrology of sedimentary rocks” book (Boggs, 2009). The book outlines what do describe in a thin section or hand sample and how to describe using sedimentary accepted

nomenclature from references therein. The samples were described under plane and cross polarized light. Frisia (2015) was used to identify calcite fabrics.

3.3 Uranium lead (U-Pb) dating

Sample MLP1F and MLP2F were dated using U-Pb dating via LA-ICP-MS at Wits in the Earthlab in the GAES building. Flowstone samples were prepared as polished fragments embedded in epoxy resin mounts. They were cleaned in an ultrasonic bath to remove any contaminants. No distinct calcite types and generation or obvious alteration from petrographic studies. U-Th-Pb measurements were carried out in the Earthlab at the University of the Witwatersrand, employing an Applied Spectra (formerly Australian Scientific Instruments) Resonetics Resolution 193 nm ArF excimer (SE 155) system coupled to a Thermo Scientific Fisher sector-field ICPMS (Element XR). The U-Th-Pb measurements were performed in low resolution and electrostatic scanning (E-scan) modes. Acquired data was by single spot analysis (100 µm), using a laser repetition rate of 15 Hz and a fluence of 2 Jcm^{-2}. Total signal acquisition time was 40 seconds, allowing data processing and preparation for the next analysis, and comprising two times 5 seconds of pre- and post-ablation (gas blank) and 30 seconds of ablation measurements. Laser sampling took place in a dual-volume ablation cell (Laurin Technic, Canberra, Australia) using a mixed He-Ar atmosphere and a small volume of N_2 to enhance signal stability and sensitivity. The following gas flows were applied: He (350 ml/min), Ar (1050 ml/min) and N_2 (5 ml/min), respectively. Graphic presentation and calculation of lower intercept ages on a Tera-Wasserburg diagram were carried out using the software ISOPLOT-R (Vermeesch, 2018). For more information on how data reduction was done, please see Appendix A.

3.4 Cosmogenic nuclide burial dating (^{26}Al/ ^{10}Be)

The sample preparation for this analysis is done to purify and concentrate the selected target mineral by physical and chemical preparation (Dunai, 2010). Physical sample preparation includes crushing, sieving, density and magnetic separation whereas chemical sample separation may include froth flotation (Dunai, 2010) (see Figure 8).

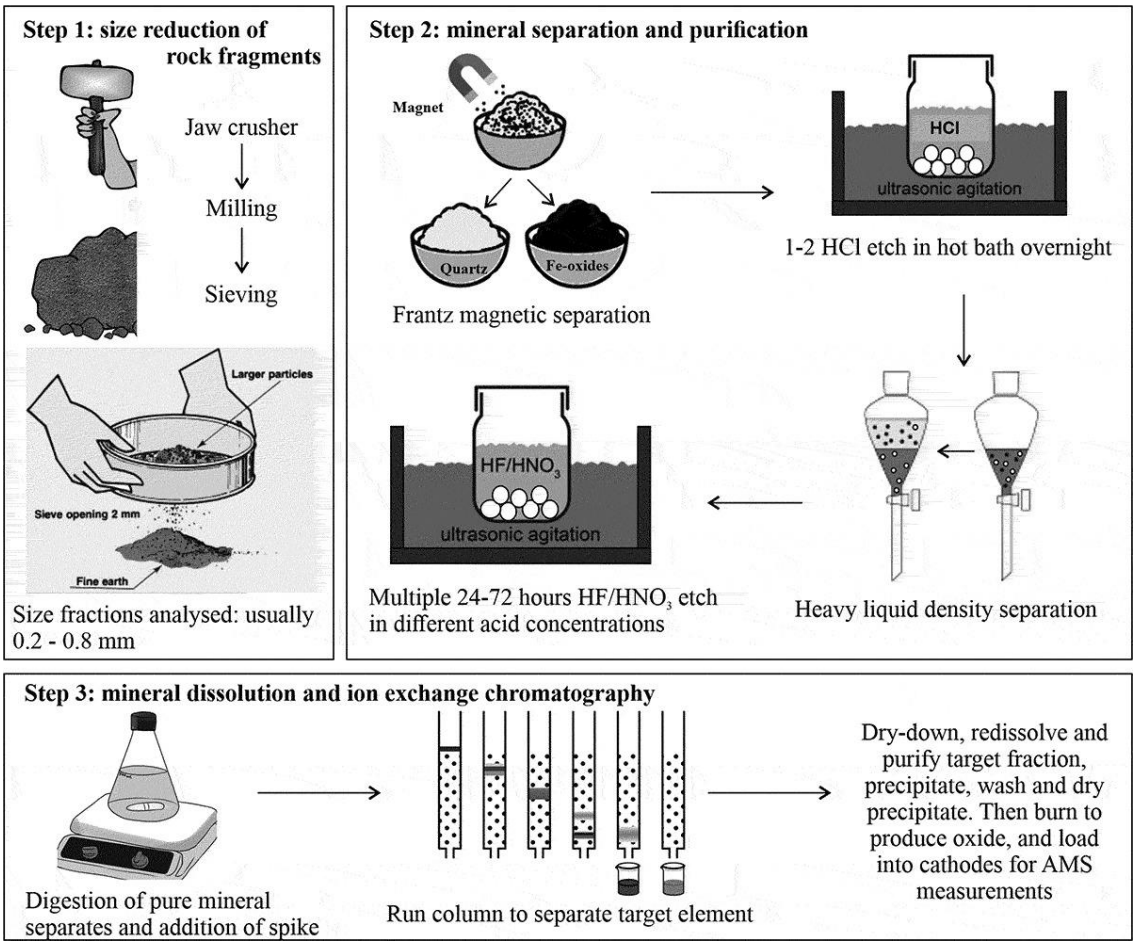


Figure 8: Flow diagram showing generalized and simplified steps of the sample preparation and processing for cosmogenic nuclide analysis (Makhubela et al., 2021).

The cave clastic sediment samples were crushed and sieved to 0.2-0.8 mm size fraction and pre-treated for quartz purification at the University of Johannesburg Spectrum Analytical Services.

Standard methods of heavy liquid and Frantz magnetic separation were used together with a series of leaching using a 50% hydrochloric acid (HCl) and a mixture of 2% nitric acid (HNO_3) and 2% hydrofluoric acid (HF) as described in Makhubela et al. (2021). The semi-pure quartz samples were taken to the Accelerator mass spectrometry (AMS) and isotope research centre, Helmholtz-Zentrum Dresden-Rossendorf (HZDR), Germany, for further sample processing and measurement. Non-quartz minerals were dissolved using hexafluorosilicic acid (H_2SiF_6) and the resulting quartz was treated with HF to remove meteoric ^{10}Be prior to complete dissolution using concentrated HF. Details of the method used are described by Merchel and Herpers (1999). Be and Al were separated using ion exchange columns and precipitated as hydroxides, which were then ignited to oxides at 900–1000 °C. Thereafter, targets were pressed for measurement of $^{10}Be/^{9}Be$ and $^{26}Al/^{27}Al$ ratios at DREAMS facility of HZDR (Rugel et al., 2016). A single processing blank was included and yielded $1.63 \pm 0.0475 \times 10^{-13}$ $^{10}Be/^{9}Be$ and $7.87 \pm 2.49 \times 10^{-15}$ $^{26}Al/^{27}Al$. The ^{10}Be (N_{10}) and ^{26}Al (N_{26}) concentrations and the burial ages were calculated using methods of Granger (2014).

CHAPTER 4: PETROLOGY AND GEOCHEMISTRY RESULTS

Cave sediments of Malapa have been described by Dirks et al. (2010) and Pickering et al. (2011b). There isn't a vast variety of lithologies to encounter at this site, but the facies of each lithology are the focus of the study. From previous studies, Malapa cave sediments compromise mudstones, clastic/calcareous sandstones, and plain/ sandy peloidal grainstone. The 17 petrographic samples are henceforth described with a focus on texture, fabrics, grain size, sorting, porosity, grain type and shape, diagenetic features, and matrix composition. The samples were named according to their grain size (classification of siliciclastic sedimentary rocks). The grain type observed in general are peloids, dolomite, chert, quartz, iron-manganese oxyhydroxides (Fe-Mn-oxyhydroxides), and calcite. Below are sample descriptions that include field descriptions, petrographic descriptions, SEM-EDS, and XRF data. Lithologies identified: peloidal limestone, muddy limestone, calcareous sandstone, micritic limestone, and sandy limestone.

4.1 Sample descriptions

4.1.1 MLP1P: Peloidal limestone

The sample is composed of spherical micritic peloids (with some minor irregularly shaped grains) and calcite cement (Fig. 9). The sample is coarse-grained, moderately sorted, and has a few pore spaces. Most of the peloids are dark brown well-rounded grains. They range from <500 µm to 4 mm in size. The calcite cement exhibits a blocky sparite texture which is white to grey in colour. SEM-EDS analysis (BSE and EDS composite images) shows that at <500 µm, there are quartz grains within the calcite cement and the peloids. There are no concentric growth rings within the peloids, and they lack an internal structure. Although rare, some grains have a Fe-Mn oxide nucleus (Fig. 9C) which is a bit over 100 µm in size and surrounded by a thin layer of calcite.

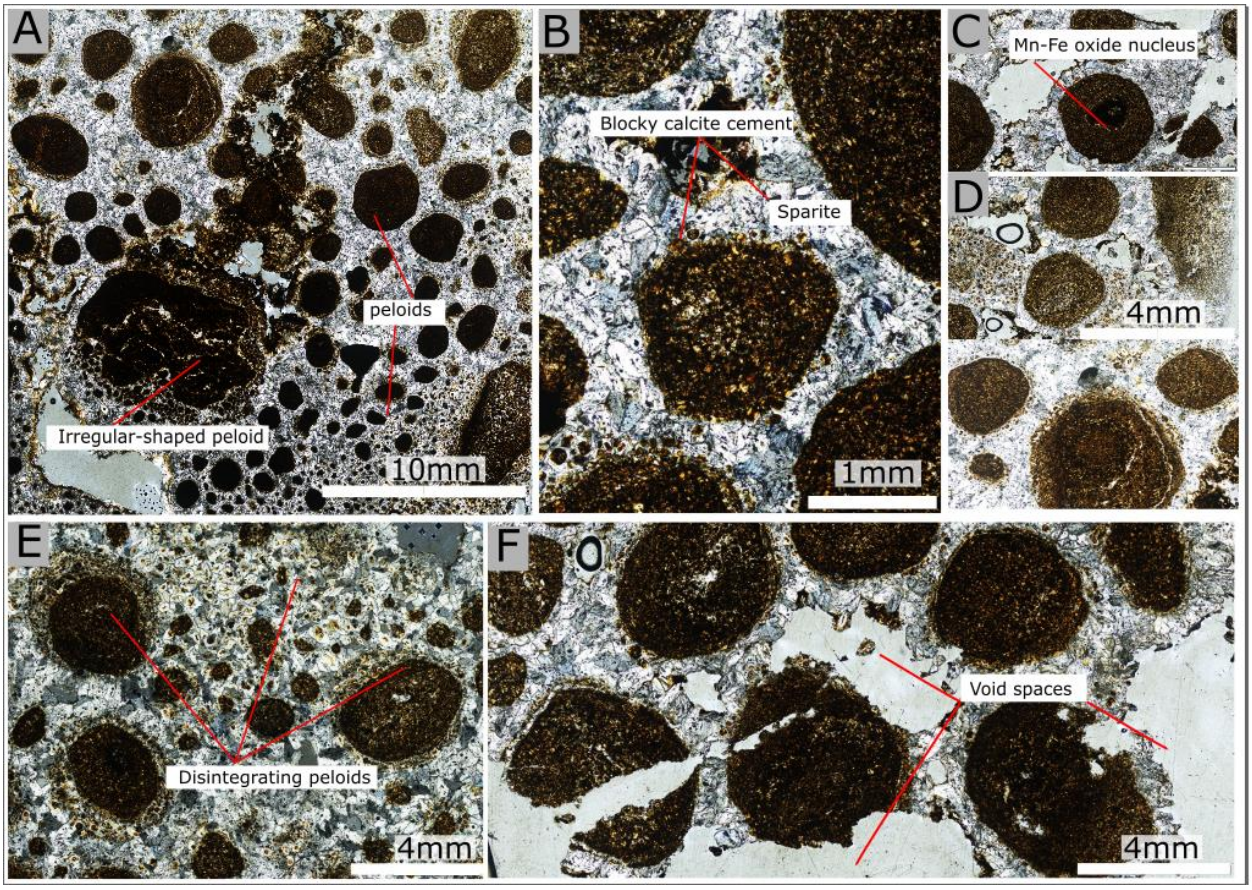


Figure 9: Petrographic images of MLP1P in cross polarized light (XPL) showing the type of grains in A. B shows the blocky sparite texture cementing the micritic peloids. The peloids in this sample are semi-uniform in shape with some void spaces between them as shown in F. In parts of the sample, the peloids start to disintegrate as shown in E. C shows a peloid grain with a nucleus that is almost rhombic.

4.1.2 MLP2P: Muddy limestone

The sample is composed of patches of blocky sparite, peloids, quartz grains, peloidal Mn-nodules, coated chert, and void spaces (Fig. 10). The sample is moderately sorted, fine-medium grained and has few (<1%) void spaces. There are fossils present. The calcite that is making up the sample forms discontinuous “threads” and patches around the other grains. It also forms thin veins cross

that crosscut the sample. The peloids are micritic as MLP1P peloids but are less spherical and have disintegrated more into micrite groundmass in most of the sample. The peloids grain size is in the same range as MLP1P i.e., <500 µm to 4 mm. The Mn-nodules, quartz grains, coated chert grains, and aggregate grains are observed at high magnification, they range from <200 µm to 2.5 mm in size.

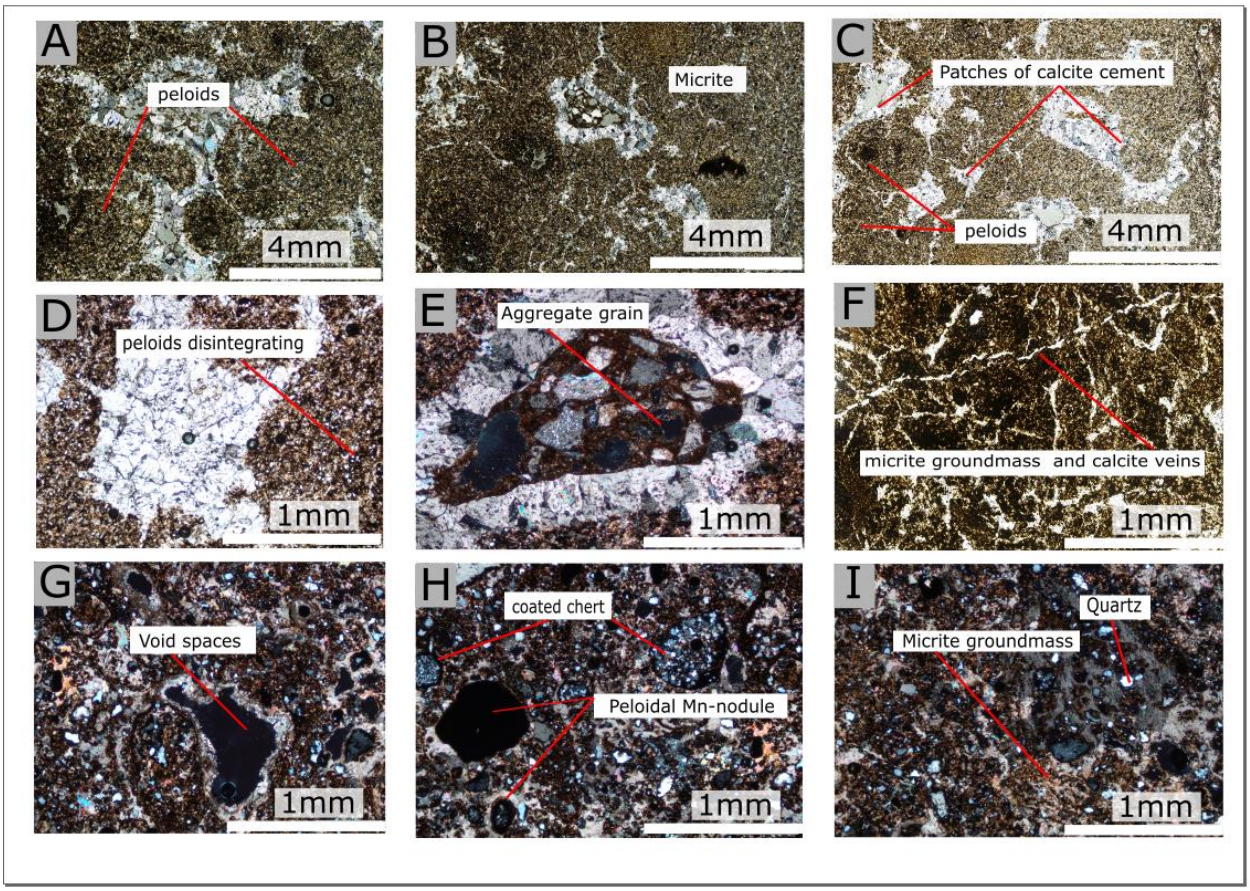


Figure 10: XPL micrographs of MLP2P showing the textures in the sample. A-C shows peloidal texture with some peloids fully disintegrated to form micrite groundmass. Calcite occurs in two forms in the sample i.e., as veins (F) and as patches of blocky cement (C-D). Other grains such as chert (G, H), quartz (I) Mn-nodules(H), and aggregate grins (E) are also shown.

4.1.3 MLP3P: Muddy limestone

This sample is similar to MLP1P in terms of composition. It is composed of spherical peloids, and the interstitial matrix is the isopachous sparite (Fig. 11). The sample is coarse-grained and moderately sorted. The peloids are more spherical than MLP2P but not as defined as MLP1P. The peloids are fractured but no veins could be identified. There are some pore spaces; though not many, they are extensive where present.

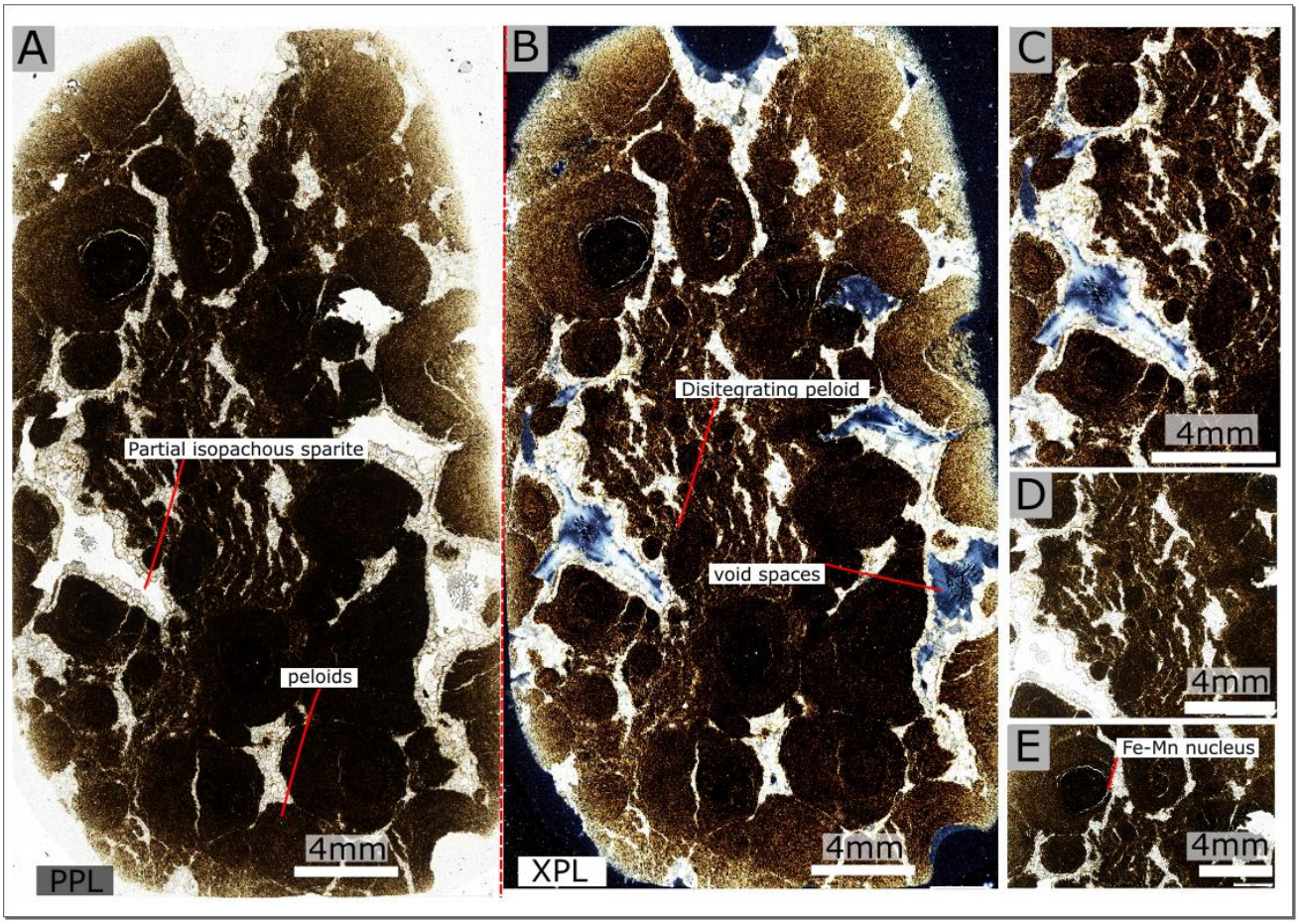


Figure 11: Petrographical images of MLP3P showing a peloidal texture, and micrite groundmass forming as peloids disintegrate (B). C-E shows in the plane polarized light micrograph, the peloid with a nucleus, the relationship between peloids and disintegrating peloids. The calcite forms a sparite cement, but it occurs as a partial isopachous matrix around and in between peloids.

4.1.4 MLP4P: Calcareous sandstone

The sample is composed of quartz, Mn-Fe oxides grains, micrite matrix, chert, and minor calcite clasts (Fig. 12). This allochemical sample is poorly sorted and coarse-grained with little to no pore spaces. The chert grains occur as angular intraclasts, some grains are thinly coated with Mn-Fe oxides. Chert grains range average between 990 µm to 1580 µm although some got to a few millimeters long. Chert grains are in abundance compared to quartz and calcite. There are fossils present.

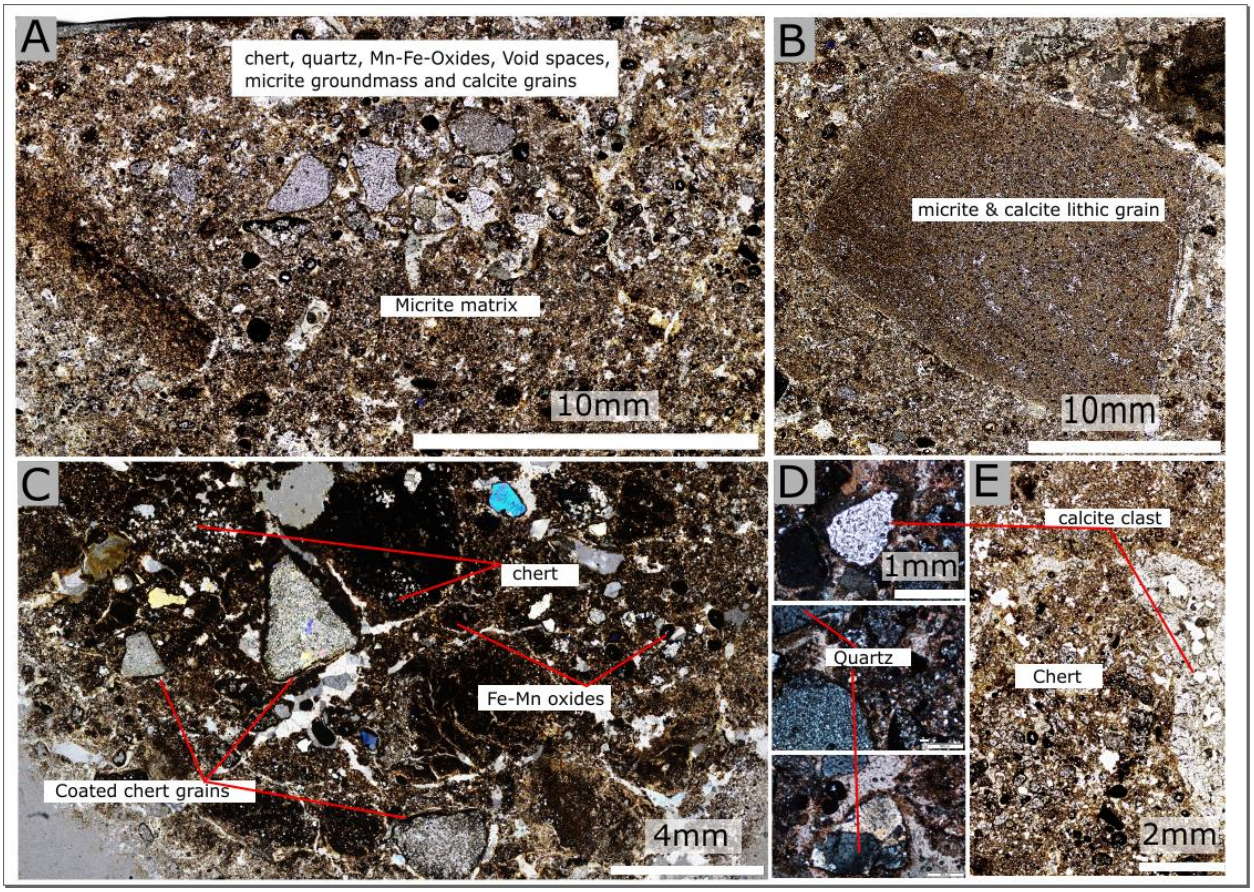


Figure 12: Micrographs of MLP4P showing a poorly sorted sample that is predominately composed of coarse clasts of chert, quartz, Mn-Fe oxides, and a fine groundmass of micrite. A, B, and E show the grain types in ppl, and C and D show the coating of chert in XPL.

4.1.5 MLP5P: Calcareous sandstone

The sample is composed of a micrite matrix, calcite blocky cement, rectangular and angular micrite clasts, chert, void spaces, quartz, Mn-nodules, and calcite grains. The sample is poorly sorted and medium-coarse-grained. This sample is very porous and is fossilized. Most grains are moderately rounded, but some are very angular (Fig. 13J, 13A). The micrite matrix is light brown to dark brown in color. Micrite, calcite, and quartz grains vary in size, but they range from <500 µm to >10 mm. This sample has less chert in terms of abundance and size than MLP4P.

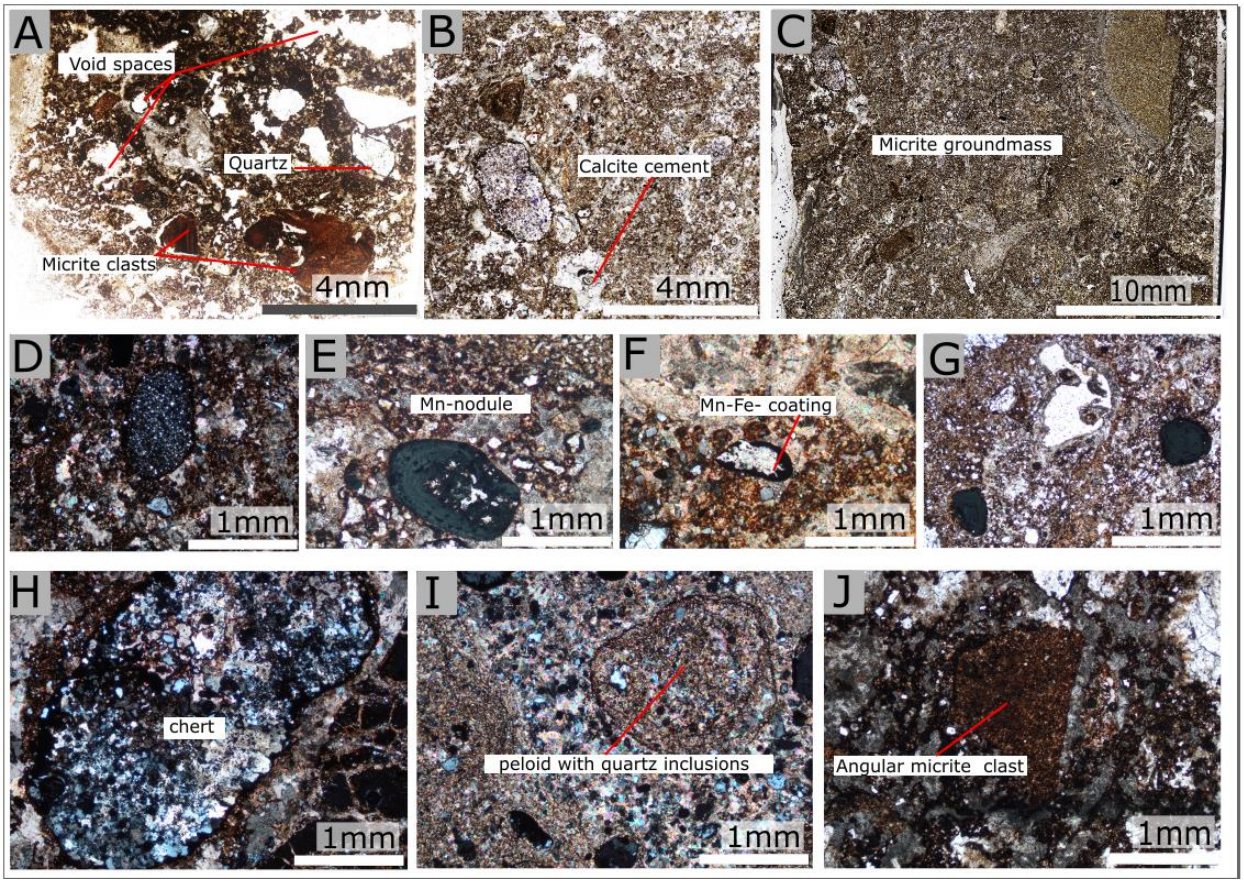


Figure 13: Petrographical images of MLP4P. This sandstone is matrix supported as shown in (C). The most abundant grain is chert and micrite clasts which are rounded and coated (D, E). The

sample has voids more than the previous sample (A). Some remnant peloidal textures can be seen with quartz inclusions (I). Micrographs G & E (PPL) and A, B, C, D, F, H, I, and J (XPL).

4.1.6 MLP6P: Calcareous sandstone

This is a binary sample composed of two separate "phases" in terms of constituents and grain size. One part of the sample is composed of micrite groundmass and long, thin calcite veins. There is one thick vein with Mn-Fe-oxides inside it. The veins all join each other in the sample. This part of the sample is fine-grained and has no pore spaces. The other part of the sample is composed of a micrite matrix, quartz grains, Mn-Fe- oxides, thinly coated chert, Mn-nodules with quartz nucleus, calcite grains, and coated calcite grains (Fig. 14). Most grains are sub-rounded to rounded. This part is coarse-grained and poorly sorted. About 45% of the grains are coated chert grains followed by peloidal Mn-nodules (20%). The rest of the sample is micrite groundmass and other accessory grains mentioned.

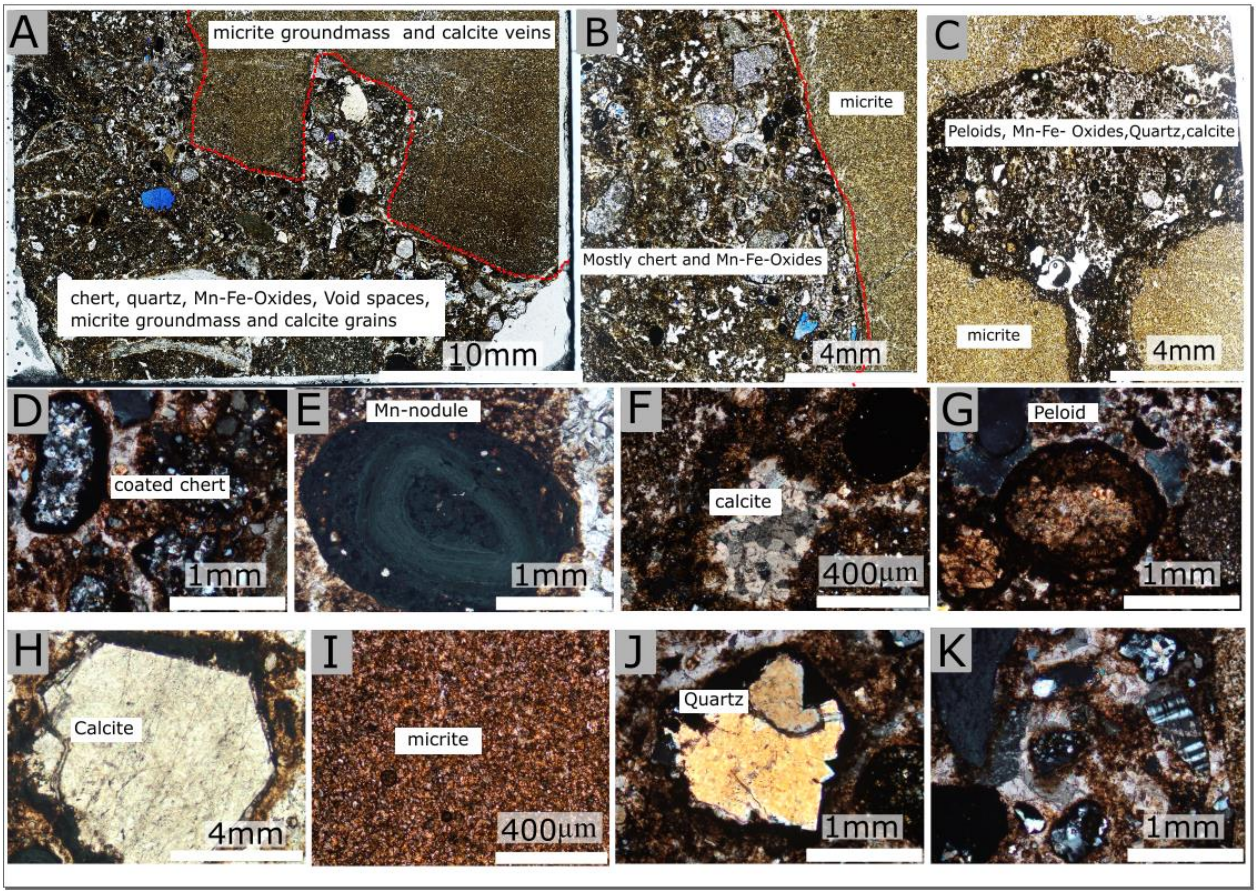


Figure 14: Micrograph of MLP6P showing a binary texture. This binary sample of Calcareous sandstone as shown in A, B, and E is texturally challenging as it is made up of two phases. Most of the grain types can only be seen at low magnification (1 mm and less) (D- K). All images (A-K) are in XPL except for E which is in PPL.

4.1.7 MLP7P: Micritic limestone

The sample is composed of predominantly micrite, calcite grains, and quartz. The sample is fine-grained and has filled pore spaces (Fig. 15). The calcite and chert grains filled in the pore spaces. Grain size is in micrometers for all grains. In terms of chert occurrence, chert is smaller here in size compared to chert found in MLP4P, MLP5P, and MLP6P. Micrite is about 75% of the sample, followed by calcite grains at 20% and chert plus quartz at 5%. The sample is fossilized.

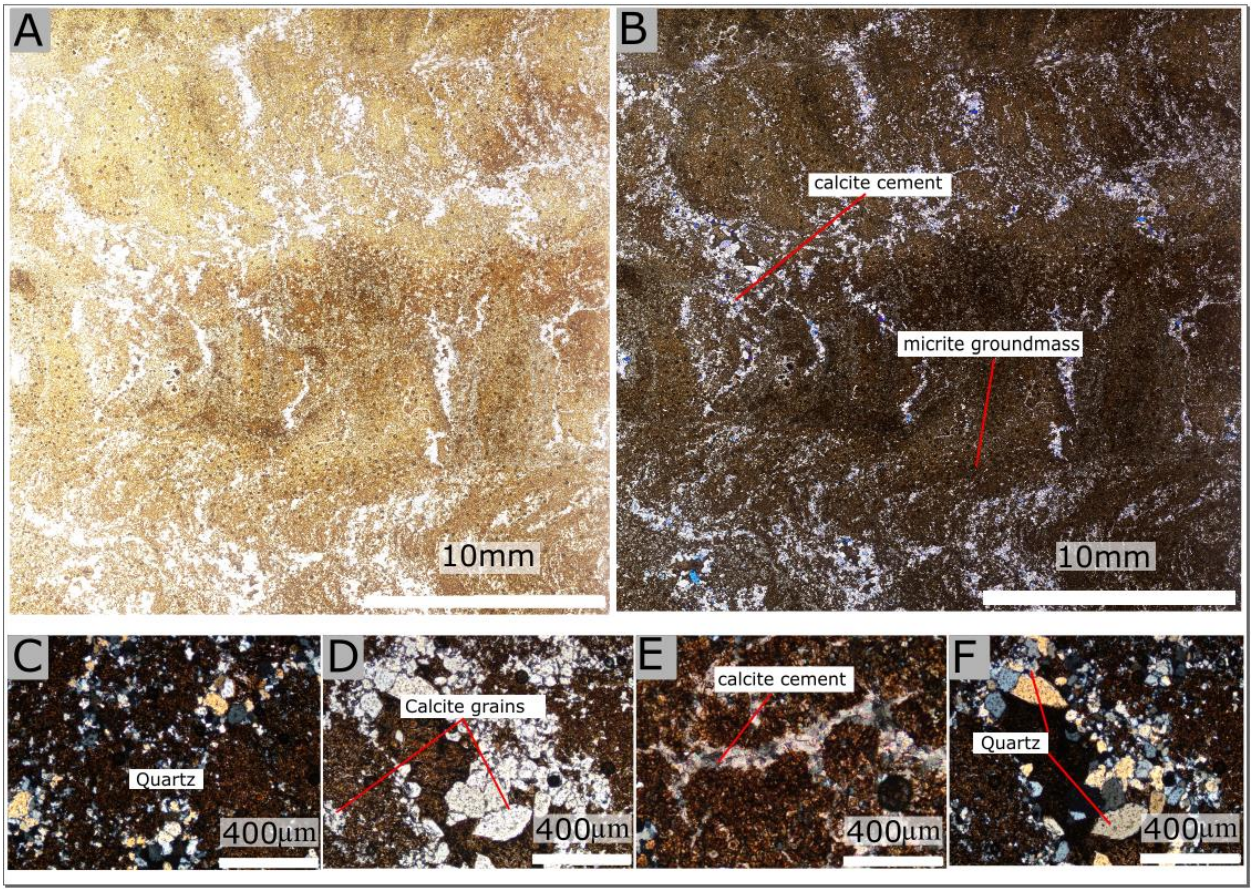


Figure 15: Micrographs of MLP7P showing micrite texture. This is a fine-grained micritic limestone sample as shown in A (PPL) and B (XPL) is composed of quartz grains (C &F), calcite grains (D), and calcite cement (E).

4.1.8 MLP8P: Sandstone

The sample is composed of chert, quartz, micrite matrix, some calcite cement, a few Mn-nodules, and discontinuous quartz veins (Fig. 16). Grain size ranges from 1690 µm to 10 mm. The sample is coarse-grained and poorly sorted. The largest chert grains are found in this sample with an average grain size of >4 mm. All framework grains in this sample are coarse, angular-surrounded, and thinly coated with Mn-Fe-oxide.

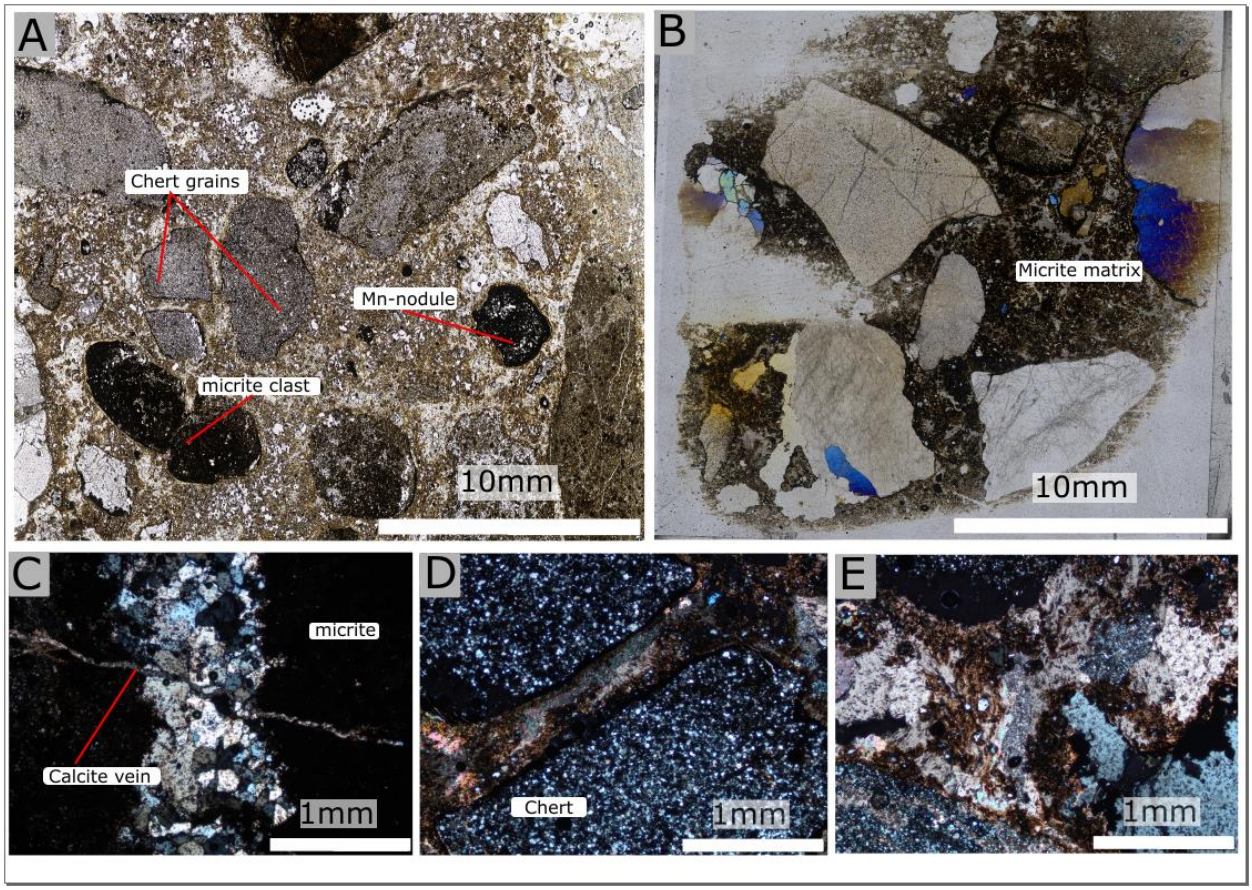


Figure 16: Micrographs of MLP8P. This sample has the coarsest grains in all the samples as seen from A and B. This sample has no peloids, it has thin calcite veins cutting through quartz and chert grains as seen in images C and D. Calcite cement is found in between certain grains with micrite being the matrix (E). A(PPL) and B-E (XPL).

4.1.9 MLP9P: Sandy limestone

The sample is composed of spherical peloids, Mn-nodules, quartz, calcite grains, calcite cement, chert, and Mn-Fe-oxides (Fig. 17). The sample is medium-grained and moderately sorted. Grain size ranges from <500 µm to <5 mm. The average grain size measured for peloids is between <110 µm to 440 µm. The peloids are zoned and rounded compared to the sub-angular chert grains. The

sample has few pore spaces (5%), and quartz is the minority phase with 2% presence. The quartz occurs as microcrystals inside Mn-Fe-oxide or incorporated within the calcite cement.

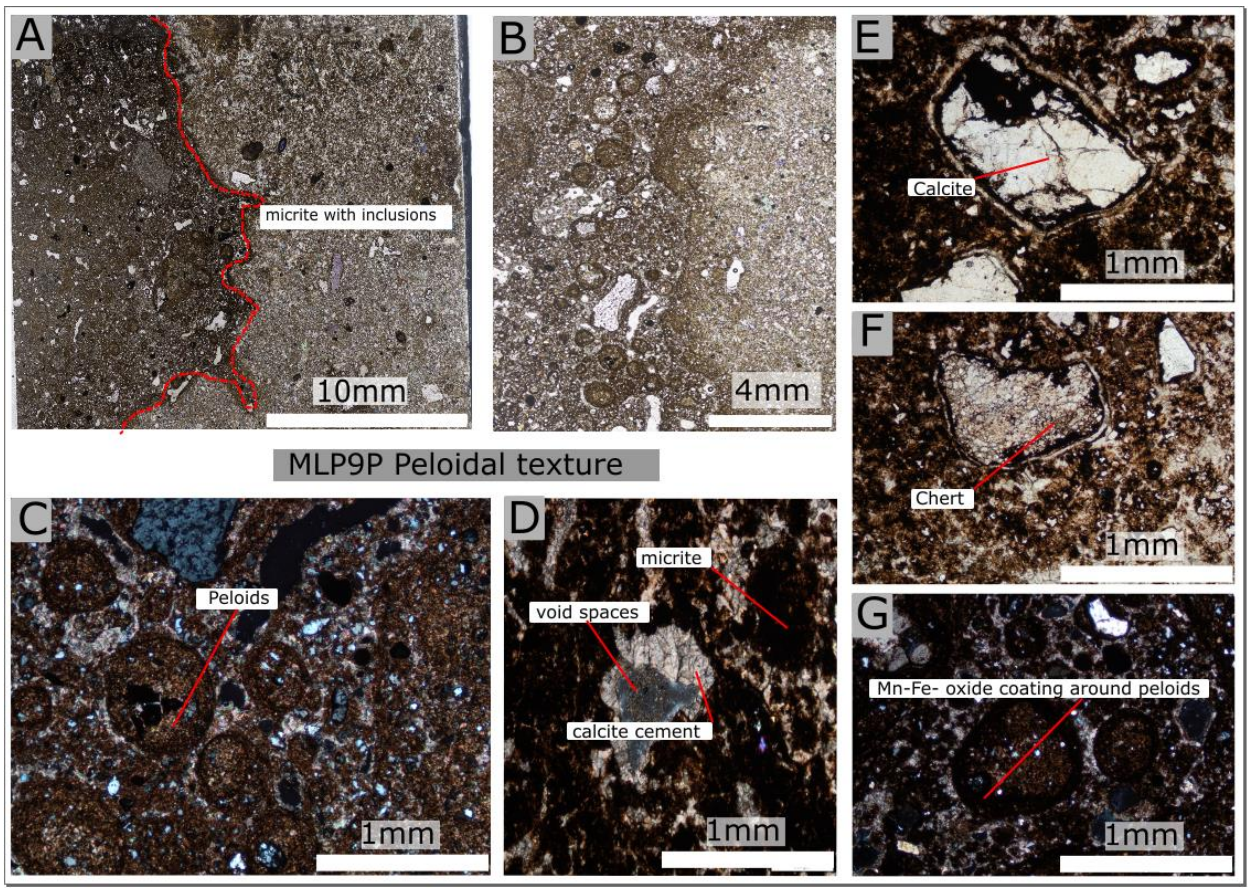


Figure 17: Micrographs of sandy limestone sample. Most of the grain textures are observed at <500 µm scale. This is where the zoning of grains can be seen (E and F). Remnants of calcite blocky cement can be seen (D) and most of the peloids are <500 µm to a millimeter in size (A, B, C, G). From the micrographs, it is clear that detrital grains such as chert are not abundant compared to chemical grains. A, C, D, and G are in XPL, and B, E, and F are in PPL.

4.1.10 MLP10P: Calcareous sandstone

The sample is composed of Mn-Fe-oxides, peloidal Mn-nodules, Calcite grains, quartz, and one chert grain that is coated (Fig. 18). The sample is fine-grained with coarse-grained parts, poorly

sorted, and has few void spaces, and discontinuous veins. Chert grains occur as inclusions or nuclei for calcite or Mn-Fe-oxide grains. Calcite grains (~710 µm in size) are scattered in the sample. Mn-Fe-oxide grains are abundant in this sample occupying 25% of the sample.

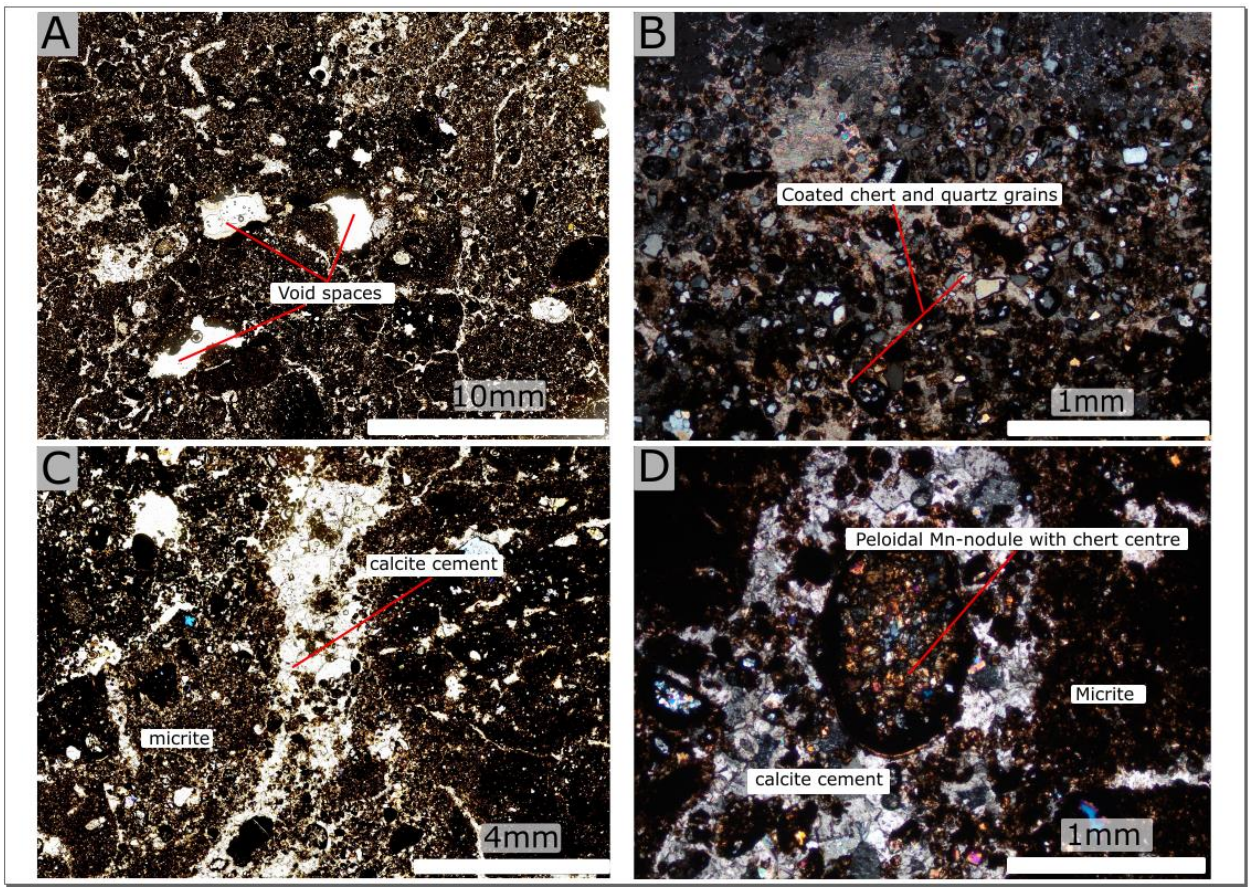


Figure 18: Petrographical imges of MLP10P, the calcreous sandstone. A few Mn-Fe-oxides have completely become Mn-Fe-nodules (B) instead of just being a coat around the grains as observed in D. Even quartz and chert grains that are less than one millimeter in size are coated with the Mn-Fe-oxides. A and C are in PPL and B and D are in XPL.

4.1.11 MLP11P: Calcareous sandstone

This is a coarse-grained, poorly sorted sample. The sample is composed of quartz, peloidal Mn-nodules, Mn-Fe-oxide grains, micrite matrix, micrite clasts, calcite, and chert (Fig. 19). This is a

grain-supported sample that has varying coated grains. The coating of grains is predominately a thin coat all around the grain (either of quartz, calcite, or chert) to a complete replacement to Mn-nodules (Fig. 19B, 19E).

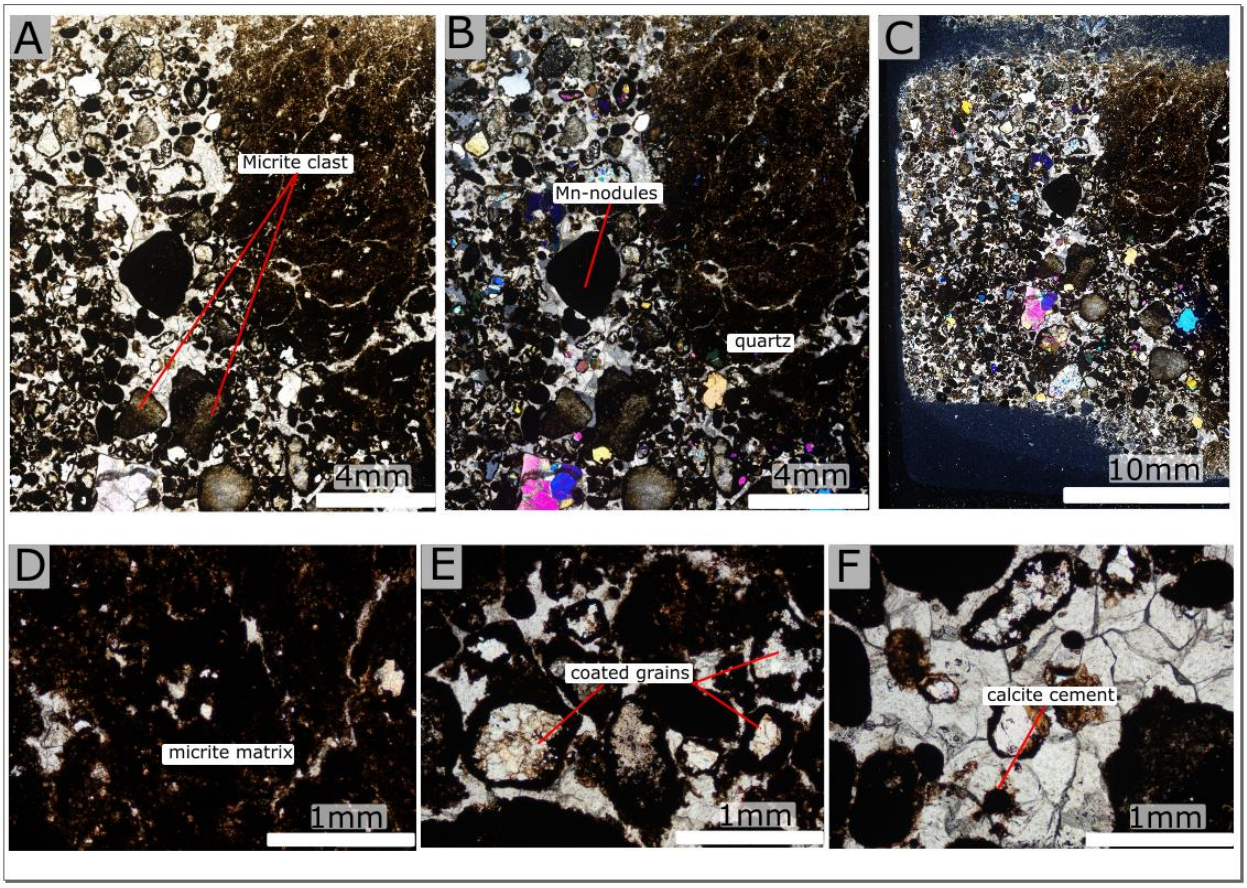


Figure 19: Micrographs of MLP11P showing Mn-F e-oxide grain textures. MLP11P is a calcareous sandstone full of coated grains. The Mn-Fe-oxides are spherical in shape as many have become predominately Mn-nodules (A & B). In the bottom left of image F, micrite can be seen at the edges of the peloidal nodule. Calcite cement (sparite) cements all the coated chert, quartz, Mn-Fe-oxides grains, and calcite grains. A, D, E, and F are in PPL and B & C are in XPL.

4.1.12 MLP12P: Sandy limestone

The sample is composed of a micrite matrix, calcite cement, pore spaces, angular quartz grains, a few Mn-Fe-oxide grains, dolomite, chert, and poorly developed peloids (Fig. 10). This a poorly sorted, coarse-grained sample with large (>4 mm) dolomite clasts (Fig. 20A). Compared to previous samples, this sample has fewer coated grains. The peloids are spherical with quartz inclusions in most grains. They are not as abundant as in other limestone samples.

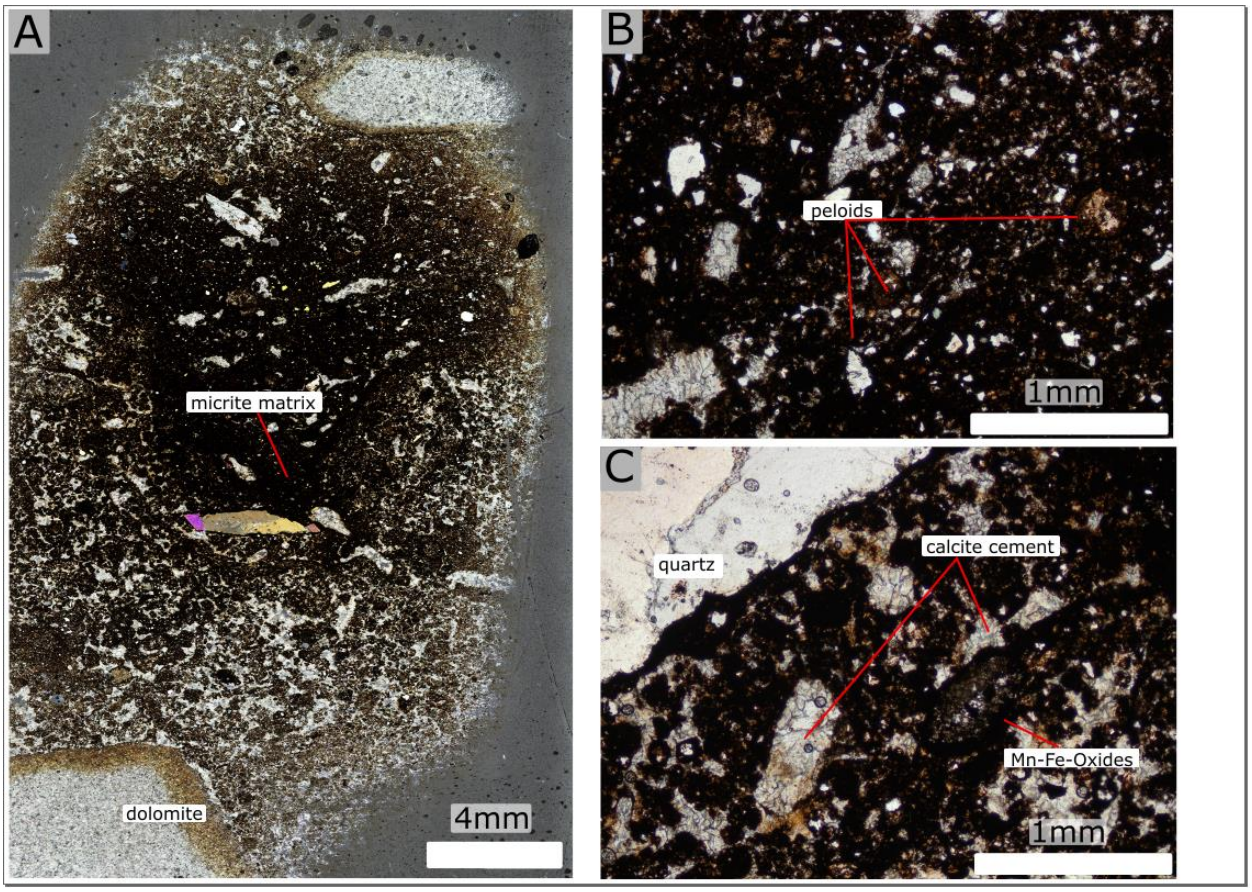


Figure 20: Micrographs of MLP12P showing grain texture. MLP12P is a sandy limestone sample. Although looking at the thin section, one might be tempted to say this is a fine-grained sample because the micrite matrix is abundant. The matrix may be fine-grained, but the clasts are larger than 2 mm in most cases. Peloids in this sample are very few and can only be seen in <500 µm grain size. A is in XPL and B & C are in PPL.

4.1.13 MLP13P: Calcareous sandstone

The sample is composed of a micrite matrix, pore spaces, patches of calcite cement, calcite grains, quartz grains, chert grains, and Mn-Fe-oxide grains (Fig. 21). This is poorly sorted, coarse-grained, and has moderate pore spaces. Calcite cement is usually found surrounding pore spaces either partially or fully enveloped around the pore grain. Chert grains are abundant and coated by a thin-thick Mn-Fe-oxide coat. Quartz grains are occurring as nuclei to Mn-Fe-oxide grains, clasts, and as inclusions within the calcite cement and other grains. Calcite cement occurs as patches and does not form extensive blocky textures.

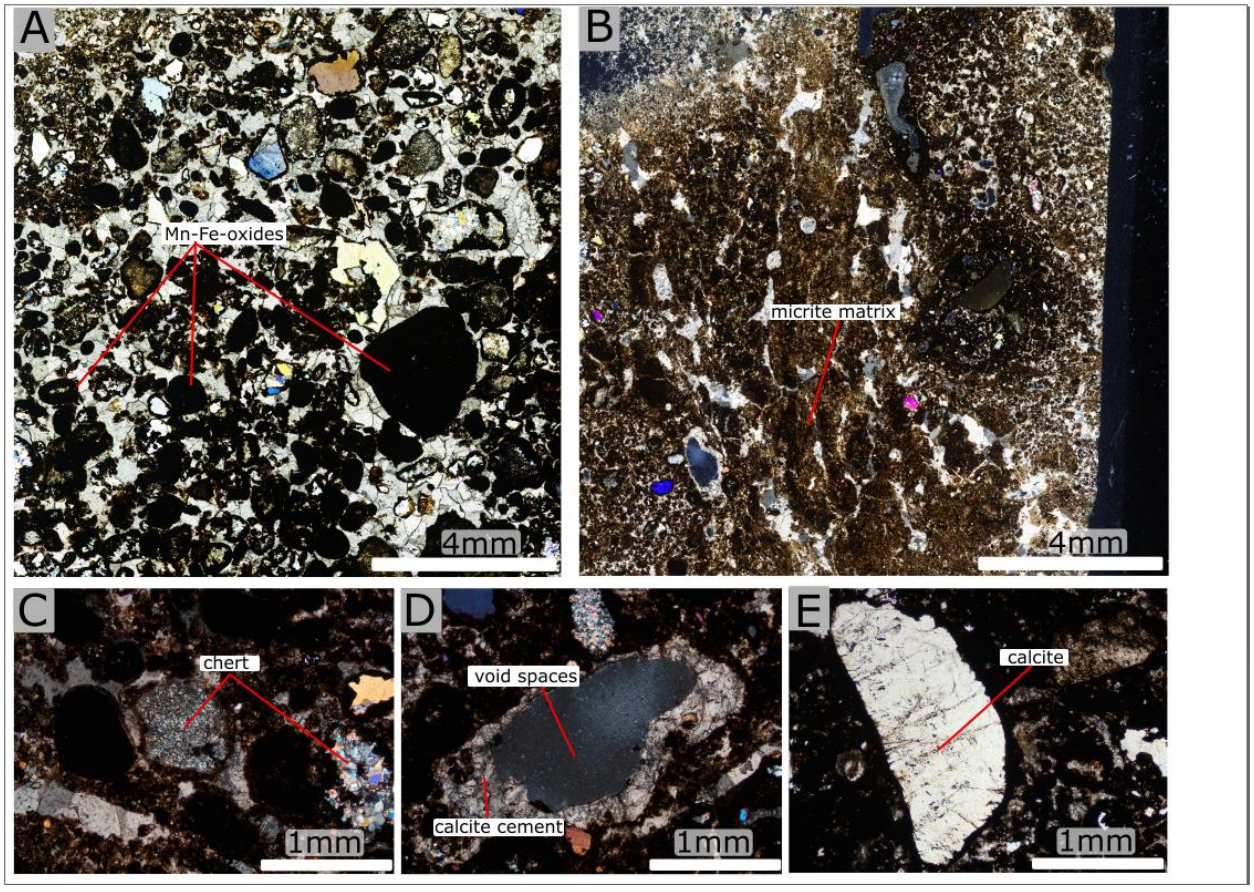


Figure 21: Micrographs of MLP13P. MLP13P is a poorly sorted calcareous sandstone. Calcite cement in this sample forms as patches and usually coats void spaces as can be from B and D.

Chert grains in this sample are small and thinly coated (C). A, B, C, and D are in XPL and E is in PPL.

4.1.14 MLP14P: Peloidal limestone with sand intercalations

This is a binary phase sample just like MLP6P. They differ because this sample has spherical peloids and the carbonate constituents make up a higher percentage of the sample than the detrital constituents. The sample is composed of a micrite matrix with long thin veins cross-cutting the sample (Fig. 22H). This part is fine-grained. The two phases are separated by a <1 mm calcite vein (Fig. 22H, 22G). The other phase of the sample is composed of a micrite matrix, calcite cement, chert grains, quartz, and Mn-Fe-oxide grains (Fig. 22A, B, C, F, I, and J). The quartz grains vary in shape, from angular to euhedral. Chert occurs as coated grains and most of the grains are rounded.

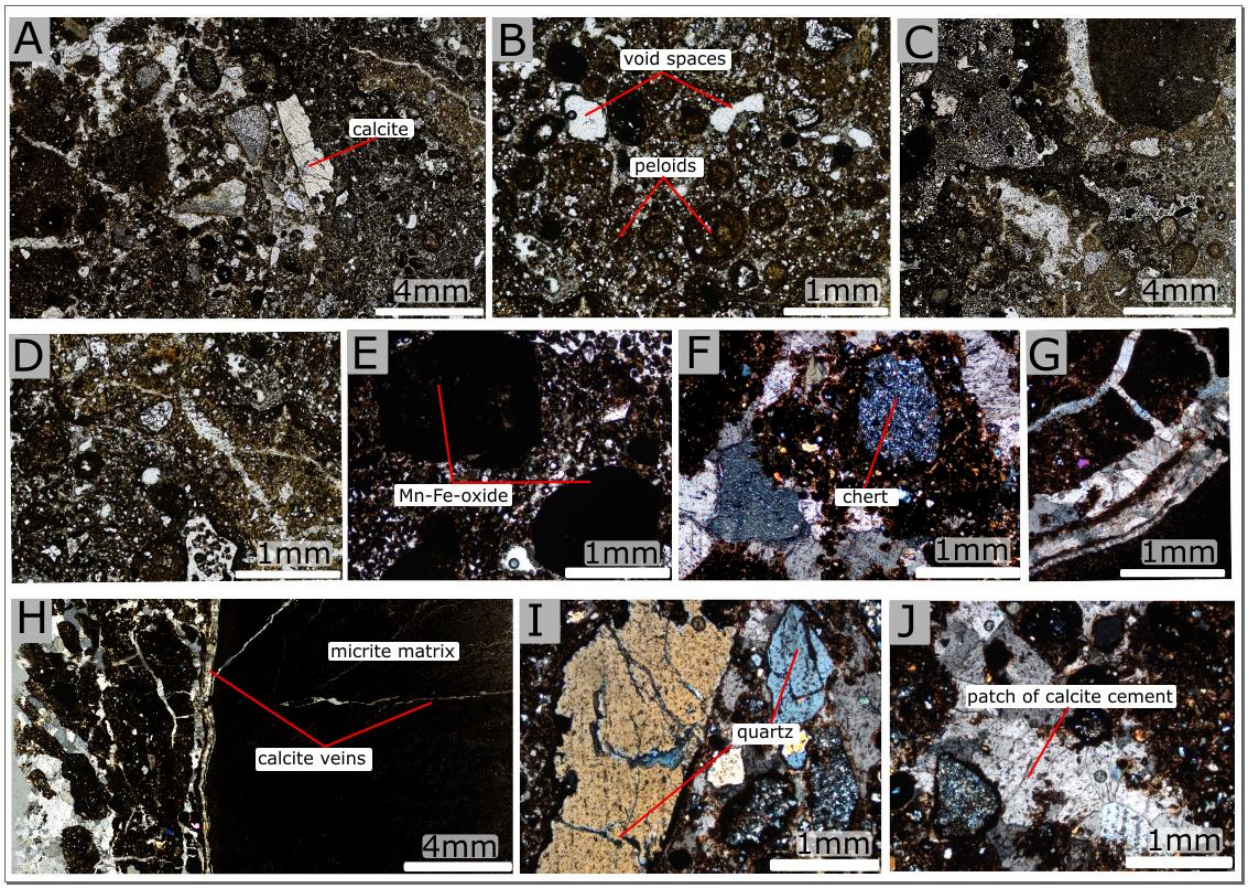


Figure 22: MLP14P image showing that MLP14P is a binary sample that has small peloids, although more abundant than MLP12P, they still do not compare to peloids encountered in MLP1P, MLP2P, and MLP3P in terms of grain size and sphericity. A, B, C, and D are in PPL, and E, F, G, H, I, and J are in XPL.

4.1.15 MLPFE1: Calcareous sandstone

According to Pickering et al. (2011b) and Dirks et al. (2010), this sample is fine-grained, well-sorted, and rounded with Fe-coated chert, quartz, and peloids as framework grains (Fig. 23). The sample is composed of Mn-Fe-oxide-coated chert. The sample is dark-colored and coarse-grained with a few peloids. It however had more Mn-Fe-oxide grains compared to peloids. The quartz grains are sub-angular to sub-rounded and 1.5 mm - 0.2 mm in size.

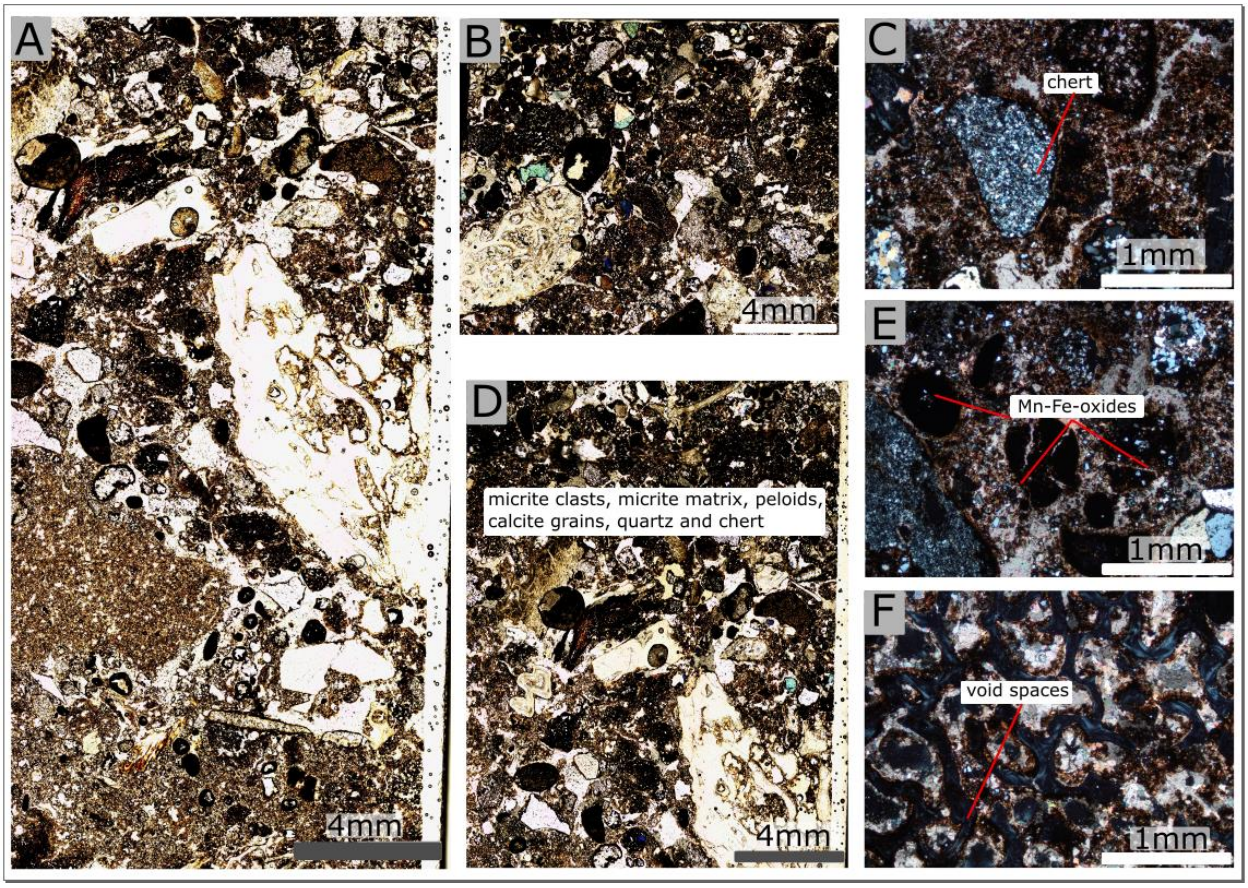


Figure 23: Composite image of MLPFE1. This figure shows the type of grains in MLPFE1. The void spaces in this sample seem to be connected (F). Compared to literature descriptions, this sample had few peloids which were so small that they were observed in a micrite clast. This sample is not well-sorted like the descriptions in the literature, it is poorly sorted.

4.1.16 MLPFF1 and MLPFF2: Alternating peloidal grainstone and sandy peloidal grainstone

This sample is a fine-grained massive rock with no sand intercalations according to Pickering et al. (2011b) and Dirks et al. (2010). Sample MLPFF1 is coarse-grained while MLPFF2 is medium grained. They are composed of micrite matrix, micrite clasts with calcite veins inside them, quartz, and chert grains (Fig. 24). MLPFF1 has no peloids. MLPFF2 has peloids from the micrite clast present but none anywhere else in the sample.

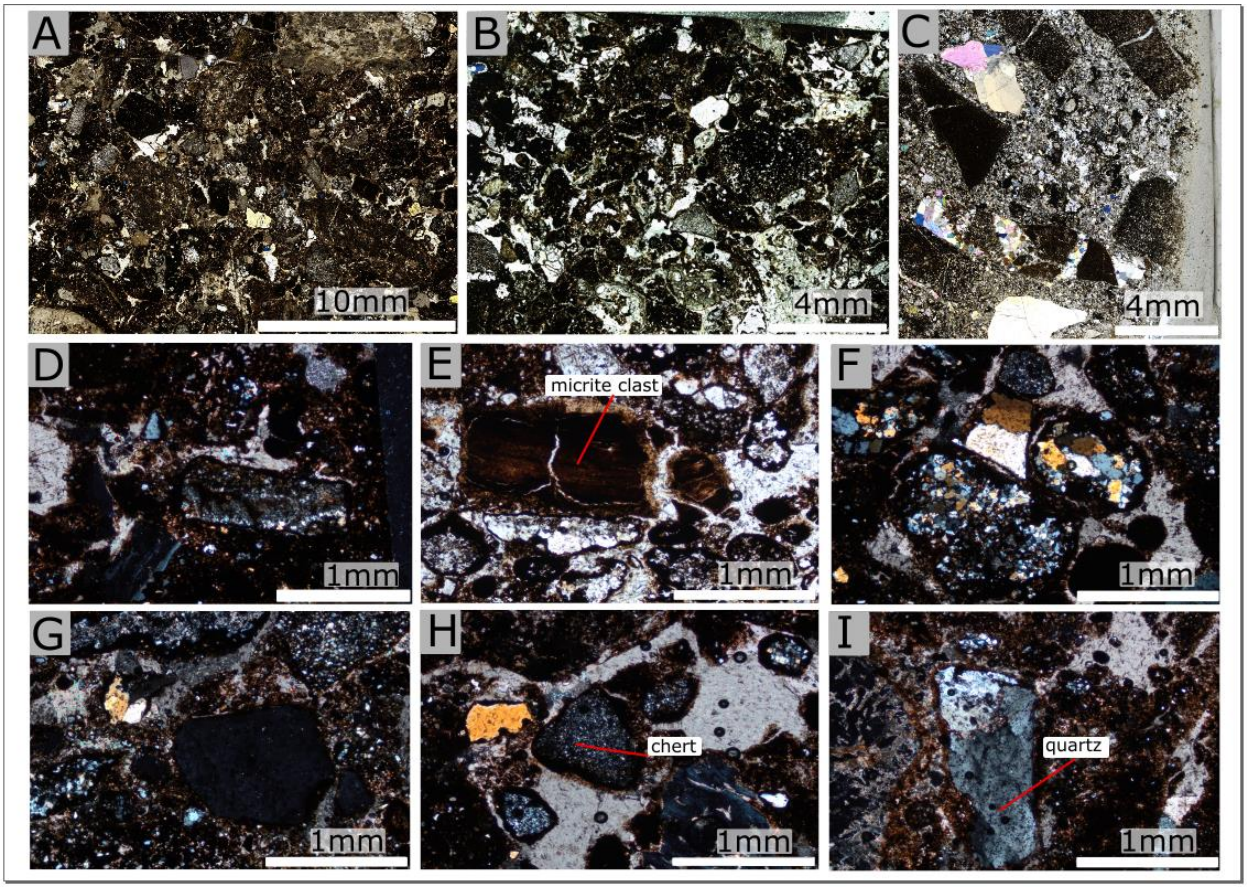


Figure 24: Composite image showing texture for MLPFF1 and MLPFF2. The two samples (MLPFF1 and MLPFF2) are not fine-grained like those studied in the literature. Chert grains were the most common clast observed with little to no peloids observed in both samples. Both samples do have a detrital element by containing quartz and chert grains.

4.1.17 MLP2F: Flowstone 2

This flowstone is composed of calcite that forms layers. The layers are white and grey coloured. The white layers are often thicker than the grey layers. The flowstone layers are older at the bottom and younger at the top. Most of the layering occurred at the bottom of the sample and this is where visible distinct closely packed layers are found. The layering becomes faint and more widely spread as we move up the sample. Calcite fabrics identified in this sample are columnar open,

columnar faint, and fascicular optic calcite (Fig. 25). The bottom of the sample has condensed dark laminae and the top has columnar open parallel laminae. The dark condensed layers are suspected to be micrite layers.

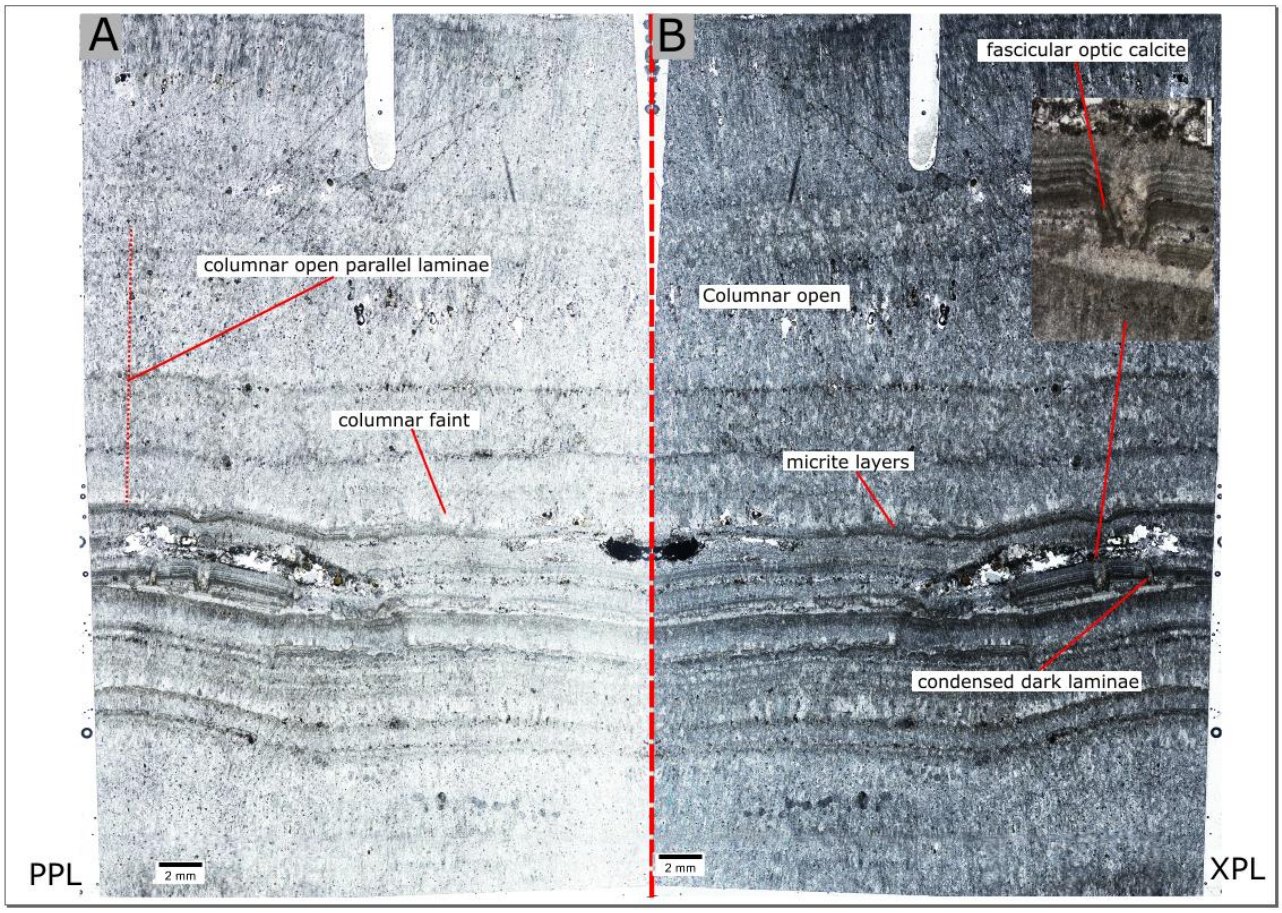


Figure 25: Image of sample MLP1F showing observed fabrics. MLP1F fabrics shown A (PPL) and B (XPL).

4.1.18 MLP3F: Flowstone 3

This sample is composed of different fabrics of calcite. It is highly fractured with vertical and sub-horizontal fractures. In terms of fabrics, this one is a columnar compact with no laminae (Fig. 26).

The white ones are the thickest while the grey ones form thin bands. At the edge of the sample, calcite forms grains with visible grain boundaries.

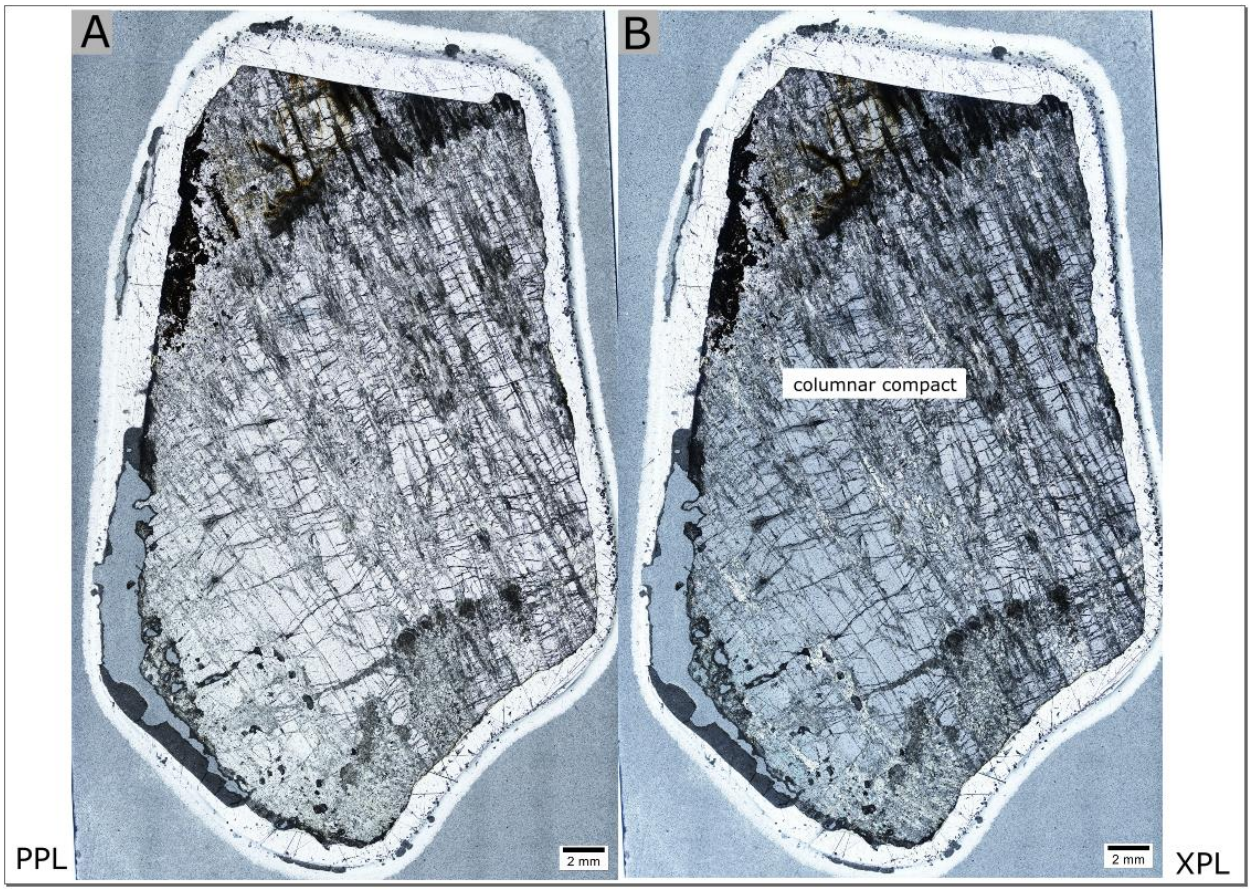


Figure 26: Image of MLP3F, it shows the flowstone as a plain flowstone with only one fabric identified, columnar open shown in A (PPL) and B (XPL)

In summary, out of all 14 samples collected from the upper member, seven contained peloids i.e., MLP1P, MLP2P, MLP3P, MLP6P, MLP9P, MLP12Pand MLP14P. Those that contained fossils include MLP2P, MLP4P, MLP5P, MLP7P, and MLP14P. MLP4P, MLP5P, MLP7P, MLP8P, MLP10P, MLP11P, and MLP13P contained no peloids at all.

4.2 SEM-EDS results

SEM-EDS analyses were done on thin sections prepared at UJ (MLP1P, MLP2P, MLP4P, MLP5P, MLP6P, MLP7P, MLP8P, MLP9P, MLP10P, MLP14P, MLPFF1, and MLPFE1). These analyses were conducted to understand the chemistry of the coated grains, especially the Mn-Fe-oxide grains. It also assisted in identifying the elementary composition of unknown grains within the sample and quantifying how much of each element was in the sample. Textures were then easy to pick up and describe, especially those that were not possible to identify using a petrographic microscope.

Mn-Fe-oxyhydroxides studies by Makhubela (2014) identified what this study ascribed as the four types of Mn-Fe-oxyhydroxide-rich coatings that occurs mostly around chert and quartz grains. It was also noted and confirmed in this study that chert and quartz are the most common nuclei in all coated grains. The Mn-Fe-oxyhydroxide coating types are classified using figure 5 and the subdivisions are as follow: type 1 (A-C), type 2 (D- F), type 3 (G- I) and type 4 (J- L). Type 1 coating represents samples that are thinly coated, and the coating is not always present around the grain boundaries. Type 2 represents the most common coating type; It has a thick concentric coating and (non-) fragmented chert/ quarts grains as a nucleus. Type 3 represents fragmented chert and quartz grains infilled with Mn-Fe-oxyhydroxides coating. Type 4 represents grains that are entirely composed of the coating. Sample MLP1P and MLP7P had no coated grains so they were used to study the micrite matrix and veins composition in detail. MLP5P, MLP9P, and MLPFE1, all have type 2, 3 & 4 coating. MLP2P (type 2 & 4), MLP4P and MLP6P (type 1 & 2), MLP10P (type 1, 2 & 3), MLP14P (type 1, 2 & 4), and MLPFF1 (type 2).

The SEM-EDS results are herein reported in three parts. One reports on all the SEM images for 11 samples showing the abundant type of coating in each sample (Fig. 27 & Fig. 28). This also

includes elementary maps of mapped clasts and Mn-Fe- oxyhydroxides coated grains (Fig. 29). Two reports on the composition of veins using EDS point and identify (ID) and elementary maps. Three reports on the composition of the matrix using SEM images and EDS elementary mapping.

1. Mn-Fe-oxyhydroxides

To study the composition of various types of coatings, samples MLP4P and MLP9P were selected. MLP4P may just have type 1 and type 2 coating but it also has the most concentrated in one zone which makes it easier to do elementary mapping on the grains. MLP9P has types 2, 3, and 4 which makes it a good sample to point and ID. The results show that the coating is predominantly manganese (average of 40% to 60%) followed by oxygen and iron in weight percentage (Fig. 30; Fig. 31A, B, C, D). The other grains in the samples are made up of silicon and oxygen as shown in Figure 30E.

2. Veins

Using the same sample i.e., MLP4P, MLP2P, and MLP6P to confirm the results obtained, the composition of the veins was confirmed to be calcite made up of calcium, carbon, and oxygen elements (Fig. 32). At proximity to the veins, grains composed of silicon, aluminum, oxygen, and carbon can be found. There are dark areas in the sample, inside the vein that remains black in color showing that there is no element present.

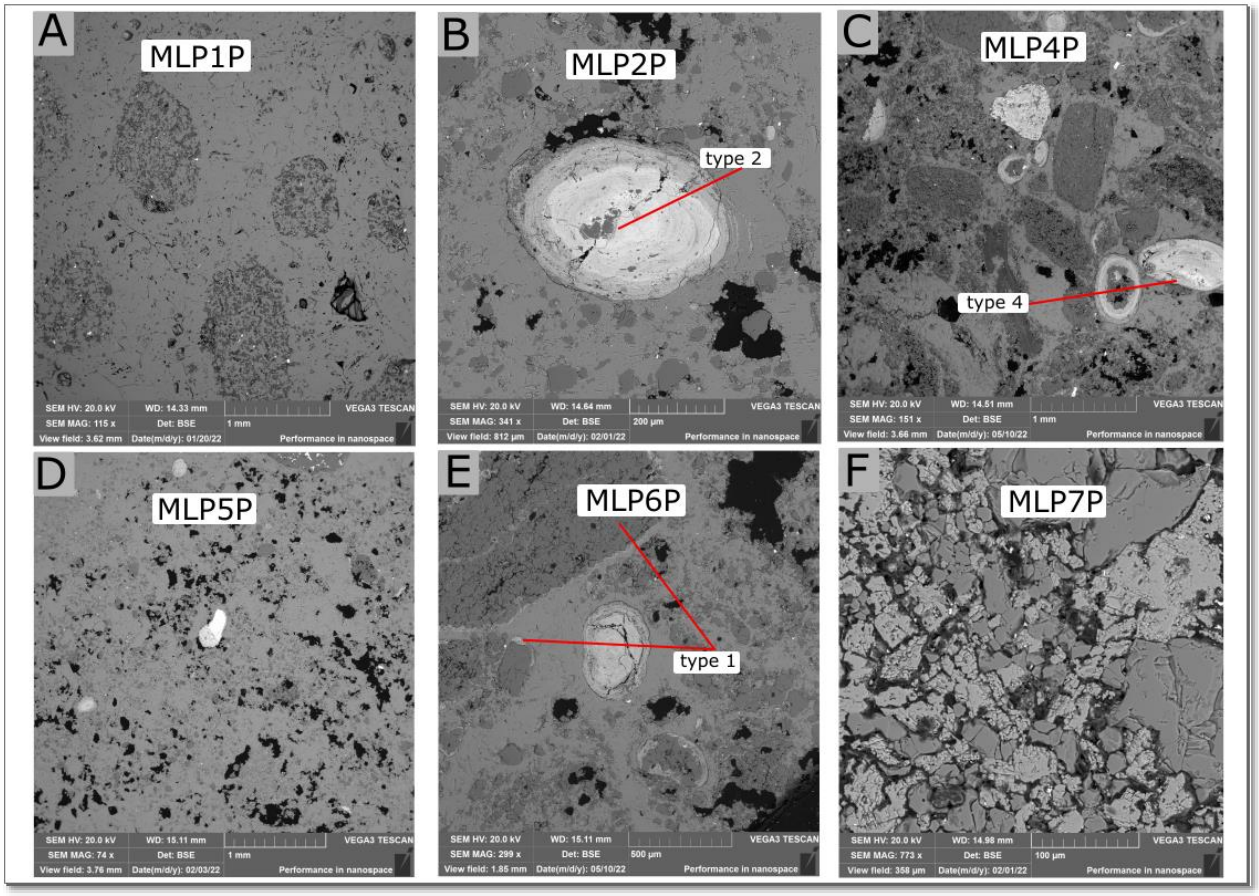


Figure 27: SEM micrographs showing per sample what type of Mn-Fe-oxyhydroxide is in each sample. Sample MLP1P (A) and MLP7P (F) have no coated grains. MLP4P (C) shows various types of coating including type 4. Type 2 coating is depicted by MLP2P (B), and type 1 can be seen from sample MLP6P (E).

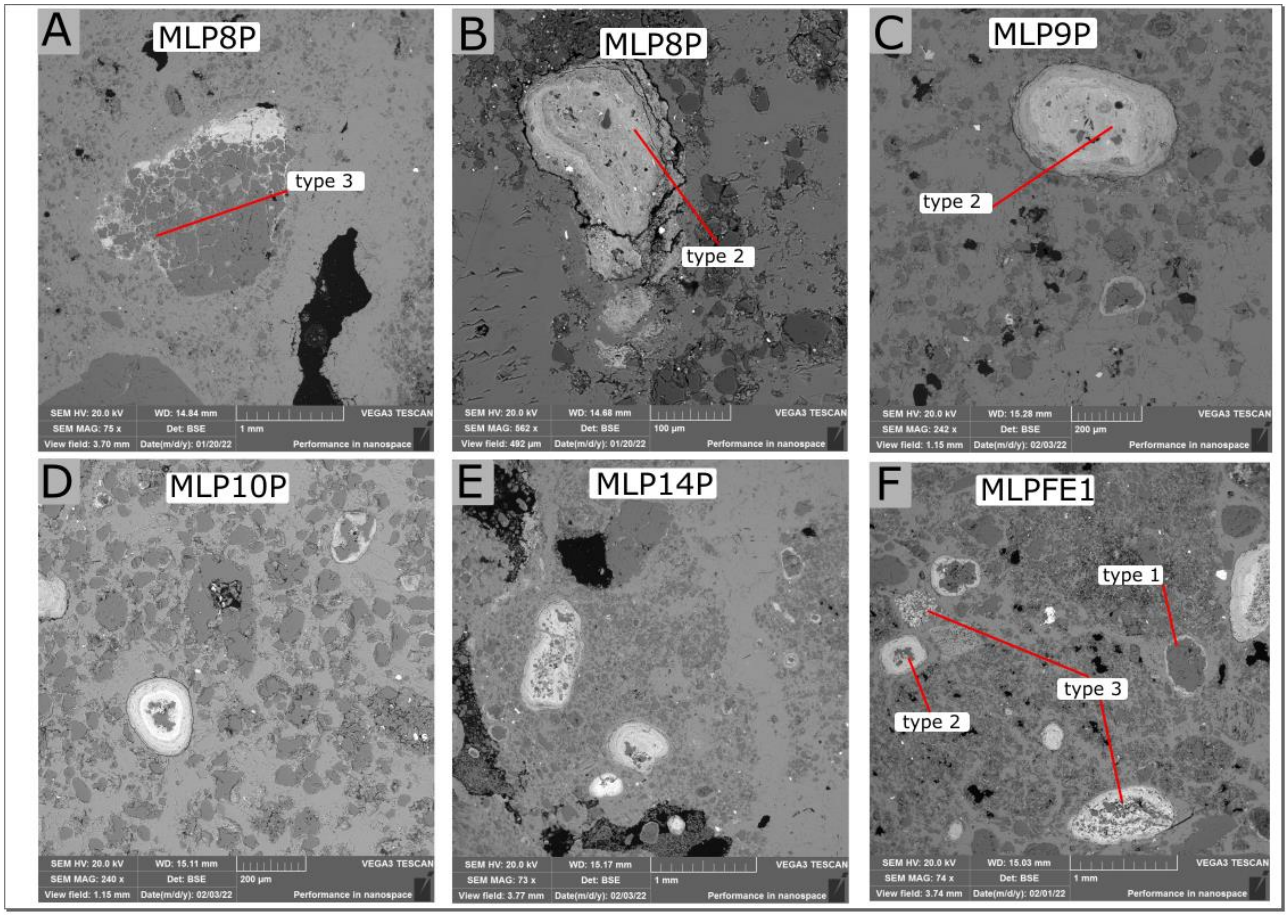


Figure 28: Continuation of figure 27 showing the rest of the samples and the types of coating that occur in each. From this figure, type 3 coating is observed in sample MLP8P (A) and MLPFE1 (F). Samples like MLP8P (A), MLP9P (C), MLP10P (D) and MLP14P (E) are dominated by type 2 coating.

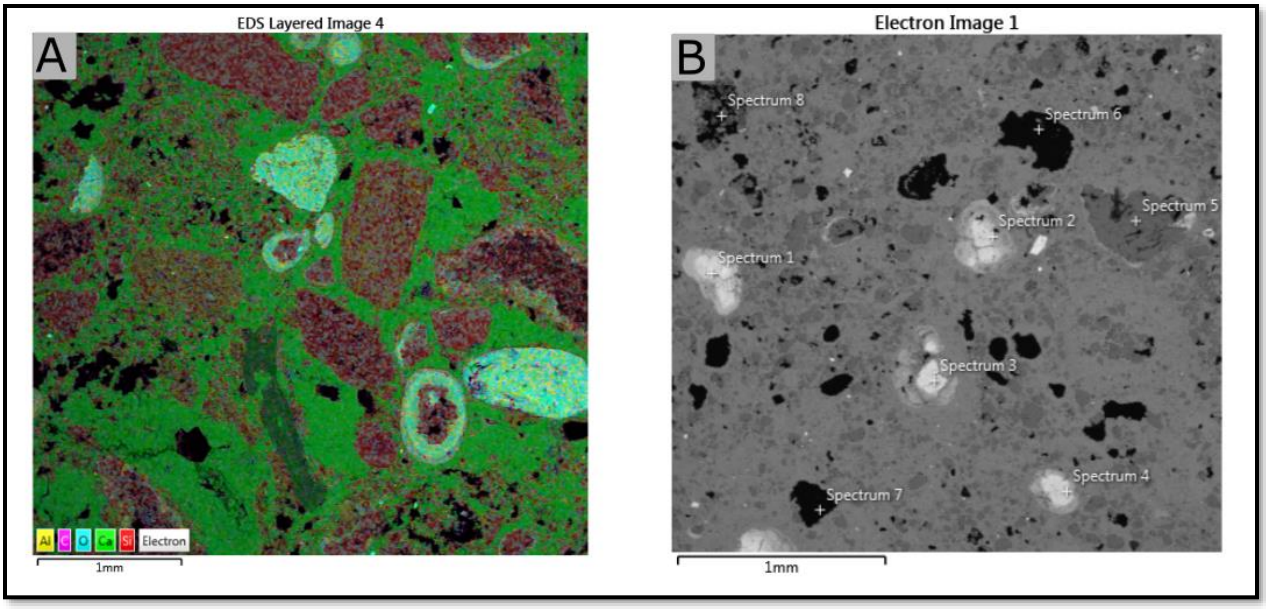


Figure 29: Composite image showing EDS elementary map composite picture (A) and point and ID image (B) of sample MLP4P and MLP9P respectively. A total of seven points were picked at different "sites" in the sample targeting different grains for the elements identified (B). The resulting spectrums are shown in Figure 31. The individual element maps that show the element that is mapped per grain to produce the composite image (A) are discussed in Figure 30.

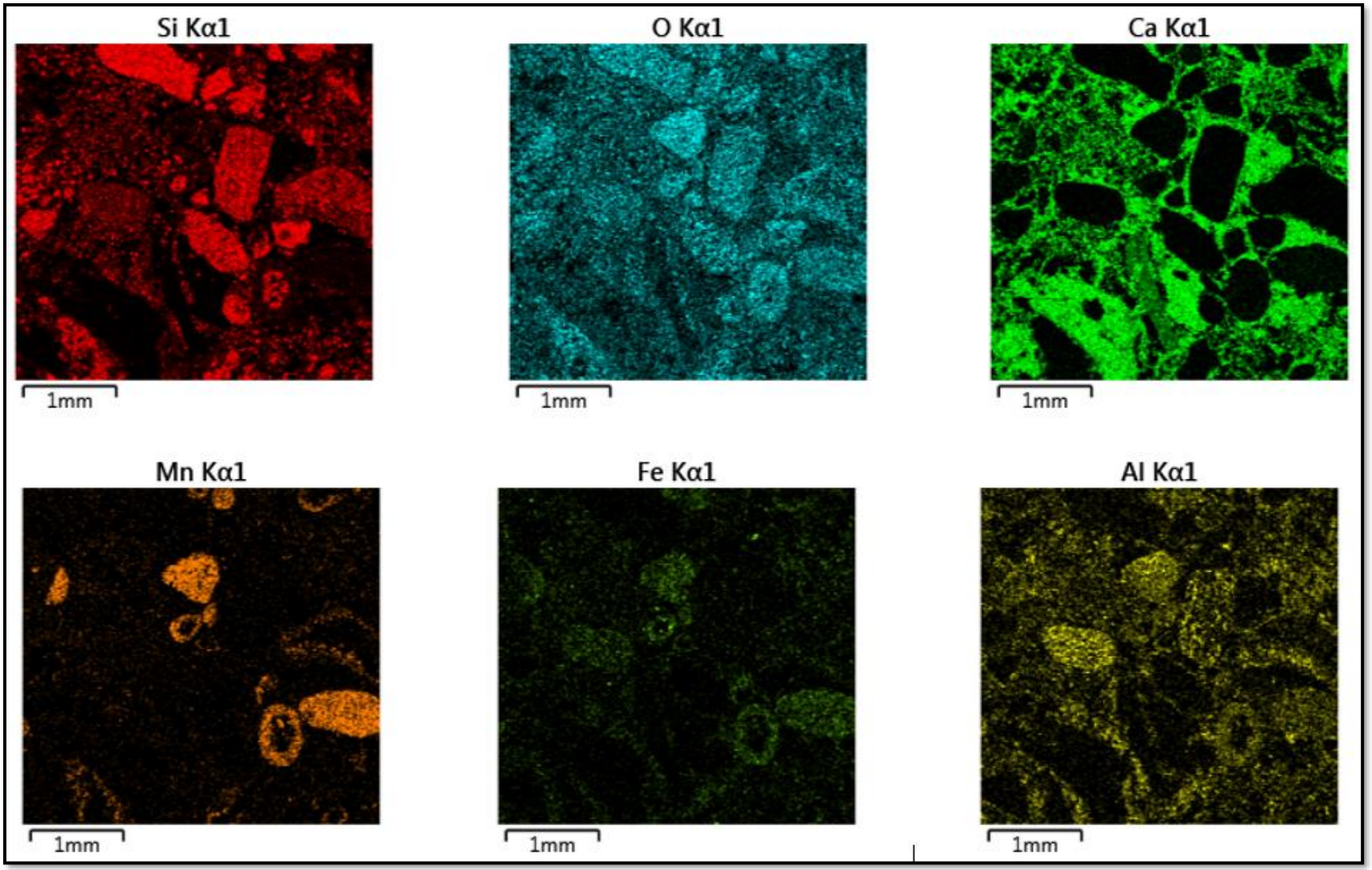

Si Kα1
1mm
O Kα1
1mm
Ca Kα1
1mm
Mn Kα1
1mm
Fe Kα1
1mm
Al Kα1
1mm

Figure 30: Individual elementary maps of MLP4P that make up the composite image of Figure 29A. The element picked up in MLP4P is aluminum (Al), oxygen (O), calcium (Ca), and silicon (Si), manganese (Mn), and iron (Fe). From these images, besides the high content of Si, Mn is more abundant than Fe which means the Mn-Fe-oxyhydroxides have a high content of manganese oxide than iron oxide.

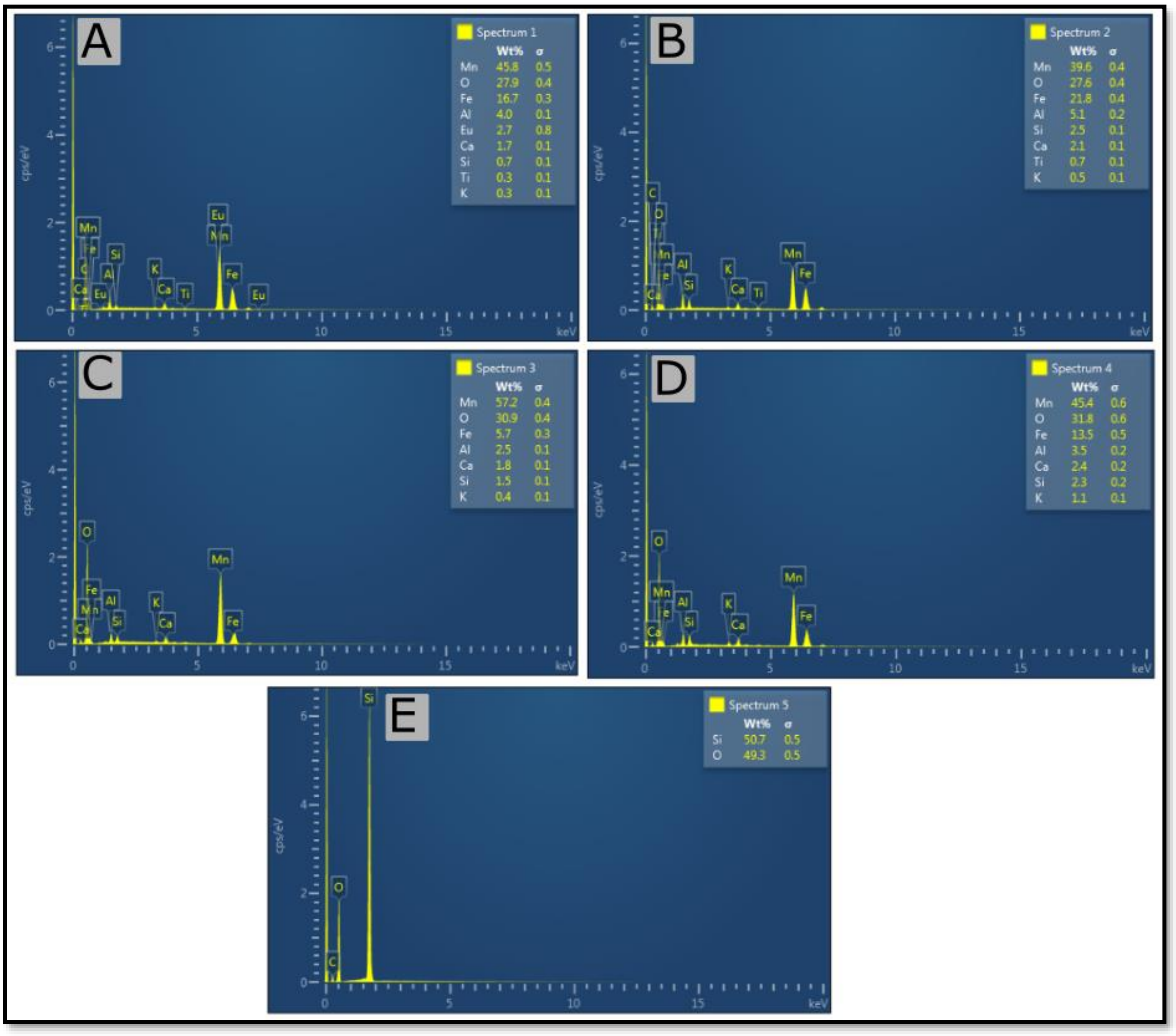


Figure 31: The point and ID spectrums (MLP9P electron image 1, see Figure 29B) show that manganese, oxygen, iron, and aluminum are the most abundant respectively. It also shows that in coated grains, Mn weighs the most with up to 60%.

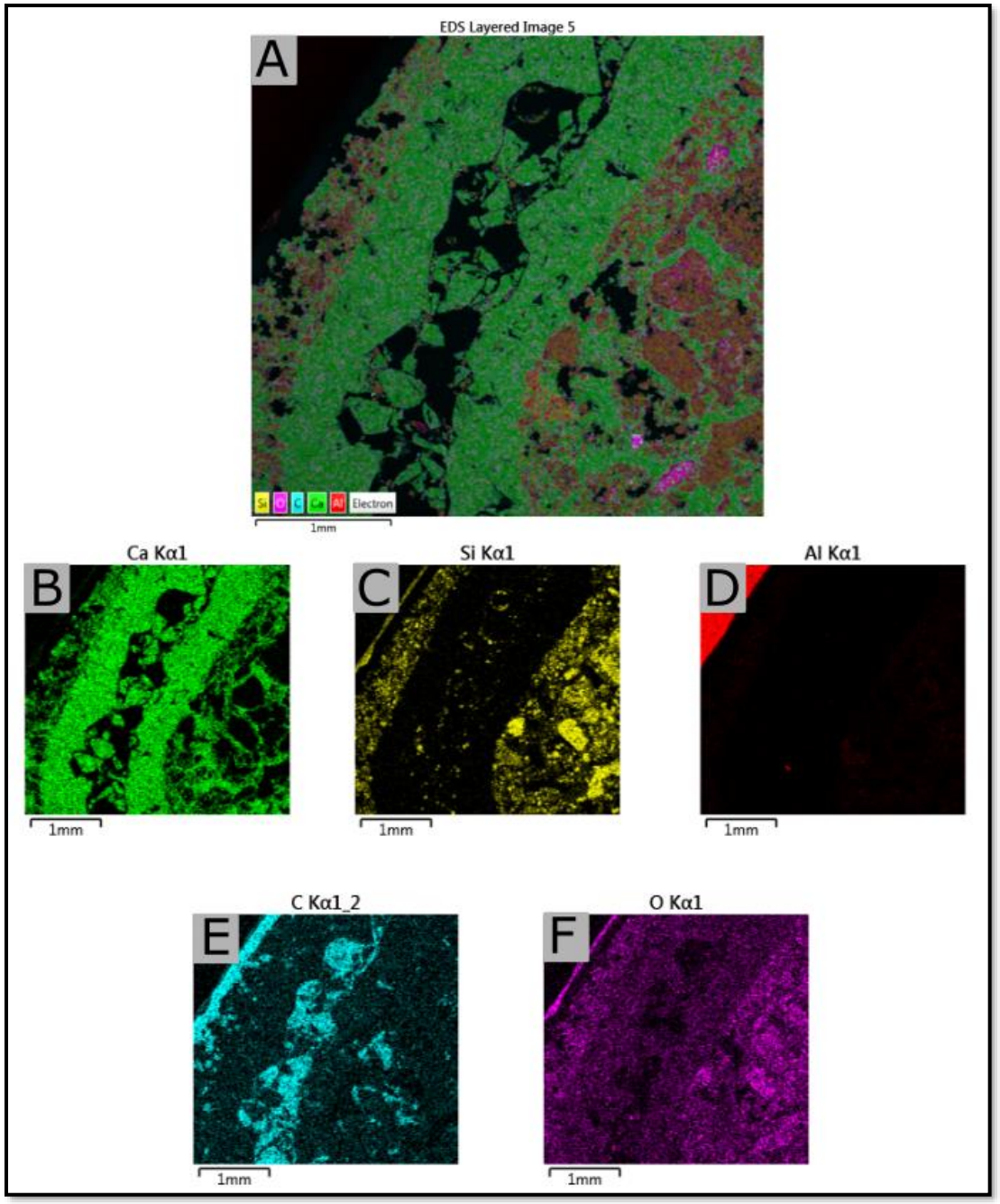


Figure 32: MLP4P matrix elementary maps (B- F) and composite image (A). This figure shows a vein and all the compositional elements of the vein. The vein is made primarily from calcium.

3. Matrix

From petrographic descriptions, the matrix is micritic. EDS elementary mapping confirmed that the matrix is composed of calcium, oxygen, oxygen and some silicon, and manganese (Fig. 33). These elements are the components that make up calcite mineral ($CaCO_3$) of which micrite is the recrystallized fine-grained version.

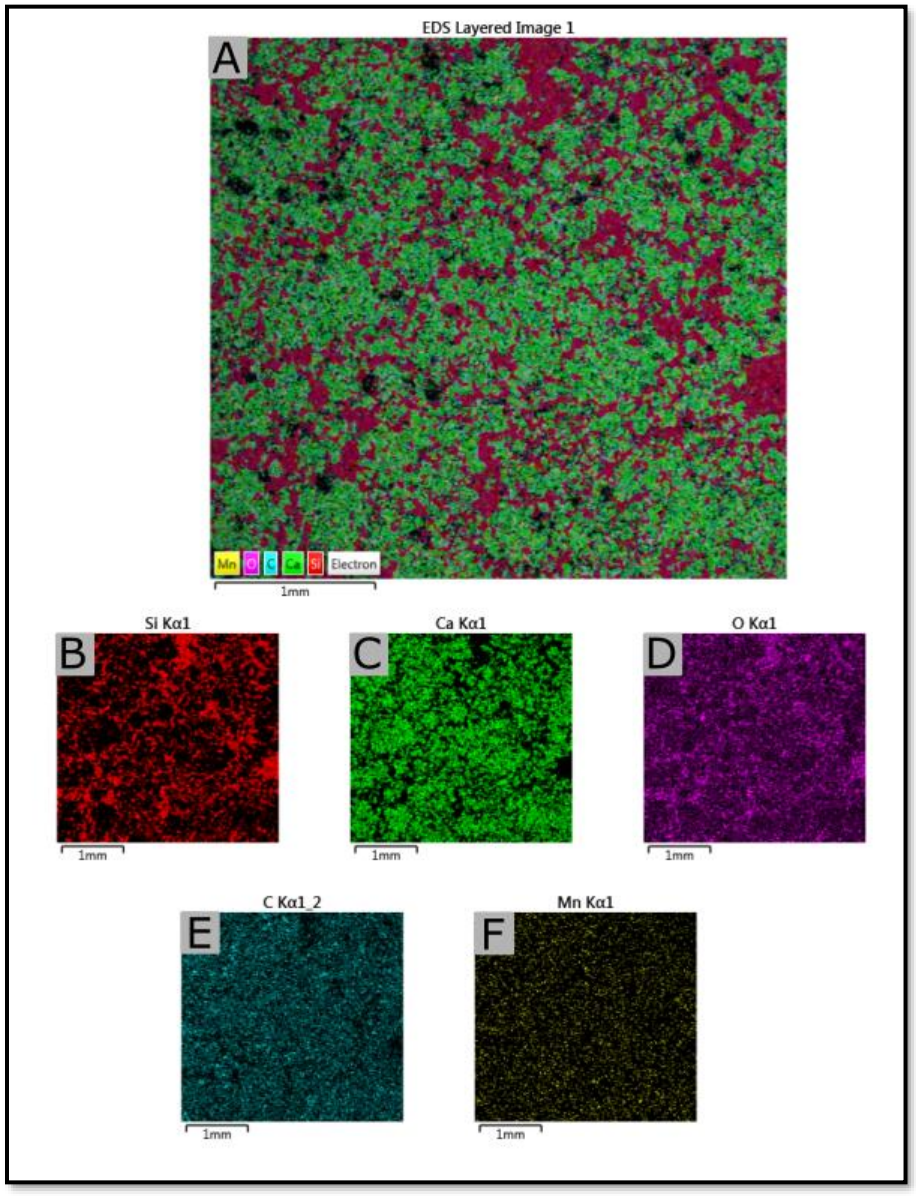


Figure 33: MLP4P micrite matrix elementary maps (B-F) results including a layered image (A).

4.3 XRF analysis results

The XRF results are reported in weight percentage (Wt% hereafter) (Table 6). The samples are predominately composed of CaO and SiO_2. Samples MLP4P- MLP14P contain more Al_2O_3, MnO, MgO, and Fe_2O_3 than samples MLP1P- MLP3P which are samples composed of peloids and calcite cement (Table 6). Sample MLP1P, MLP5P, MLP2P, MLP12P contain the most CaO Wt% which is to be expected all the samples (limestones) except for MLP5P (sandstone). From Table 6, it was observed that sample MLP1P, MLP5P and MLP12P have the least SiO_2 percentage (< 20 Wt%). This observation is contradictory to MLP5P thin section descriptions because it had more silica-based minerals as framework grains. MLP8P has the greatest percentage of SiO_2 of all samples, and this reflects the petrographic descriptions of the sample. Loss in ignition (LOI) show how much of the sample was lost before it was analyzed for elements present.

Table 6: Table presenting results in Wt% of major oxides detected by the XRF for all petrographic samples.

Sample	Al_2O_3	CaO	Fe_2O_3	K_2O	MgO	MnO	P_2O_5	SiO_2	TiO_2	LOI
1P	1.01	48.5	0.82	0.08	0.61	0.35	-	9.49	0.1	38.26
2P	2.63	38.37	2.52	0.17	0.46	1.61	-	22.29	0.22	30.61
3P	2.79	36.44	2.27	0.2	0.48	0.99	-	26.37	0.23	29.15
4P	3.98	28.57	3.32	0.25	0.56	1.38	0.1	36.06	0.28	24.57
5P	2.93	42.15	2.48	0.16	0.48	0.83	0.22	15.99	0.2	33.46
6P	3.43	35.45	2.99	0.22	0.59	1.42	0.16	24.85	0.24	29.01
7P	2.99	30.02	2.49	0.2	0.53	1.15	-	36.98	0.24	24.22
8P	1.77	26.14	2.25	0.1	0.37	1.34	-	45.68	0.13	20.88
9P	3.27	32.37	2.96	0.2	0.71	1.6	-	29.67	0.25	27.01
10P	4.01	27.61	3.97	0.24	0.58	1.72	-	38.62	0.32	22.83
11P	3.22	32.86	3.44	0.21	0.81	3.09	-	27.93	0.23	27.12
12P	1.73	38.31	2.4	0.14	6.96	2	-	10.21	0.13	37.31
13P	3.28	34.09	3.24	0.21	1.82	1.94	-	25.07	0.25	29.29
14P	3.65	29.74	3.42	0.22	0.91	1.56	0.63	33.97	0.25	24.71
FE1	3.63	30.66	3.53	0.21	0.65	2.14	1.6	31.93	0.25	24.20
FF1	2.64	28.92	3.38	0.15	0.46	1.3	1.11	38.05	0.23	22.82
FF2	4.18	34.67	3.82	0.25	0.93	1.7	0.36	24	0.28	28.78

The raw XRF data can also be used to assess the depletion and enrichment of certain elements using the shale and sandstone global standards (Table 7). The most abundant clastic sedimentary rock is a shale in terms of volume and its chemical composition has been estimated with two average compositions accepted as global standards for post-Archean shales (Ray and Paul, 2021). The two global average shale chemical composition standards are Post-Archean Australian Shale (PAAS) and North American Shale Composite (NASC). These standards are usually used to determine the upper continental crust (UCC) average composition (Ray and Paul, 2021). This study used these global standards to assess if the samples are enriched or depleted in certain elements which have an impact on the interpretation of the depositional environment. Rudnick and Gao (2014) compiled data for UCC, Taylor and McLennan (1985) for PAAS, and Pourmand et al. (2012) for NASC. Apart for the two accepted shale global standards, this study included average sedimentary rock composition presented by Clarke and Washington (1924). Clarke and Washington (1924) also presented "typical" compositions of shales, sandstones, and limestones in the earth's crust and computed average composition of shale and "typical" sedimentary composition from that data (Table 7). For sandstones, this study used two widely used standards i.e., Average Early Proterozoic Sandstone (AEPS) and Average Late Proterozoic Sandstone (ALPS) presented by Ronov and Migdisov (1971). Each study reported Al_2O_3, CaO, Fe_2O_3, K_2O, MgO, MnO, P_2O_5, SiO_2, and TiO_2 as major oxides found in shales and sandstones (Table 7). This study only focused on these major oxides as they are the same as major oxides reported in this study as well. The "typical" sandstone is more related to the AEPS which shows that average sandstone contains between ~5% and ~8% of Al_2O_3. Shales contain between 15% and 20% of Al_2O_3 which is higher than all other sedimentary rocks. Limestones contain the least Al_2O_3 of

about 1% or less. The Clarke and Washington (1924) shale composition is on par with the two chosen global standards, but the average sedimentary rock composition is higher than any individual rock averages so individual average rock averages are best to use in this case to compare with this study samples. The sandstones, shales and limestones contain little to no MnO, TiO_2, and P_2O_5. Limestones contains more MnO than all rock types with sandstones and shales containing similar MgO quantity. Other oxides in the samples vary too greatly, see Table 6 and 7.

Table 7: Table containing the major oxides reported in Wt% of the shale average three global standards i.e., UCC, NASC and PAAS. The major oxides reported coincide with the major oxides measured on the study samples. The table is modified from Ray and Paul (2021) Data source: Taylor and McLennan (1985); Pourmand et al. (2012); Rudnick and Gao (2014). AEPS and ALPS data is from Ronov and Migdisov (1971). ACSD (average composition of sedimentary rock) and CWS (Clarke and Washington shale) are just table convenience acronyms used to represent data from Clarke and Washington (1924) including shale, sandstone, and limestone average composition data.

STANDARD	Al_2O_3	CaO	Fe_2O_3	K_2O	MgO	MnO	P_2O_5	SiO_2	TiO_2
UCC	15.4	3.59	5.61	2.8	2.48	0.1	0.15	66.6	0.64
NASC	16.9	3.63	6.3	3.97	2.86	0.06	0.13	64.8	0.7
PAAS	18.9	1.3	7.24	3.7	2.2	0.11	0.16	62.8	1
AEPS	8.71	1.45	3.21	1.3	1.65	0.04	0.05	78.81	0.28
ALPS	9.79	1.37	4.9	2.94	1.67	0.09	0.07	72.78	0.56
SHALE	15.4	3.1	4.02	3.24	2.44	0	0.17	58.11	0.65
SANDSTONE	4.76	5.5	1.08	1.32	1.16	0	0.08	78.31	0.25
LIMESTONE	0.81	42.57	0.54	0.33	7.89	0.05	0.04	5.19	0.06
ACSD	13.07	5.44	3.37	2.81	2.51	0	0.15	58.53	0.056
CWS	17.02	3.44	6.71	3.58	2.7	0.5	0.19	64.21	0.72

It is evident from Table 6 and 7 that the seventeen samples used in this study are depleted in Al_2O_3, Fe_2O_3, and SiO_2 compared to the average global shale chemical composition. They are however

enriched in CaO compared to the shale global standards and those of Clarke and Washington (1924). The sandstones from this study are highly enriched in CaO and depleted in SiO_2 and generally have a slight enrichment in all oxides compared to the sandstone standards (Fig. 37, 38). The limestones are greatly depleted in all oxides except SiO_2 which is in excess. The average limestone contains more MgO and CaO of which the limestones of this study are in depletion (Fig. 39, 40). There is an exception of one sample, MLP1P which has CaO content greater than of the average limestone composition. Overall, the samples resemble more of limestones than sandstones and shales. They contain more CaO than shales and sandstones, but the CaO content is lower than the limestone average composition. The sandstones contain less SiO_2 and Al_2O_3 than the global sandstone standards and more CaO.

In the Cradle, many studies have provided XRF data for certain members/ facies that the study was interested in. For example, Edwards et al. (2021) published XRF data on deposits related to *Mrs Ples* at Sterkfontein. The following studies also reported XRF data: Makhubela et al., 2019; Wiersma et al., 2020 (Rising Star cave soil and facies respectively). Studies such as Nhauro, 2010 (Gladysvale bones) and Kuczumow et al. (2010) (*Australopithecus Africanus* bones) supplied XRF-data for bone chemical composition and not deposits. There is no standard and accepted chemical composition of various lithologies in the Cradle particularly in the Malmani Subgroup to compare with those in this study that candidate is aware of and hence the data was compared with shale, limestone and sandstone accepted standards. There are however average shale and sandstone estimates by Erikson et al., 1990 and Reczko (1994) in the Transvaal sequence (Pretoria Group) and overlies the Chuniespoort Group. The Pretoria group contains formations with mudrocks (Timeball Hill, Strubenskop, and Silverton), sandstones and conglomerates (Erikson et al., 1990). Erikson et al., (1990) results shows that the shales of the Transvaal sequence relate more to the

sedimentary shale compositions in Clarke and Washington (1924). There is a study about the black shales of the Chuniespoort Group by Meyer and Robb (1996) in which average compositions are given and Reimer (1992) provided composition averages of the carbonaceous shale from the Malmani Subgroup. These three average compositions for the Transvaal sequence were used to assess regional average shale and sandstone composition. According to Reczko (1994), the Pretoria Group shales are moderately enriched in Al_2O_3 and depleted moderately in Na_2O and MnO compared to average estimates. The Pretoria Group shales are considered CaO depleted (0.96 to 0.72 Wt%) although some are considerable enriched in CaO (2.2 Wt%). The carbonaceous shales of the Malmani Subgroup are highly aluminous, greatly depleted in CaO (0.4%) and contain 6.19 Wt% K_2O which is higher than all samples in this study. The SiO_2 and TiO_2 are also enriched while Fe_2O_3, P_2O_5 and MnO are depleted (Fig. 41, 42). The black shales of the Chuniespoort Group are similar in composition to the carbonaceous shale of the Malmani Subgroup except that they contain less Al_2O_3 and more MgO (see table 8).

Table 8: Table containing major oxides in Wt% of the carbonaceous shale from the Malmani Subgroup (CSMG), Pretoria Group shale (PSG) and the black shales of the Chuniespoort Group (BSCG) in the Cradle. The acronyms are table specific and used in Harker diagrams below in the legend. Data source: Schreiber (1990); Reimer (1992); Meyer and Robb (1996); Erikson et al. (1994).

STANDARD	Al_2O_3	CaO	Fe_2O_3	K_2O	MgO	MnO	P_2O_5	SiO_2	TiO_2
CSMG	21.47	0.4	0.96	6.19	1.57	0.03	0.03	61.14	1.14
PGS	19.07	2.71	7.68	3.58	3.1	0.05	0.16	62.37	0.64
BSCG	14.69	2.49	3.15	7.07	3.86	0.08	0.1	60.43	0.57

To further classify the petrographic samples chemically, Harker diagrams were drawn where Al_2O_3 was plotted against all other major oxides detected by the XRF (Fig. 34) and reported by the global standards (Fig. 35). The same principle was applied to SiO_2, it was plotted against all other major oxides to observe possible trends (Fig. 36). Harker diagrams were plotted to see if there is a chemical coherence between major elements which can be used to suggest that the major oxide elements have a similar underlying process (Rollinson, 1993). Harker diagram data of SiO_2 plotted against other major oxides, can be used to assess if the sediments reflect an increase in maturity (Rollinson, 1993). This means that if an increase in SiO_2 is observed (more quartz content) then there are mixing lines (sediments mixing with different ingredients) in which the rocks formed to result in different facies (Rollinson, 1993). Scattered trends seen on variation diagrams like Harker diagrams can be used to detect element mobility from compositional changes and mineralogical phases in a rock (Rollinson, 1993). These changes may be due to metamorphism or hydrothermal activity (Rollinson,1993).

Figure 34 shows Al_2O_3 of the study samples plotted against all other major oxides. The Harker diagrams were created using the grouped rock types from petrography and acronyms were given for the sake of the legend. The acronyms used are as follows: calcareous sandstones (CS), sandy limestones (SL), muddy limestone (ML), micritic limestone (ML) and peloidal limestone (PD). All samples used in this study contain Al_2O_3 content of greater than 1% to ~4.2%. The calcareous sandstones contain more Al_2O_3 and the peloidal limestone contain the least Al_2O_3 Wt%. Looking at the peloidal limestone samples (MLP1P and MLP14P), they behave very different chemically. MLP1P contains more CaO Wt% and low Al_2O_3 Wt% whereas MLP14P contains low CaO Wt% and high Al_2O_3 Wt%. MLP1P is depleted in K_2O, MgO, P_20_5, MnO, Fe_2O_3, SiO_2 and TiO_2 compared to MLP14P which is enriched in all those oxides except MgO and a slight depletion in

P_2O_5. MLP14P contains more SiO_2 than MLP1P. The muddy limestones (MLP2P and MLP3P) are chemically similar containing similar Wt% of all oxides. The micritic limestone sample MLP7P contains low CaO Wt%, MgO, P_2O_5 and a slightly high MnO and Fe_2O_3 Wt%. It is enriched in SiO_2, TiO_2 and K_2O. MLP7P seems more closely related to the muddy limestones chemically. The sandy limestone sample (MLP9P and MLP12P) also behave different chemically. MLP12P contains more MgO than all samples in this study while MLP9P contains similar MgO values like the rest of the samples. MLP12P is more enriched in CaO and MnO than MLP12P which is more enriched in K_2O, SiO_2 and Fe_2O_3. The sandstones (MLP4P, MLP5P, MLP6P, MLP8P, MLP10P, MLP11P and MLP13P) show a great chemical difference. These samples show a scattered trend mostly, but similarities can be seen in terms of Fe_2O_3 Wt%, SiO_2 Wt% and CaO Wt%. In summary, peloidal limestones contain ~1 Wt% to 3.6 Wt% of Al_2O_3, Muddy limestones contain ~2,7 Al_2O_3 Wt%, micritic limestone contains ~3 Wt% Al_2O_3, sandy limestone ~1,7 Wt% to ~3.3 Wt% Al_2O_3, and calcareous sandstones contain mostly 3 Wt% to 4 Wt%.

Results of Al_2O_3 and SiO_2 plotted against all other major oxides (Fig. 35, 36) show a depletion trend between the study samples and the shale global standards. All the petrographic samples contain less Al_2O_3, K_2O, P_2O_5, SiO_2, Fe_2O_3, TiO_2 compared to the shale global standards. The study samples seem to have similar MgO content with the shale global standards except for the sandy limestone which contains more MgO than all the samples including the shale global standards. The study samples contain more CaO and MnO than the shale global standards. This trend is not surprising as carbonate rocks like limestone identified in this study generally contain 1 % to 2.5% Al_2O_3 and sandstones contain ~1.7 % to 4.3 % Al_2O_3 whereas shale as stated in literature contains ~15 % to 20 % (Table 7). Because “normal” shales and sandstones are clastic rocks with stream sediments, they tend to have a negative correlation relation with CaO. The

sandstones at Malapa are more calcareous than “normal” sandstones. This also means they will contain less SiO_2 than the global standards. Harker diagram results of Al_2O_3 and SiO_2 plotted against all other major oxides of the sandstone global standards (Fig. 37, 38) show that the study samples are not chemically similar. Harker diagrams were drawn to compare the study samples with average compositions of sandstones, limestones and shales proposed by Clarke and Washington (1924) (Fig. 39,40). Harker diagrams were also drawn to show the relation between the Cradle standards and the study samples (Fig. 41, 42).

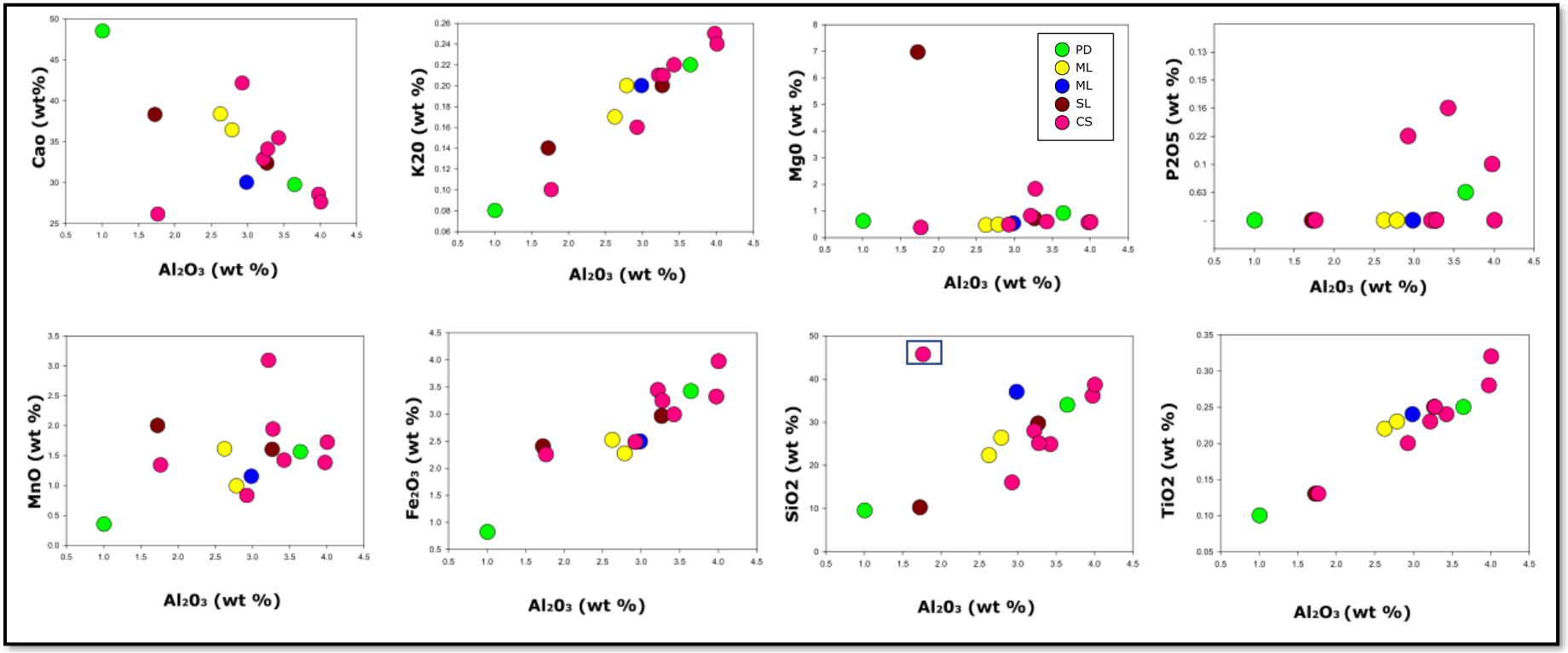


Figure 34: Harker diagrams of Al_2O_3 plotted against all other major oxides detected by the XRF and reported without global standards. These Harker diagrams exclude the global standards to assess the relationship between the samples individually. The legend is read as follows: The calcareous sandstones (CS), the sandy limestones (SL), the micritic limestones (ML), and the muddy limestones (ML) in yellow and peloidal limestone (PD). The samples grouped as calcareous sandstones using petrographic descriptions show an interesting

distribution. The calcareous sandstones seem to be closely related by having compositions that are similar and different at the same time. MLP5P (in the blue rectangle) despite being petrographically a sandstone, chemically has more CaO% than SiO_2 and low Al_2O_3.

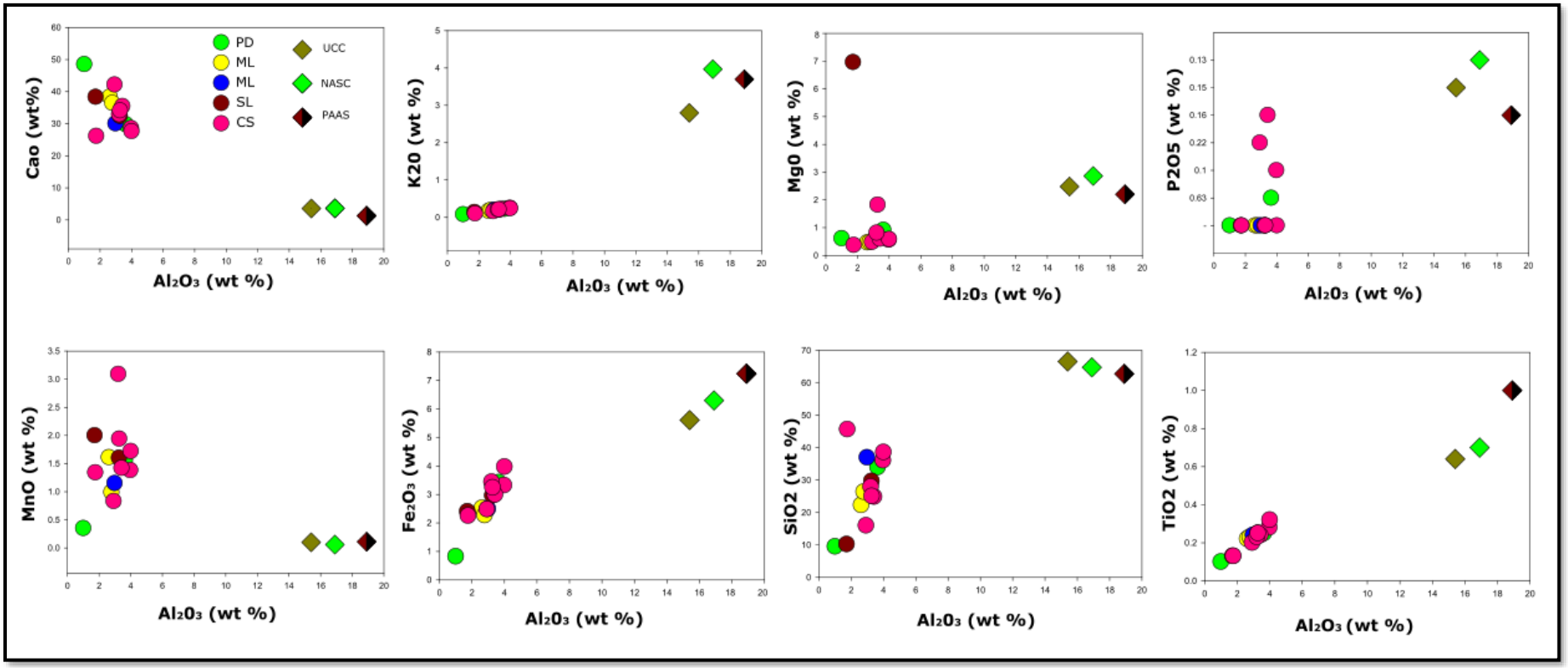


Figure 35: Harker diagrams of Al_2O_3 plotted against all other major oxides detected by the XRF and reported by global standards. All samples from this study have Al_2O_3 content of between 1- 4%. The calcareous sandstones (CS), the sandy limestones (SL), the micritic limestones (ML), and the muddy limestones (ML) in yellow and peloidal limestone (PD) all show significant depletion on all major

oxides compared to the global standards. The global standards have a low CaO/Al_2O_3 ratio, MnO/Al_2O_3 ratio, and relatively low MgO/Al_2O_3 ratio compared to this study' samples. The global standards also have a high SiO_2/Al_2O_3 ratio, K_2O/Al_2O_3 ratio, Fe_2O_3 ratio, and TiO_2 ratio.

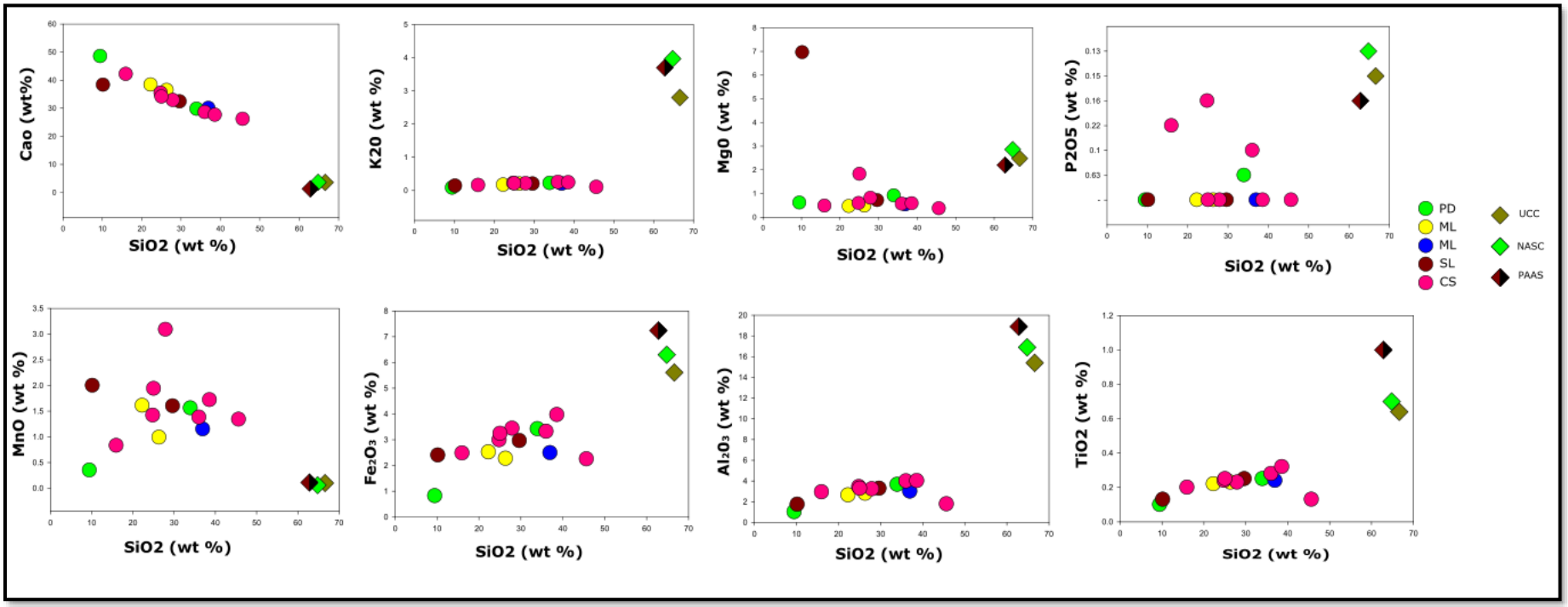


Figure 36: Harker diagrams of SiO_2 plotted against all other major oxides detected by the XRF and reported with global standards. The trend observed mostly in these Harker diagrams with SiO2 in the x-axis is a scattered trend. There isn't a strong correlation between the samples themselves and the global standards. The samples are depleted compared to global standards as can be seen from these plots as

well. Notice MLP11P having the highest MnO/ Al_2O_3 of all samples and the global standards. MLP12P also contains more MgO than the global standards and the study samples.

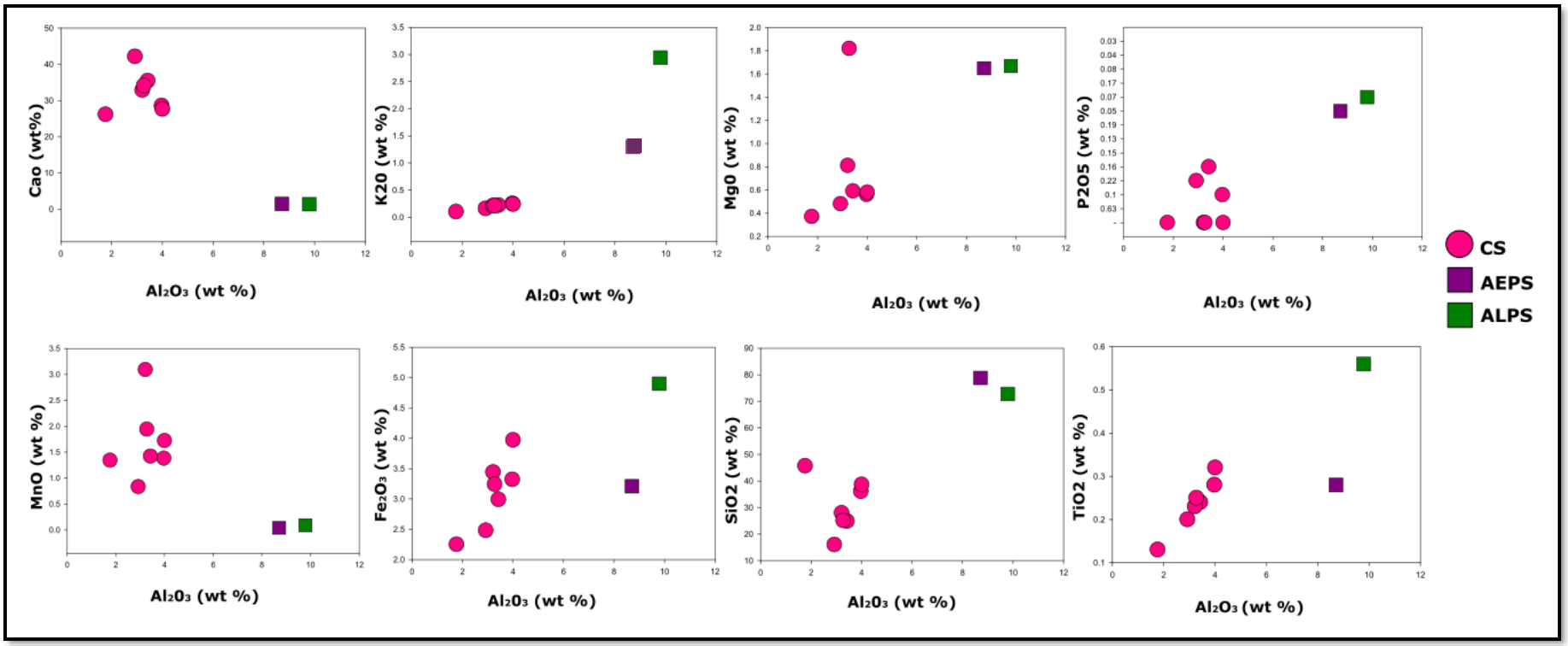


Figure 37: Harker diagrams of Al_2O_3 plotted against all other major oxides detected by the XRF reported by sandstone standards. The calcareous sandstones from this study are enriched in CaO and MnO but are depleted in Al_2O_3, SiO_2, P_2O_5, MgO and K_2O.The samples do not resemble either the Average Early Proterozoic Sandstone (AEPS) or the Average Late Proterozoic Sandstone (ALPS).

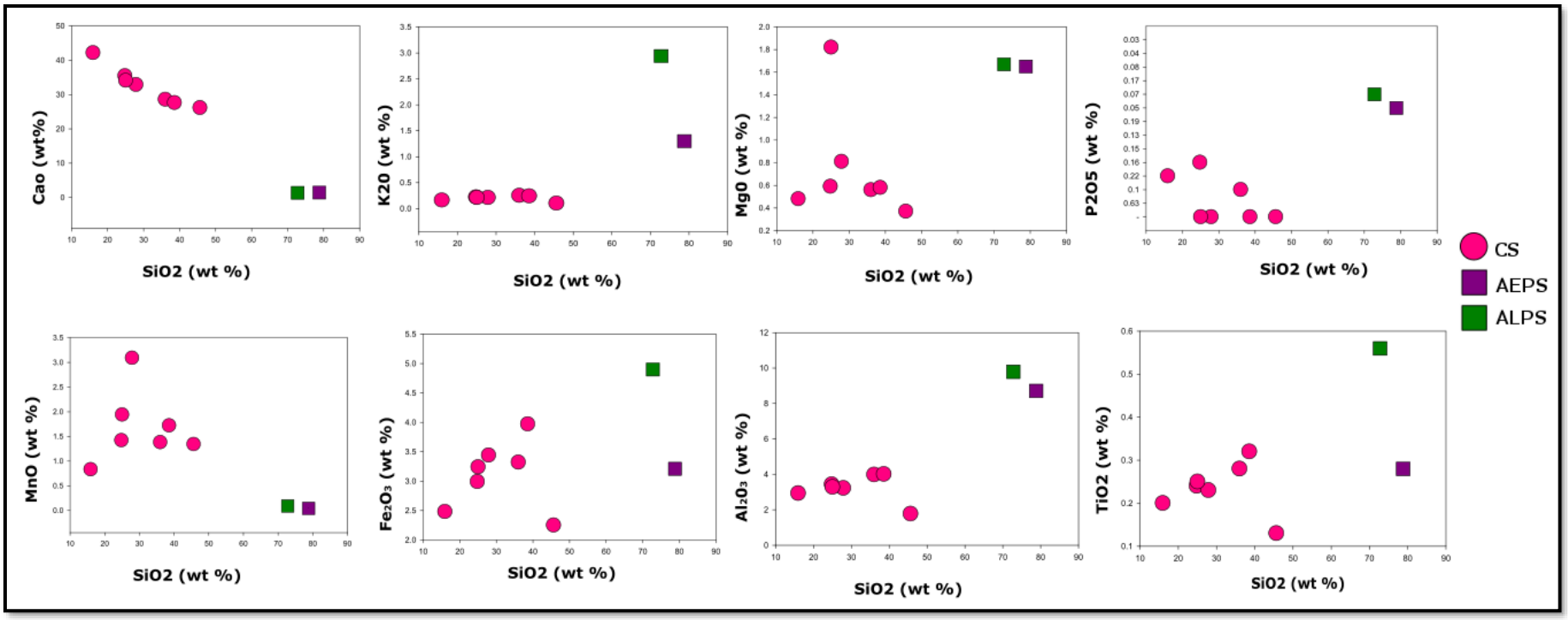


Figure 38: Harker diagrams of SiO_2 plotted against all other major oxides detected by the XRF reported by sandstone standards. The depletion trend can be seen more clearly when SiO_2 is plotted against all other oxides. Clearly the standards have more SiO_2 than all the samples, and only have one sandstone from this study containing more MgO than them.

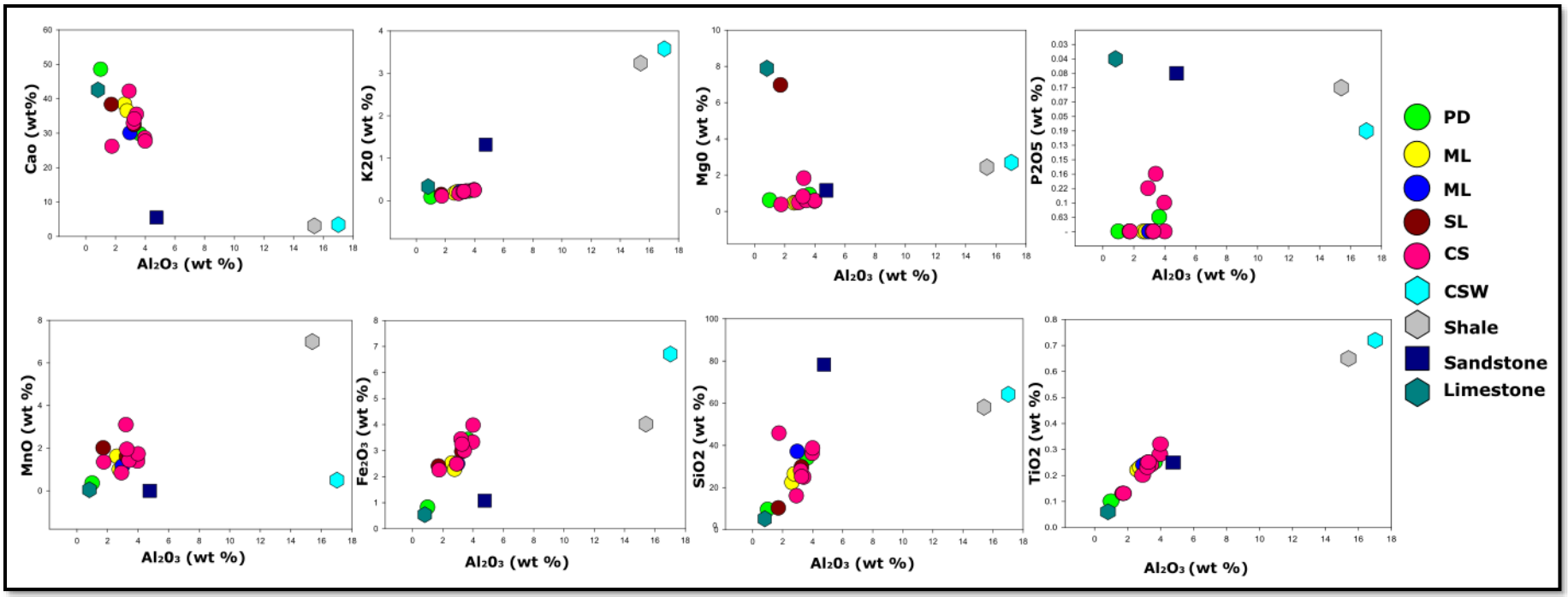


Figure 39: Harker diagrams of Al_2O_3 plotted against all other major oxides detected by the XRF reported by Clarke and Washington (1924) average composition of shale, limestone, and sandstone standards. The diagram also reports on the average shale calculated from this data presented a s a standard by Clarke and Washington (1924). This figure shows that the study samples are more similar to limestone in terms of most oxides than the sandstone and the two shales. In terms of TiO_2 and MgO, MnO and Fe_2O_3, the samples are more chemically similar to both sandstones and limestones. A sample that is more similar compositionally to the limestones average of Clarke and Washington (1924) is MLP1P, in all major oxides except for the MgO and P_2O_5 they are siting almost on top of each other in the diagram.

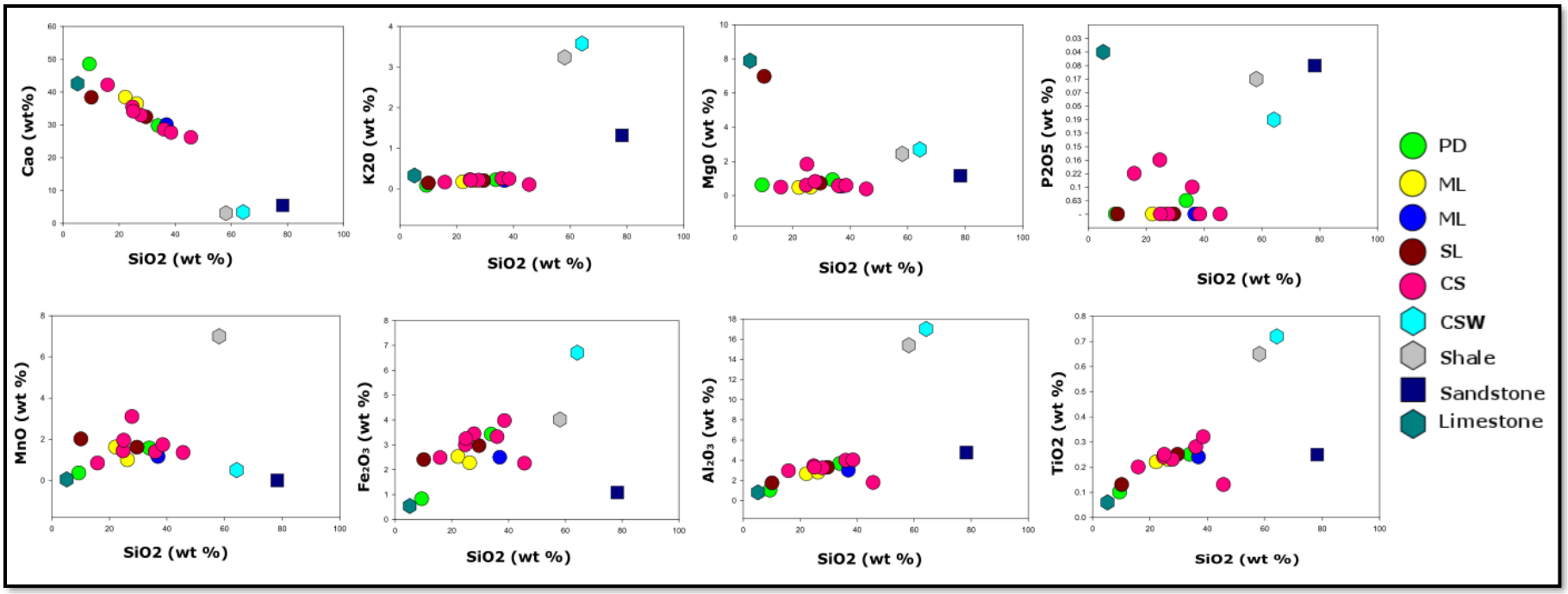


Figure 40: Harker diagrams of SiO_2 plotted against all other major oxides detected by the XRF reported by Clarke and Washington (1924) average composition of shale, limestone, and sandstone standards. The study samples are depleted in SiO2 and slightly depleted in all other oxides except for CaO of which they are enriched compared to the four averages. The depletion trend is seen in both presentation of the data.

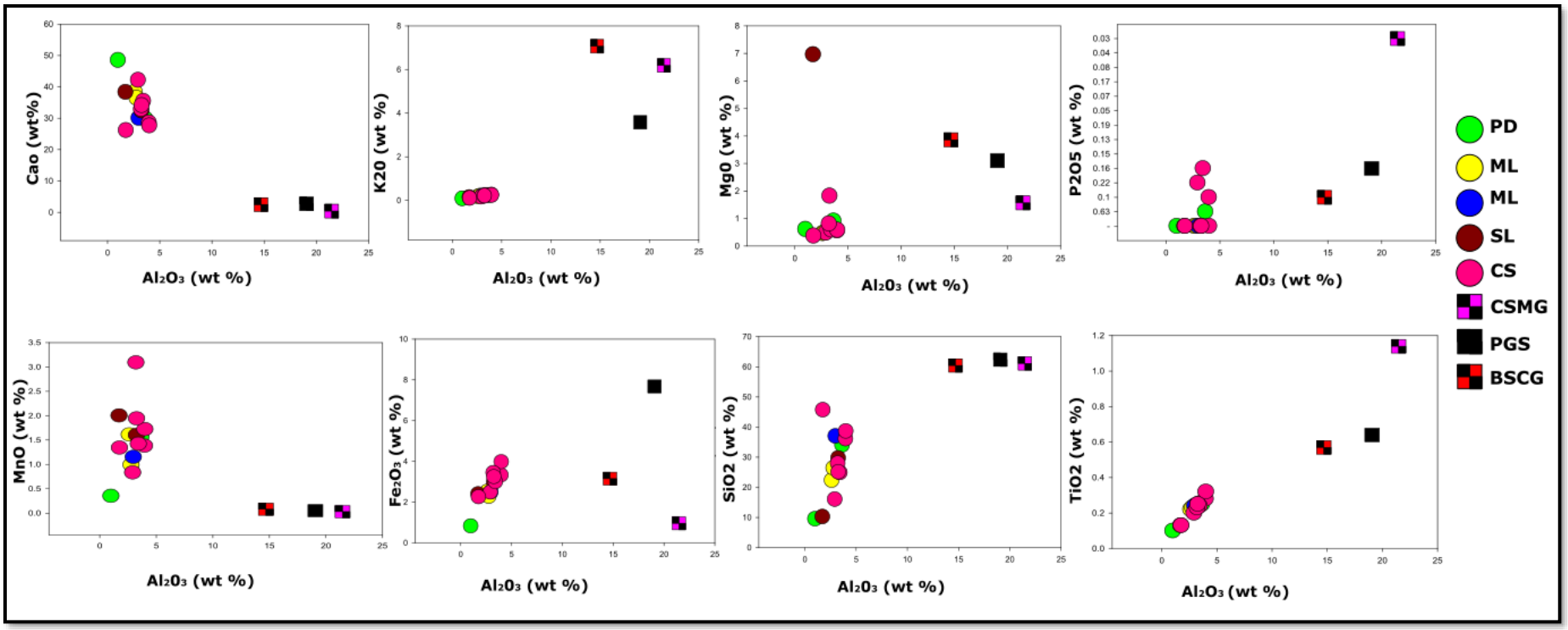


Figure 41: Harker diagrams of Al_2O_3 plotted against all other major oxides detected by the XRF reported by average compositions of shale in the Cradle. Despite the standard data coming from the regional area, the samples are not chemically correlated with the standards. The study samples are depleted in Al2O3 compared to the Cradle averages. The averages show a depletion in CaO, MnO and a slight depletion in Fe_2O_3 compared to the study samples. The calcareous shales of the Malmani Subgroup (CSMG) are the most chemically different in all the data represented in this Harker diagram.

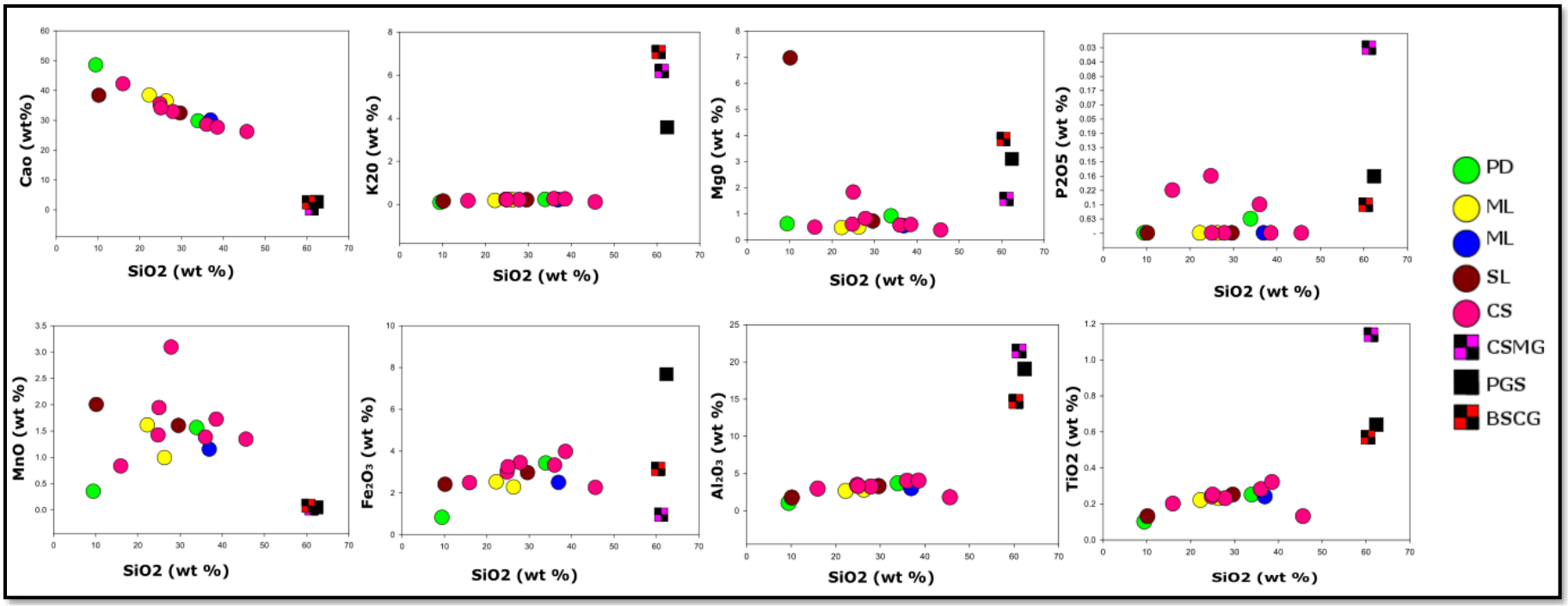


Figure 42: Harker diagrams of SiO_2 plotted against all other major oxides detected by the XRF reported by average compositions of shale in the Cradle. The trends are better seen when SiO_2 is the controlling factor. The three averages contain similar amounts of CaO and MnO Wt%, that is why they are sitting on top of each other.

CHAPTER 5: GEOCHRONOLOGY RESULTS

5.1 Flowstone 2F

Flowstone 2F and 3F were dated at the university of the Witwatersrand using the LA-ICP-MS isochron method. Flowstone 2F was sampled from pit 2, in the same deposit area Pickering et al. (2011a) sampled for Flowstone 2. In this study, two lithologies were identified within the area where the flowstone is draping over sediments i.e., peloidal limestone and muddy limestone. Pickering et al. (2011a) placed the flowstone as draping over block 3 in pit 2 and covered by Facies F. After site visitation to reassess the stratigraphy and understand the stratigraphic context of Flowstone 2F, this study noted that block 3 couldn't be identified in the field. The flowstone rather drapes over the peloidal limestone, muddy limestone and the calcareous sandstone in the vicinity. Flowstone 1F was dated to 3.72 Ma ± 0.77. The error of the age is approximately 21% (Fig. 43) with a mean squared weighted deviation (MSWD) of 2.8. The MSWD is greater than 1, which means the ages are over dispersed with respect to the stated analytical uncertainties and other factors. The $P(x^2)$ values are also less than 0.05 which also indicates the ages are over dispersed. The analytical uncertainty is ~21% at 95% confidence level.

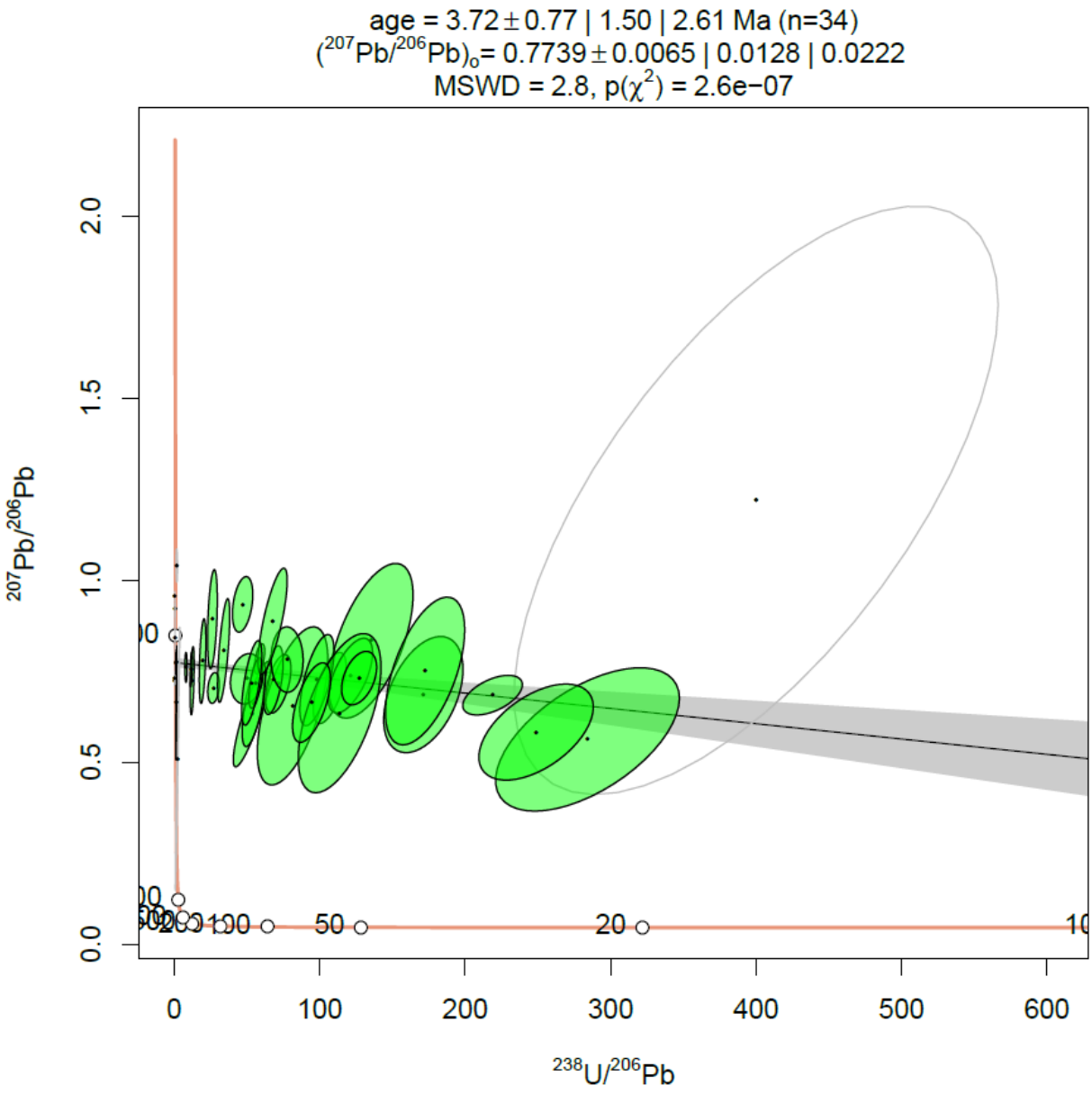


Figure 43: Image depicting the date of MLP1F which was determined using LA-ICP-MS via the isochron method. The age is 3.72 Ma with an error of ± 0.77. The MSWD is higher than 1 which means this age is overdispersed concerning the stated analytical uncertainties

5.2 Flowstone 3F

Flowstone 3F was sampled from the newly deposits right next to the main pit. This flowstone occurred as an ex-situ clast incorporated within facies C deposits (Fig. 7C). This flowstone fragment yielded an age of 7.50 Ma ± 0.37 (Fig. 44). The error of the age is ~5% with a MSWD of 2.1 and $P(x^2)$ of 0.00026. The MSWD is greater than 1 so the data points defining the isochron are caused by more than analytical uncertainty, the age is over dispersed with respect to stated analytical uncertainties and more factors. The $P(x^2)$ is less than 0.05 which mean the age was over dispersed and analytical uncertainties are underestimated by a factor of a root of MSWD. The analytical uncertainty is ~5% at 95% confidence level. The error within the age of Flowstone 3F is less than that of Flowstone 2F.

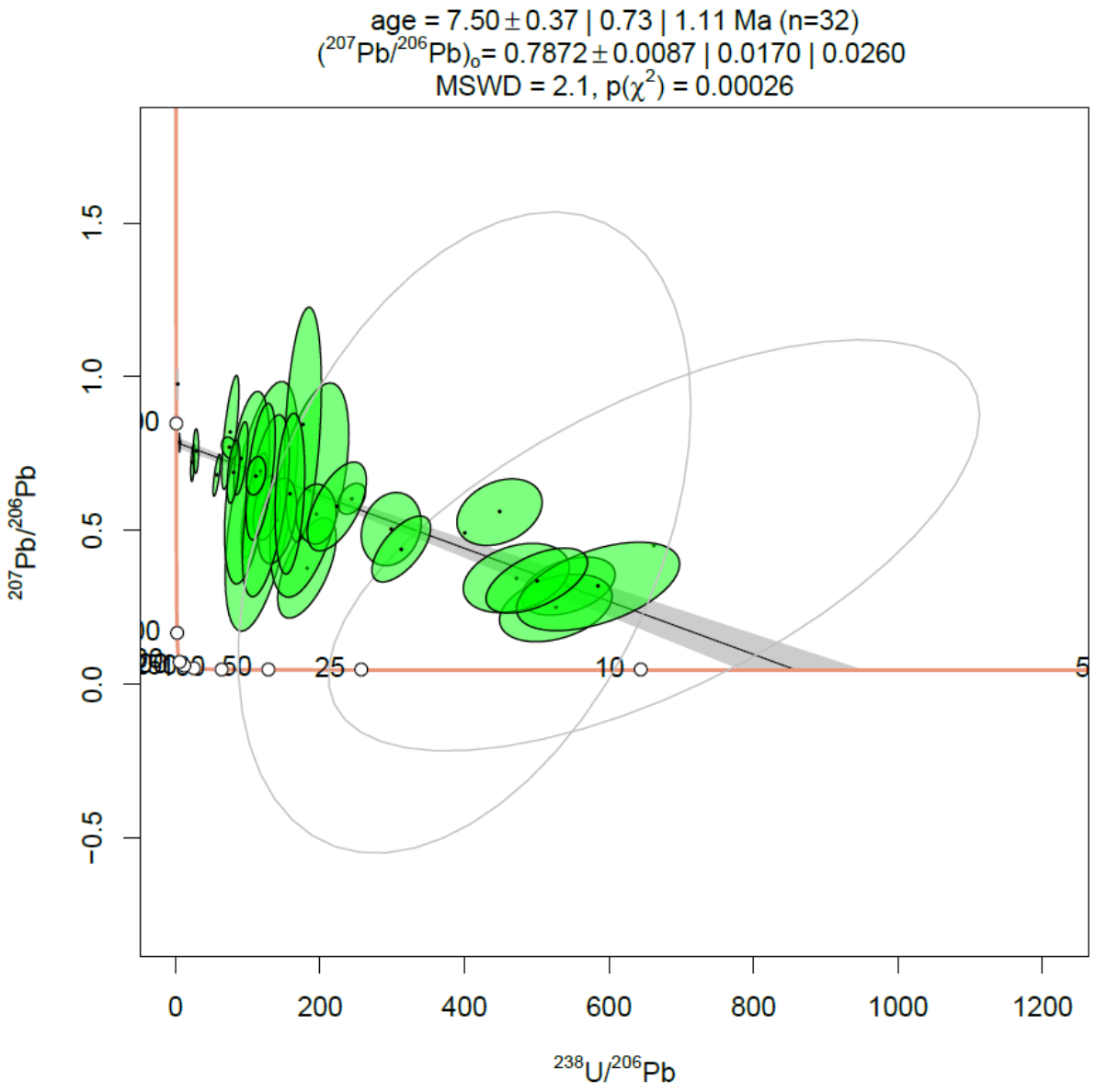


Figure 44: Image showing the date of MLP2F which was determined using LA-ICP-MS via the isochron method. The age is 7.50 Ma with an error of ± 0.37. The MSWD is also greater than 1, this indicates that the ages are also overdispersed concerning the stated analytical uncertainties.

5.3 Cosmogenic nuclide burial dating results

Individual calculated ages for all six samples are reported in table 9. Table 10 contains sample processing data and measured results. MLP1CN- MLP4CN and MLP6CN were sampled as muddy sandstones and MLP5CN was a quartz vein. MLP1CN - MLP4CN were sampled in pit 2 deposits and MLP5CN - MLP6CN were sampled in the newly exposed deposits (Fig. 6). The ^{10}Be and ^{26}Al concentrations and ages were calculated at 1σ meaning the results include 68% of all samples. The samples were sampled in more or less the same depth in the upper member, so the stratigraphic context is intact.

Sample MLP4CN contains the lowest concentrations of ^{10}Be and ^{26}Al of all samples, this sample is the same as MLP8P which contained the largest chert and quartz grains. This means that MLP4CN was exposed at the cave surface for a very short time prior to being incorporated in the cave sediments. As expected of a sample composed almost entirely of quartz grains i.e., quartz vein, sample MLP5CN contains the highest concentrations of ^{10}Be and ^{26}Al meaning that it was exposed for longer at the cave surface than the rest of the samples before burial. MLP1CN and MLP2CN have similar high concentrations of ^{10}Be and ^{26}Al a while MLP3CN and MLP6CN have similar low concentrations. All individual ages are similar and range between 1.55 and 1.98 Ma. These samples were then used to create an isochron cosmogenic burial age using the isochron cosmogenic nuclide burial dating method and the resultant isochron is shown in Figure 45. The isochron cosmogenic burial age was calculated to assign one age to the deposits in pit 2 and the newly exposed deposits of Malapa. The isochron age is 1.59 ± 0.44 Ma.

Table 9 : Table containing cosmogenic burial dating result for the six samples. N10 represents cosmogenic concentrations of ^{10}Be and N26 represents concentrations of ^{26}Al.

Sample ID	N10 ($\times10^6$ at/g)	$\pm$ 1σ ($\times10^4$ at/g)	N26 ($\times10^6$ at/g)	$\pm$ 1σ ($\times10^5$ at/g)	Al/Be	$\pm$ 1σ	Burial Age (Ma)	$\pm$ 1σ (Ma)
MLP1CN	1.40	9.42	3.83	1.79	2.74	0.22	1.88	0.15
MLP2CN	1.14	7.34	4.22	1.82	3.71	0.29	1.39	0.11
MLP3CN	0.94	4.67	3.12	1.30	3.32	0.22	1.55	0.1
MLP4CN	0.68	2.29	1.77	0.72	2.6	0.14	1.98	0.1
MLP5CN	1.55	5.15	5.10	1.70	3.28	0.15	1.57	0.07
MLP6CN	1.19E	4.00	3.90	1.32	3.27	0.16	1.57	0.07

Table 10: Table containing the cosmogenic nuclide data measured from the six samples.

Sample ID	Quartz wt. (g)	Be (ug)	[Al] (µg/g)	10Be/9Be ($\times10^{-13}$)	$\pm$ 1σ ($\times10^{-14}$)	26Al/27Al ($\times10^{-13}$)	$\pm$ 1σ ($\times10^{-14}$)
MLP1CN	2.09	310.85	537.10	3.05	82.0	3.68	1.67
MLP2CN	2.47	307.90	318.81	3.02	73.8	4.26	1.80
MLP3CN	4.40	312.58	277.59	3.60	86.1	4.15	1.71
MLP4CN	13.46	310.98	394.57	6.06	1.41	3.99	1.61
MLP5CN	5.53	312.24	219.61	5.75	1.28	8.22	2.72
MLP6CN	6.75	312.19	217.88	5.50	1.20	7.40	2.49

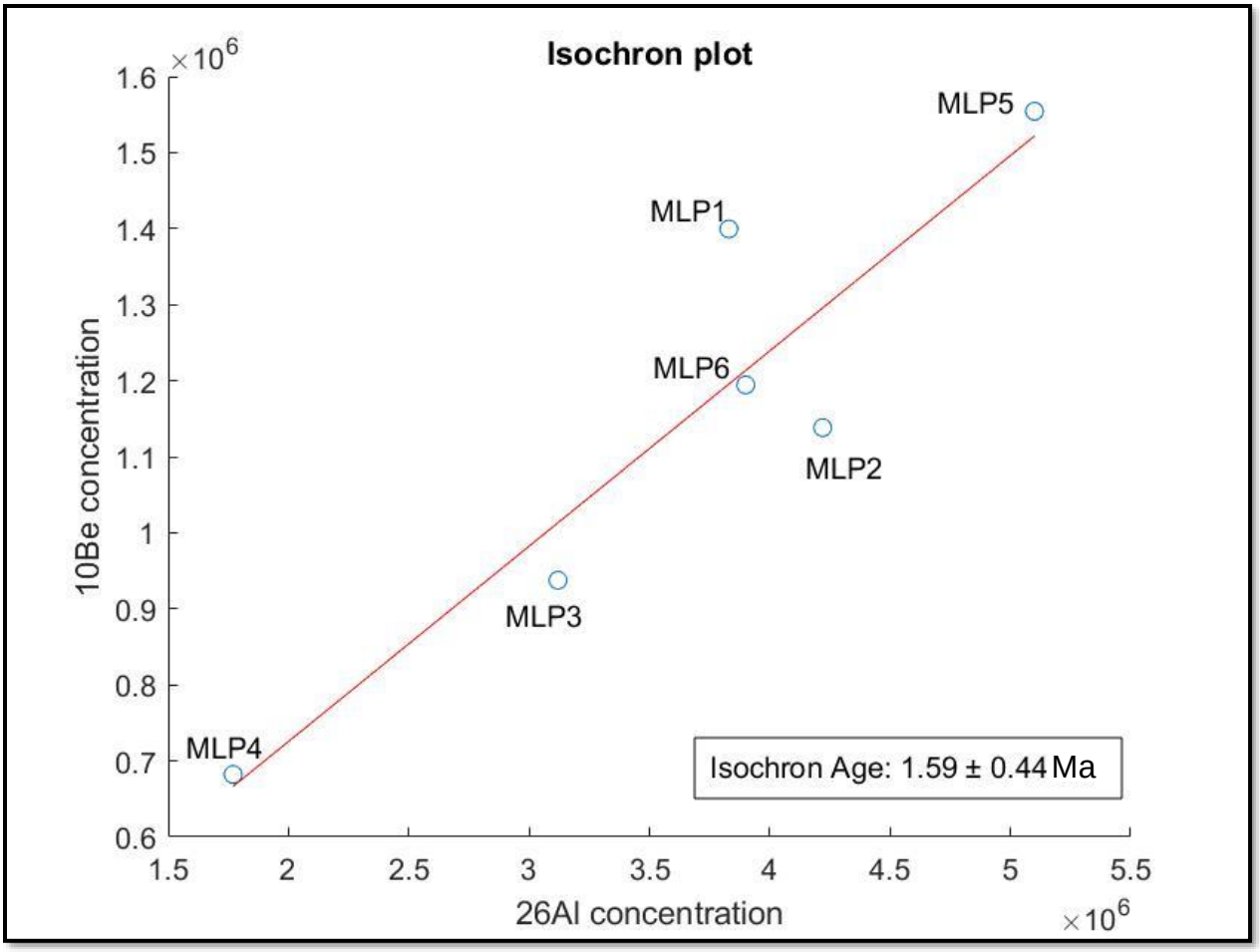


Figure 45: Image showing the isochron cosmogenic burial age calculated from sample MLP1CN – MLP6CN. The age is 1.59 ± 0.44 Ma.

CHAPTER 6: DISCUSSION

6.1 Newly exposed deposits: interpretations

Six lithofacies have already been established at Malapa (Dirks et al., 2010; Pickering et al., 2011a). The newly exposed deposits and the deposits denoted as facies F by Pickering et al. (2011a) are henceforth grouped to be called upper member. The reason for grouping these deposits is that the petrographical descriptions determined facies F as a heterogeneous deposit. To assess whether the upper member is composed of facies already established i.e., A- F, the sample descriptions in chapter 3 have yielded the following results. Three facies i.e., facies B, C, and F were identified (Fig. 46). MLP1P, MLP3P, and MLP9P can be classified as facies F. They all have peloids and some sandy peloidal grains. MLP2P was identified as facies B for having >50% rounded peloids and some clastic sediments. MLP6P, MLP12P, and MLP14P were identified as facies C. They have peloids but also a ~15% of quartz, and ~20% Mn-Fe-coated grains. The rest of the samples could not be classified under the already established facies as they did not contain peloids, pellets, or ooids. These samples were composed of chert, quartz, Mn-Fe-coated grains, and some micrite matrix. These included sample MLP4P, MLP5P, MLP7P, MLP8P, MLP10P and MLP11P. These samples were then classified as facies G for they contained no peloids and a high number of detrital grains. Three of these samples from facies G contained fossils i.e., MLP4P, MLP5P, and MLP7P. Facies G is a new facies at Malapa introduced in this study to accommodate samples that do not contains peloids and composed of detrital grains with Fe-Mn-coating on their grains. This is the new proposed topmost facies before the dolomitic walls.

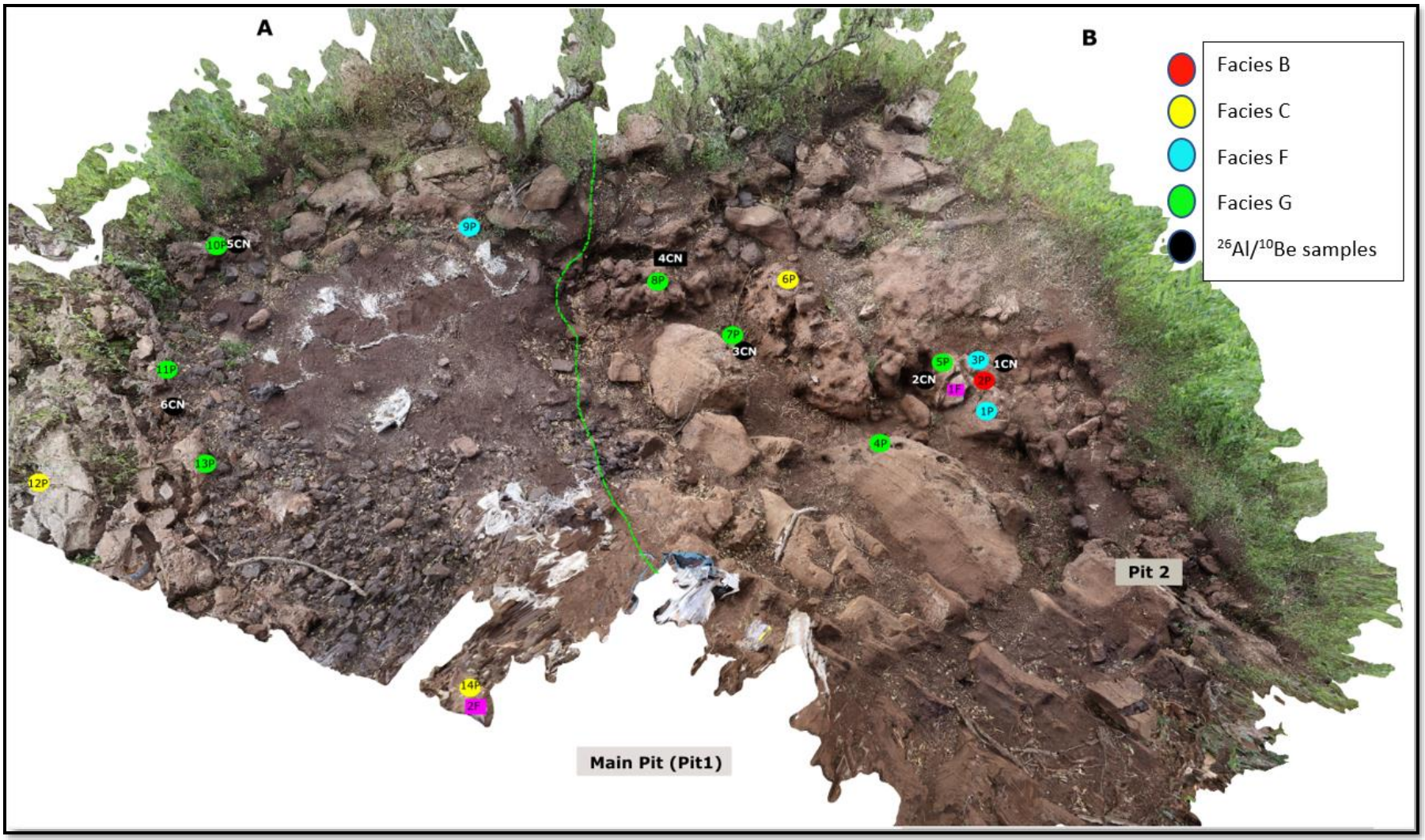

A
B
Facies B
Facies C
Facies F
Facies G
$^{26}Al/^{10}Be$ samples
9P
10P
5CN
4CN
8P
6P
7P
3CN
11P
6CN
13P
12P
5P
3P
1CN
2CN
2P
1F
1P
4P
Pit 2
14P
2F
Main Pit (Pit1)

Figure 46: Photogrammetry photo encompassing the upper member deposits, Pit 1 and Pit 2 at Malapa. The image shows where each sample comes from and which facies they fall under. The photo also shows where the cosmogenic samples were samples relative to the petrographic samples. Three facies already described at Malapa are present in the upper member deposits i.e., facies B, C and F. Facies G is found all over the upper member and in area A, it occurs right at the edge of the dolomitic walls. Photogrammetry photo cred: Paloma de la Peña.

The presence of Facies B and C in the upper member can be explained using stratigraphic laws. Since it is possible for chronologically different facies to form under similar depositional environments and be lithologically similar (Murszewski et al., 2020); it is possible for the processes that formed facies B and C in the main pit and top of block 3 in pit 2 to have formed similar deposits in the upper member. Simply put, the processes and depositional environment that occurred in the main pit could have formed the deposits in the upper member even if they are chronologically different. Sedimentary processes can repeat over time under similar depositional settings. Also, it is possible that facies of different lithologies grade into each other and occur in separate parts of the site thus producing synchronous distinct lithological units. Pickering et al. (2011a) correlated facies C to block 3 using its petrographic characteristics and stratigraphic relations. With the same characteristics observed in this study for both facies B and C, it can be inferred that the processes that formed facies B and C in the main pit have repeated to form them in the upper member. The presence of Facies F in the upper member was already thought to have formed under similar conditions to the one in the main pit by Pickering et al. (2011a). This study agrees with the findings of Pickering et al. (2011a) in that regard.

The chemical classification of the rocks in the upper member showed that the sediments are more mature, meaning that they have an increase in quartz grains (facies G) coupled with a decrease in grains such as feldspars and lithic fragments (Bhatia, 1983). Seeing that the trends in Harker diagrams are mostly weakly correlated or scattered, it can be inferred that this was a result of three component mixing (calcite-quartz-ilmenite) (Argast and Donnelly, 1987). All other samples are depleted in Al_20_3, SiO_2, and Fe_2O_3 compared to global standards because they are forming calcium-rich framework grains. It is no surprise they would be enriched in calcium compared to the three global standards. Although the sediment in the Cradle is variable, the regional sediment chemistry is not aligned with the sediment fill at Malapa. For example, the shales of the Cradle are highly aluminous and contain little CaO Wt% which is the opposite of the chemical configuration of the upper member samples (Reimer, 1992; Meyer and Robb, 1996).

According to Dirks et al. (2010) and Pickering et al. (2011b), facies B was deposited on a muddy cave floor along with local speleothem deposition. Facies C was interpreted as pellets accumulated as mud on the base of cave chambers. Facies F was interpreted as water-logged sediments by the previous studies. The sandstone samples display a loose packing of framework grains meaning they are poorly sorted (Dirks et al., 2010). This was interpreted as an indication of little post-depositional compaction of the grains according to Blatt et al. (2006). The abundant pore spaces of rocks in facies B were interpreted as trapped gas formed probably by organic matter decay (Tucker, 1991, Blatt et al., 2006). The peloids themselves were interpreted as either soil micropeds or fecal remains (Pickering et al., 2007; Retallack, 1990). The peloids disintegrating was interpreted as a mechanical reworking of the water-logged unconsolidated peloids (Dirk et al., 2010). The sandstones comprise of allochthonous sediments such as chert, quartz, bone fragments, and shale fragments (Dirks et al., 2010). The literature also interpreted the presence of isopachous

sparite as indicating that cementation occurred in a phreatic environment soon after deposition. Makhubela (2014) not only identified types of Mn-Fe-oxyhydroxides, but the study also dated the grains that formed peloidal nodules. These grains and coating types together with inclusions within them were identified as different mineral phases. Anatase, goethite, siderite, and hematite were some of the mineral phases identified (Makhubela, 2014). The inclusions were narrowed down to muscovite and phlogopite (Makhubela, 2014). The interpretations of that study concluded that the nodules are older than other sediments and could have been derived from the Malmani dolomite host rock (Makhubela, 2014). This interpretation was aided by $^{40}Ar/^{39}Ar$ ages that suggested the nodules to have formed in the Proterozoic era. The Makhubela (2014) study did isolate type 4 nodules from this interpretation, giving evidence that the grains formed in situ with low concentrations of uranium and thorium. The study also associated these grains with a hydrothermal, non-biological process of formation.

By assessing existing data at Malapa, it is possible to assume that all framework, accessory, and minor grains encountered and described in this study are the same as those from Dirks et al. (2010), and Pickering et al. (2011b). Assessing the matrix, carbonate grains, and non-carbonate constituents encountered in upper member samples; it was possible to confirm the depositional interpretations that were made in previous studies. The upper member rocks' common non-skeletal grains include peloids, clasts, coated grains, and grain aggregates. Micrite matrix, isopachous cement, and sprite are the main groundmass. The non-carbonate constituents are the detrital grains i.e., chert, quartz, and aggregate grains of both quartz and chert. The peloids in this study are mostly rounded and some have irregular shapes which can be interpreted as deposited platform wide. These indicate that the peloids can either be classified as fecal pellets, algal peloids, and mud peloids (Flugel, 2010). By the peloid size alone, algal peloids no longer qualify. Algal peloids can

only reach up to 2mm and the peloids in this study are mostly larger than that. The peloids can either be fecal pellets or mud peloids which means they are either of biotic origin (lithified organic excrements) or reworking of mud and grains origin (a post-sedimentary reworking of carbonate mud and micrite). The peloids in this study are more likely to be mud peloids than fecal pellets as no bioturbation structures were observed compared to those reported by Dirks et al. (2010) and Pickering et al. (2011b). The silicate addition to the carbonate system could be from river input (White, 2007) and silica supplied from hydrothermal fluids (Flugel, 2010). Without further evidence, is impossible to speculate which one is more likely to have added the silicate component to this samples.

A stratigraphic column to put things into perspective is provided below. See fig. 47.

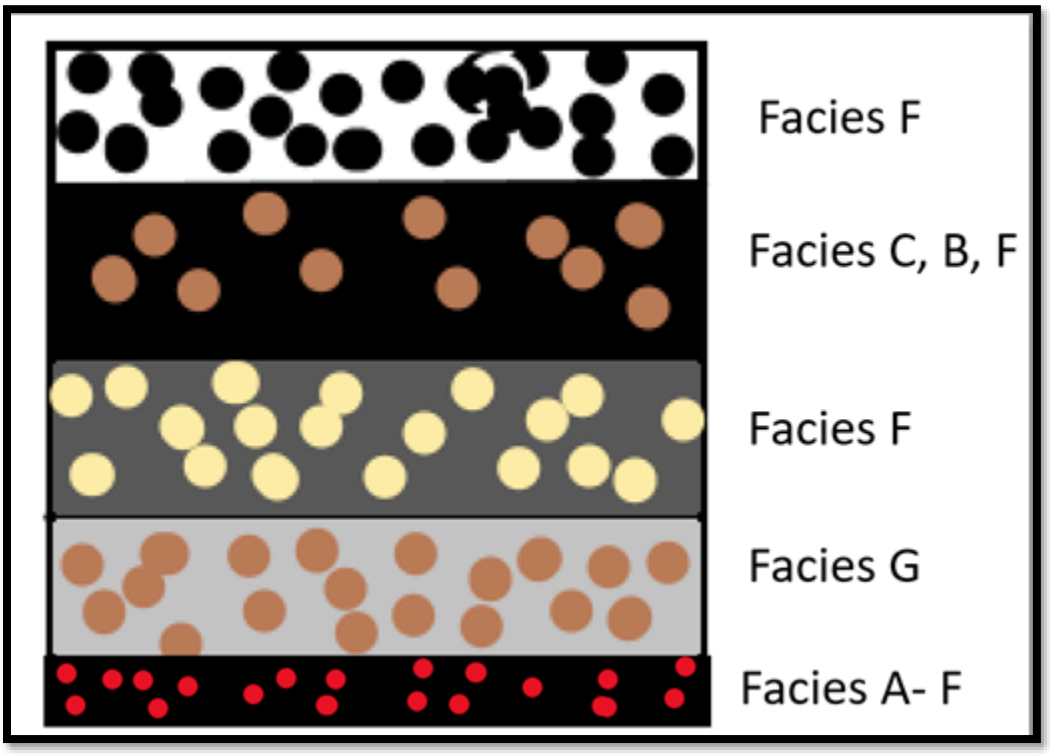


Figure 47: Summary stratigraphic column drawn to demonstrate that facies are repeating as we approach the dolomitic walls. More than one facies were exposed at a time. Flowstone 3 would be where there are multiple facies exposed.

6.2 Facies G

The homogenous fine-grained matrix (micrite) found in all facies including facies G can be interpreted as a diagenetic feature according to Flugel (2010). Facies G comprises of micrite matrix, various coated grains, some grain aggregates, and detrital clasts. This facies G could be a result of sedimentation in the cave where fewer carbonate minerals were being deposited in the system. More silica from either hydrothermal fluid or river input enriched the sediments to form less calcite and more quartz and chert grains although the latter is unlikely. No channel input has been proven or even observed therefore, it is unlikely to be a contributor. The candidate did entertain the idea of a textural variation within the same facies as noted in Dirks et al. (2010) where samples taken at the bottom of the facies are different from the samples taken towards the top of facies. This was disproved with the sampling technique used, which was random with adequate spacing laterally and vertically.

6.3 Geochronology interpretations

6.3.1 U-Pb

To assess the chronology of the upper member, two flowstones were dated using the U-Pb method. MLP1F which was in situ when sampling yielded an age of 3.72 Ma. This age does not align with known ages at Malapa and in the Cradle. The Cradle sediment fill has been confined by reliable dates to be between 1Ma and 3.2Ma. The age is also in disagreement with a well constrained age of the flowstone by Pickering et al. (2011a) who dated the flowstone using MC-ICP-MS method

in two separate labs. The age thus does not make logical sense. The age also has a significant amount of error. Pickering and Edwards (2021) investigated factors controlling age quality in the Cradle and classified three groups based on % error and final U-Pb ages. The age quality groups; the good (error < 5%), the bad (error of 5% to 10%) and the ugly (error of >10%). Malapa has produced one good age (Dirks et al., 2010) and one bad age (Pickering et al., 2011a). The age produced in this study is considered an ugly age (n= 34). Factors attributed to be controlling ugly ages is that there is a low spread of isochron, low levels of radiogenic Pb and high Pb concentrations from detrital grains. Ugly ages also result from samples that have undergone heavy diagenesis that the original trace is gone which makes it impossible to compute an age (Pickering and Edwards, 2021). To get good ages, a lower Pb concentration is better whereas U concentration has little to no effect on the quality of the age (Pickering and Edwards, 2021). Although, U concentrations of approximately 1 ppm preserves good trace signals. The ugly age could be as a results of method inaccuracy and precision on low-U and or young samples. Most speleothems in the Cradle contain < 1 ppm U. The age obtained for this study is an ugly age, this could not have been caused by a lack of number of points defining the isochron line since n=24. The low spread in the isochron lien could be the reason why the age is considered ugly. Most points in the isochron are concentrated in one place. Implications for this ugly age is that it cannot be used to constrain any deposit as the error is too large.

In summary, the method LA-ICP-MS has four limitations i.e., isotopic composition of common lead, dating young material which introduces disequilibria, dating old material which introduces the potential of dealing with an open system and lastly analytical limitations (Roberts et al., 2020). The largest contributor of uncertainty to LA-ICP-MS dates is elemental fractionation during an analytical session (Roberts et al., 2020). The ugly age places the upper member to be Pliocene in

age and not Pleistocene. This has no meaning however because the age doesn't make sense. Hence, information cannot be inferred about how old the upper member is based on this age. The flowstones inside the main pit and those of pit 2 are around 2 Ma in age.

The second flowstone (MLP2F) is 7.50 Ma in age making it Miocene in age. This flowstone is an ex-situ clast found in between facies C sediments. The error within the age is below 5% and can be regarded as a "good" age according to Pickering and Edwards (2021). The flowstone exhibits a simple fabric of columnar compact. Because of the LA-ICP-MS analytical limitations on samples with low U concentrations, this age is questionable just MLP1F. In the Cradle, there hasn't been ages reported of this age for the speleothems. Speleogenesis is even proposed to have occurred contemporary at ~2 Ma across most fossil-bearing sites (Pickering et a., 2011b). Because the occurrence of a flowstone that is Miocene in age is highly unlikely in the Cradle, the same flowstone can be sampled again and dated using MC-ICP-MS which is more accurate than LA-ICP-MS to get a well constrained age. As it is, the candidate can hypothesise that this flowstone may be a collapsed clast from the cave roof considering how old it seems to be. If the age was well-constrained, this would have been evidence for a speleogenesis event that hasn't been preserved in the Cradle due to cave de-roofing and subsequent erosion events.

MLP1F and MLP2F fabrics such as columnar compact, columnar open, columnar faint, and fascicular optic calcite can be interpreted as flowstones forming at relatively low supersaturation and a regular flow (Frisia et al., 2000; Frisia, 2014). Discharge variability can be induced by open columnar fabric (Boch et al., 2011). One can also speculate or hypothesise that due to MLP3F having less calcite fabrics, it preserved more trace than MLP2F which was suitable for dating.

6.3.2 $^{10}Be/^{26}Al$

The clastic sediments of the upper member were dated and returned an isochron burial age of 1.59 ± 0.44 Ma. This age gives a range of 1.15 - 2.03 Ma. The age of 2.03 Ma aligns with the ages of Dirks et al., 2010 and Pickering et al., 2011a. However, this range also means that the deposits were formed sometime within this period from 1.15 Ma to 2.03 Ma. The minimum age of the upper member deposits is 1.15 Ma which suggests that the upper member deposits are younger than those in the main pit. It is also possible to treat the individual ages obtained to entertain the idea of temporal variation of facies in Malapa. Sample MLP2CN, MLP3CN, MLP5CN, and MLP6CN all occurs within facies G. The ages ranges between 1.39 - 1.57 Ma with an average of 1.52 Ma. Facies G age can be attributed to 1.52 ± 0.088 Ma which is the average of the four samples that occurs within it. Sample MLP1CN was sampled in the deposits of facies F and yielded an age of 1.88 ± 0.15 Ma. Sample MLP4CN which was sampled close to the dolomitic walls in facies C yielded an age of 1.98 ± 0.1Ma. From assessing this data, it can be said that there could be two different phases of deposition represented in the upper member. Within error, the facies C and F deposits could most likely be forming between the pre-Olduvai event (~1.977 Ma) and early Olduvai Subchron (1.95- 1.78 Ma) marking the first phase. Facies C, D, and E palaeomagnetic data has been interpreted as the beginning of Olduvai Subchron by Dirks et al (2010). This study, within error can support the findings of Dirks et al. (2010) for facies C using cosmogenic nuclide dates. The second phase could be one of facies G, this is the youngest deposit in the site and the study proposes facies G to be the topmost deposit at Malapa. The candidate acknowledges that cosmogenic burial dating method has drawbacks in chapter 2 and one of them is yielding large uncertainties most of time either due to methodological or analytical uncertainties (Dunai, 2010).

This is seen with the age obtained in this study, the error is 0.44 Ma which is ~28% of the age. That is the disadvantage of using the cosmogenic nuclide burial method compared to U-Pb method.

CHAPTER 7: CONCLUSION

In conclusion, the upper member is not composed of new deposits of facies F. The upper member is composed of facies B, C, and F which are Early Pleistocene in age, and facies G of which the age is proposed to be 1.52 ± 0.088 Ma based on cosmogenic nuclide dates. This means that facies G is Early Pleistocene in age. The research was able to disprove that the newly exposed deposits now referred to as upper member are not composed of new deposit of facies F deposit only but of other facies found in the main pit. These facies are lithologically similar but chronologically different. Facies F is present in the upper member deposits, and it has been dated to be Early Pleistocene, this means that upper member has Early Pleistocene deposits exposed. The hypothesis that the upper member is composed of multiple different facies is true, and they are all Early Pleistocene in age. The upper member is composed of new facies and comprises of younger facies G deposits. This could not be proven with the resultant data of this dissertation. The upper member is composed of multiple facies, it has a more depositional environment as discussed in preceding chapters.

The new cosmogenic nuclide ages are young and overlap with deposits of Coopers'D cave and Swartkrans. These deposits of age 1.39 to 1.58 Ma are associated with the deposition of Paranthropus robustus in the Cradle. By just assessing the ages, upper member facies G deposits are being deposited at the same time deposits of Member 2 in Swartkrans. Member 2 of Swartkrans is composed of fossils, bone and stone artefacts encased in a brown breccia which is different to facies G. Although Coopers' D deposits are fossil rich and encased in breccia, the breccia has abundant quartz and chert like facies G.

REFERENCES

Adams, J.W., 2012. A revised listing of fossil mammals from the Haasgat cave system ex situ deposits (HGD), South Africa. *Palaeontologia electronica*, *15*(3), pp.1-88.

Adams, J.W., Hemingway, J., Kegley, A.D.T. and Thackeray, J.F., 2007. Luleche, a new paleontological site in the Cradle of Humankind, North-West Province, South Africa. *Journal of human evolution*, *53*(6), pp.751-754.

Adams, J.W., Herries, A.I.R., Hemingway, J., Kegley, A.D., Kgasi, L., Hopley, P., Reade, H., Potze, S. and Thackeray, J.F., 2010. Initial fossil discoveries from Hoogland, a new Pliocene primate-bearing karstic system in Gauteng Province, South Africa. *Journal of Human Evolution*, *59*(6), pp.685-691.

Adams, J.W., Rovinsky, D.S., Herries, A.I. and Menter, C.G., 2016. Macromammalian faunas, biochronology and palaeoecology of the early Pleistocene Main Quarry hominin-bearing deposits of the Drimolen Palaeocave System, South Africa. *PeerJ*, *4*, p.e1941.

Alexandre, P., Andreoli, M.A., Jamison, A. and Gibson, R.L., 2006. 40Ar/39Ar age constraints on low-grade metamorphism and cleavage development in the Transvaal Supergroup (central Kaapvaal craton, South Africa): implications for the tectonic setting of the Bushveld Igneous Complex. *South African Journal of Geology*, *109*(3), pp.393-410.

Andreoli, M.A.G., 1988. Evidence for thrust tectonics in the Transvaal Sequence based on geophysical profiles. *Extended Abstracts, Geocongress' 88, Geological Society of South Africa*, *3*(6).

Argast, S. and Donnelly, T.W., 1987. The chemical discrimination of clastic sedimentary components. *Journal of Sedimentary Research*, *57*(5), pp.813-823.

Beaudoin, N., Lacombe, O., Roberts, N.M.W. and Koehn, D., 2018. U-Pb dating of calcite veins reveals complex stress evolution and thrust sequence.

Berger, L., 2012. Australopithecus sediba and the earliest origins of the genus Homo. *J Anthropol Sci*, *90*, pp.117-131.

Berger, L.R., De Ruiter, D.J., Churchill, S.E., Schmid, P., Carlson, K.J., Dirks, P.H. and Kibii, J.M., 2010. Australopithecus sediba: a new species of Homo-like australopith from South Africa. *Science*, *328*(5975), pp.195-204.

Berger, L.R., De Ruiter, D.J., Steininger, C.M. and Hancox, J., 2003. Preliminary results of excavations at the newly investigated Coopers D deposit, Gauteng, South Africa: preliminary research reports: human origins research in South Africa. *South African Journal of Science*, *99*(5), pp.276-278.

Berger, L.R., Hawks, J., de Ruiter, D.J., Churchill, S.E., Schmid, P., Delezene, L.K., Kivell, T.L., Garvin, H.M., Williams, S.A., DeSilva, J.M. and Skinner, M.M., 2015. Homo naledi, a new species of the genus Homo from the Dinaledi Chamber, South Africa. *elife*, *4*, p.e09560.

Berger, L.R., Hawks, J., de Ruiter, D.J., Churchill, S.E., Schmid, P., Delezene, L.K., Kivell, T.L., Garvin, H.M., Williams, S.A., DeSilva, J.M. and Skinner, M.M., 2015. Homo naledi, a new species of the genus Homo from the Dinaledi Chamber, South Africa. *elife*, *4*, p.e09560.

Berger, L.R., Keyser, A.W. and Tobias, P.V., 1993. Gladysvale: first early hominid site discovered in South Africa since 1948. *American Journal of Physical Anthropology*, *92*(1), pp.107-111.

Bertok, C., Barale, L., d'Atri, A., Martire, L., Piana, F., Rossetti, P. and Gerdes, A., 2019. Unusual marbles in a non-metamorphic succession of the SW Alps (Valdieri, Italy) due to early Oligocene hydrothermal flow. *International Journal of Earth Sciences*, *108*(2), pp.693-712.

Bhatia, M.R., 1983. Plate tectonics and geochemical composition of sandstones. *The Journal of Geology*, *91*(6), pp.611-627.

Blatt, H., Tracy, R. and Owens, B., 2006. *Petrology: igneous, sedimentary, and metamorphic*. Macmillan.

Boch, R., Spoetl, C. and Frisia, S., 2011. Origin and palaeoenvironmental significance of lamination in stalagmites from Katerloch Cave, Austria. *Sedimentology*, *58*(2), pp.508-531.

Bosch, R.F. and White, W.B., 2004. *Lithofacies and transport of clastic sediments in karstic aquifers* (pp. 1-22). Springer US.

Braga, J., Thackeray, J.F. and Zipfel, B., 2022. The Kromdraai early hominin-bearing site. A review of recent findings. *L'Anthropologie*, p.103054.

Braga, J., Thackeray, J.F., Bruxelles, L., Dumoncel, J. and Fourvel, J.B., 2017. Stretching the time span of hominin evolution at Kromdraai (Gauteng, South Africa): Recent discoveries. *Comptes Rendus Palevol*, *16*(1), pp.58-70.

Brain, C.K. and Sillent, A., 1988. Evidence from the Swartkrans cave for the earliest use of fire. *Nature*, *336*(6198), pp.464-4

Brain, C.K. ed., 1993. *Swartkrans: A cave's chronicle of early man* (Vol. 8). Transvaal Museum.

Brain, C.K. ed., 1993. *Swartkrans: A cave's chronicle of early man* (Vol. 8). Transvaal Museum.

Brain, C.K., 1976. A re-interpretation of the Swartkrans site and its remains. *South African Journal of Science*, *72*(5), p.141.

Brain, C.K., 1983. *The hunters or the hunted?: an introduction to African cave taphonomy*. University of Chicago Press.

Brain, CK, Watson, V., Grine, F. E. "Swartkrans; a cave's chronicle of early man. Structure and stratigraphy of the Swartkrans Cave in the light of the new excavations. Composition of the Swartkrans bone accumulations in terms of skeletal parts and animals represented. Description and preliminary analysis of new hominid craniodental fossils from the Swartkrans formation." *Transvaal Museum Monographs* 8, no. 1 (2004).

Broom, R., 1937. Discovery of a lower molar of Australopithecus. *Nature*, *140*(3546), pp.681-682.

Broom, R., 1938. The pleistocene anthropoid apes of South Africa. *Nature*, *142*(3591), pp.377-379.

Broom, R., 1939. A preliminary account of the Pleistocene carnivores of the Transvaal caves. *Annals of the Transvaal Museum*, *19*(3), pp.331-338.

Brouwer, P., 2006. Theory of XRF. *Almelo, Netherlands: PANalytical BV*.

Bruxelles, L., Maire, R., Couzens, R., Thackeray, J.F. and Braga, J., 2016. A revised stratigraphy of Kromdraai. *Kromdraai, a birthplace of Paranthropus in the Cradle of Humankind. SUN MeDIA MeTRO, Stellenbosch, South Africa*, pp.31-47.

Burisch, M., Gerdes, A., Walter, B.F., Neumann, U., Fettel, M. and Markl, G., 2017. Methane and the origin of five-element veins: Mineralogy, age, fluid inclusion chemistry and ore forming processes in the Odenwald, SW Germany. *Ore Geology Reviews*, *81*, pp.42-61.

Button, A., 1973. The stratigraphic history of the Malmani dolomite in the eastern and north-eastern Transvaal. *South African Journal of Geology*, *76*(3), pp.229-247.

Butzer, K.L.W., 1976. Lithostratigraphy of the Swartkrans formation. *South African Journal of Science*, *72*(5), p.136.

Caruana, M.V. and Stratford, D.J., 2019. Historical perspectives on the significance of archaeology in the Cradle of Humankind, South Africa. *South African Archaeological Society Goodwin Series*, *12*, pp.44-55.

Caruana, M.V., Tasker, D. and Stratford, D.J., 2019. Identifying raw material transportation and reduction strategies from the lithic scatters at Elandsdrift Farm (Cradle of Humankind World Heritage Site), South Africa. *African Archaeological Review*, *36*, pp.271-289.

Churchill, S.E., KIBII, J., Schmid, P., Reed, N.D. and BERGER, L., 2018. Australopithecus sediba. *PaleoAnthropology*, *334*, p.356.

Clarke, F.W. and Washington, H.S., 1924. *The composition of the earth's crust* (Vol. 127). US Government Printing Office.

Clarke, R., 2013. Australopithecus from Sterkfontein Caves, South Africa. *The paleobiology of Australopithecus*, pp.105-123.

Clarke, R.J., 1977. The cranium of the Swartkrans hominid, SK 847 and its relevance to human origins [PhD dissertation]. *Johannesburg: University of the Witwatersrand*.

Clarke, R.J., 1994. The significance of the Swartkrans Homo to the Homo erectus problem. *Courier Forschungs-Institut Senckenberg*, *171*, pp.185-193.

Clarke, R.J., Howell, F.C. and Brain, C.K., 1970. New finds at the Swartkrans australopithecine site (contd): More evidence of an advanced hominid at Swartkrans. *Nature*, *225*, pp.1219-1222.

Coogan, L.A., Parrish, R.R. and Roberts, N.M., 2016. Early hydrothermal carbon uptake by the upper oceanic crust: Insight from in situ U-Pb dating. *Geology*, *44*(2), pp.147-150.

Curnoe, D., Grün, R., Taylor, L. and Thackeray, F., 2001. Direct ESR dating of a Pliocene hominin from Swartkrans. *Journal of Human Evolution*, *40*(5), pp.379-391.

Dart, R.A. and Salmons, A., 1925. Australopithecus africanus: the man-ape of South Africa. *A Century of Nature: Twenty-One Discoveries that Changed Science and the World*, pp.10-20.

De Ruiter, D.J., 2003. A revised faunal list for the Australopithecine-bearing Members of Swartkrans. *Annals of the Transvaal Museum, 39*, pp.29-41.

de Ruiter, D.J., Pickering, R., Steininger, C.M., Kramers, J.D., Hancox, P.J., Churchill, S.E., Berger, L.R. and Backwell, L., 2009. New australopithecus robustus fossils and associated U-Pb dates from Cooper's cave (Gauteng, South Africa). *Journal of Human Evolution*, *56*(5), pp.497-513.

DeSilva, J.M., Holt, K.G., Churchill, S.E., Carlson, K.J., Walker, C.S., Zipfel, B. and Berger, L.R., 2013. The lower limb and mechanics of walking in Australopithecus sediba. *Science*, *340*(6129), p.1232999.

Dirks, P.H. and Berger, L.R., 2013. Hominin-bearing caves and landscape dynamics in the Cradle of Humankind, South Africa. *Journal of African Earth Sciences*, *78*, pp.109-131.

Dirks, P.H., Berger, L.R., Roberts, E.M., Kramers, J.D., Hawks, J., Randolph-Quinney, P.S., Elliott, M., Musiba, C.M., Churchill, S.E., de Ruiter, D.J. and Schmid, P., 2015. Geological and taphonomic context for the new hominin species Homo naledi from the Dinaledi Chamber, South Africa. *Elife*, *4*, p.e09561.

Dirks, P.H., Kibii, J.M., Kuhn, B.F., Steininger, C., Churchill, S.E., Kramers, J.D., Pickering, R., Farber, D.L., Mériaux, A.S., Herries, A.I. and King, G.C., 2010. Geological setting and age of Australopithecus sediba from southern Africa. *Science*, *328*(5975), pp.205-208.

Dirks, P.H., Placzek, C.J., Fink, D., Dosseto, A. and Roberts, E., 2016. Using 10Be cosmogenic isotopes to estimate erosion rates and landscape changes during the Plio-Pleistocene in the Cradle of Humankind, South Africa. *Journal of Human Evolution*, *96*, pp.19-34.

Dirks, P.H., Roberts, E.M., Hilbert-Wolf, H., Kramers, J.D., Hawks, J., Dosseto, A., Duval, M., Elliott, M., Evans, M., Grün, R. and Hellstrom, J., 2017. The age of Homo naledi and associated sediments in the Rising Star Cave, South Africa. *Elife*, *6*, p.e24231.

Drake, H., Heim, C., Roberts, N.M., Zack, T., Tillberg, M., Broman, C., Ivarsson, M., Whitehouse, M.J. and Åström, M.E., 2017. Isotopic evidence for microbial production and consumption of methane in the upper continental crust throughout the Phanerozoic eon. *Earth and Planetary Science Letters*, *470*, pp.108-118.

Drake, H., Mathurin, F.A., Zack, T., Schäfer, T., Roberts, N.M., Whitehouse, M., Karlsson, A., Broman, C. and Åström, M.E., 2018. Incorporation of metals into calcite in a deep anoxic granite aquifer. *Environmental science & technology*, *52*(2), pp.493-502.

Drake, H., Roberts, N.M. and Whitehouse, M.J., 2020. Geochronology and stable isotope analysis of fracture-fill and karst mineralization reveal sub-surface paleo-fluid Flow and microbial activity of the COSC-1 Borehole, Scandinavian Caledonides. *Geosciences*, *10*(2), p.56.

Drake, H., Roberts, N.M., Heim, C., Whitehouse, M.J., Siljeström, S., Kooijman, E., Broman, C., Ivarsson, M. and Åström, M.E., 2019. Timing and origin of natural gas accumulation in the Siljan impact structure, Sweden. *Nature communications*, *10*(1), p.4736.

Drost, K., Chew, D., Petrus, J.A., Scholze, F., Woodhead, J.D., Schneider, J.W. and Harper, D.A., 2018. An image mapping approach to U-Pb LA-ICP-MS carbonate dating and applications to direct dating of carbonate sedimentation. *Geochemistry, Geophysics, Geosystems*, *19*(12), pp.4631-4648.

Dunai, T.J., 2010. *Cosmogenic nuclides: principles, concepts and applications in the earth surface sciences*. Cambridge University Press.

Edwards, H.G., Carter, E.A., Kelloway, S.J., Privat, K.L. and Harrison, T.M., 2021. Raman spectroscopic and elemental analysis of bone from a prehistoric ancestor: Mrs Ples from the Sterkfontein cave. *Journal of Raman Spectroscopy*, *52*(12), pp.2272-2281.

Edwards, T. and Pickering, R., 2022, May. A simple sedimentological model demystifying the complexity of fossil bearing cave deposits in the Cradle of Humankind, South Africa. In *EGU General Assembly Conference Abstracts* (pp. EGU22-6299).

Edwards, T.R., Armstrong, B.J., Birkett-Rees, J., Blackwood, A.F., Herries, A.I., Penzo-Kajewski, P., Pickering, R. and Adams, J.W., 2019. Combining legacy data with new drone and DGPS mapping

to identify the provenance of Plio-Pleistocene fossils from Bolt's Farm, Cradle of Humankind (South Africa). *PeerJ*, *7*, p.e6202.

Thackeray, J.F., 2020. A summary of the history of exploration at the Sterkfontein Caves in the Cradle of Humankind World Heritage Site. *Hominin Postcranial Remains from Sterkfontein, South Africa, 1936-1995*, p.1.

Edwards, T.R., Armstrong, B.J., Birkett-Rees, J., Blackwood, A.F., Herries, A.I., Penzo-Kajewski, P., Pickering, R. and Adams, J.W., 2019. Combining legacy data with new drone and DGPS mapping to identify the provenance of Plio-Pleistocene fossils from Bolt's Farm, Cradle of Humankind (South Africa). *PeerJ*, *7*, p.e6202.

Edwards, T.R., Pickering, R., Mallett, T.L. and Herries, A.I., 2023. Challenging the antiquity of the Cradle of Humankind, South Africa: Geochronological evidence restricts the age of Eurotomys bolti and Parapapio to less than 2.3 Ma at Waypoint 160, Bolt's Farm. *Journal of Human Evolution*, *178*, p.103334.

Edwards, T.R., Pickering, R., Mallett, T.L. and Herries, A.I., 2023. Challenging the antiquity of the Cradle of Humankind, South Africa: Geochronological evidence restricts the age of Eurotomys bolti and Parapapio to less than 2.3 Ma at Waypoint 160, Bolt's Farm. *Journal of Human Evolution*, *178*, p.103334

Edwards, T.R., Pickering, R., Mallett, T.L. and Herries, A.I., 2023. Challenging the antiquity of the Cradle of Humankind, South Africa: Geochronological evidence restricts the age of Eurotomys bolti and Parapapio to less than 2.3 Ma at Waypoint 160, Bolt's Farm. *Journal of Human Evolution*, *178*, p.103334.

Edwards, T.R., Pickering, R., Mallett, T.L. and Herries, A.I., 2020. Reconstructing the depositional history and age of fossil-bearing palaeokarst: A multidisciplinary example from the terminal Pliocene Aves Cave Complex, Bolt's farm, South Africa. *Results in Geophysical Sciences*, *1*, p.100005.

Edwards, T.R., Pickering, R., Mallett, T.L. and Herries, A.I., 2023. Challenging the antiquity of the Cradle of Humankind, South Africa: Geochronological evidence restricts the age of Eurotomys bolti and Parapapio to less than 2.3 Ma at Waypoint 160, Bolt's Farm. *Journal of Human Evolution*, *178*, p.103334.

Edwards, T.R., Pickering, R., Mallett, T.L. and Herries, A.I., 2023. Challenging the antiquity of the Cradle of Humankind, South Africa: Geochronological evidence restricts the age of Eurotomys bolti and Parapapio to less than 2.3 Ma at Waypoint 160, Bolt's Farm. *Journal of Human Evolution*, *178*, p.103334.

Edwards, T.R., Pickering, R., Mallett, T.L. and Herries, A.I., 2020. Reconstructing the depositional history and age of fossil-bearing palaeokarst: a multidisciplinary example from the terminal Pliocene Aves Cave Complex, Bolt's farm, South Africa. *Results in Geophysical Sciences*, *1*, p.100005.

Eriksson, KA & Truswell, J.F., 1974. Stratotypes from the Malmani subgroup north-west of Johannesburg, South Africa. *South African Journal of Geology*, *77*(3), pp.211-222.

Eriksson, P.G. and Altermann, W., 1998. An overview of the geology of the Transvaal Supergroup dolomites (South Africa). *Environmental Geology*, *36*, pp.179-188.

Eriksson, P.G. and Reczko, B.F.F., 1995. The sedimentary and tectonic setting of the Transvaal Supergroup floor rocks to the Bushveld Complex. *Journal of African Earth Sciences*, *21*(4), pp.487-504.

Eriksson, P.G., Altermann, W., Hartzer, F.J., Johnson, M.R., Anhaeusser, C.R. and Thomas, R.J., 2006. The Transvaal Supergroup and its precursors. *The Geology of South Africa*, pp.237-260.

Eriksson, P.G., Hattingh, P.J. and Altermann, W., 1995. An overview of the geology of the Transvaal Sequence and Bushveld Complex, South Africa. *Mineralium Deposita*, *30*, pp.98-111.

Eriksson, P.G., Schreiber, U.M., Reczko, B.F.F. and Snyman, C.P., 1994. Petrography and geochemistry of sandstones interbedded with the Rooiberg Felsite Group (Transvaal Sequence, South Africa); implications for provenance and tectonic setting. *Journal of Sedimentary Research*, *64*(4a), pp.836-846.

Eriksson, PG, Twist, D. G25, Snyman, CP & Burger, L., 1990. The geochemistry of the Silverton Shale Formation, Transvaal Sequence. *South African Journal of Geology*, *93*(3), pp.345-362.

Esterhuysen, A., 2007. *Sterkfontein: Early Hominid Site in the Cradle of Humankind*. Witwatersrand University Press.

Fairchild, I.J. and Baker, A., 2012. *Speleothem science: from process to past environments*. John Wiley & Sons.

Fairchild, I.J., Frisia, S., Borsato, A. and Tooth, A.F., 2006. Speleothems.

Flügel, E. (2010) *Microfacies of carbonate rocks: analysis, interpretation and application*. 2nd ed., Berlin: springer.

Forbes, M.S. and Bestland, E.A., 2007. Origin of the sedimentary deposits of the Naracoorte Caves, South Australia. *Geomorphology*, *86*(3-4), pp.369-392.

Fourvel, J.B. and Frerebeau, N., 2023. A new canid species (Carnivora: Canidae) from the Plio-Pleistocene hominin-bearing site of Kromdraai (Cradle of Humankind, Gauteng, South Africa). *PalZ*, *97*(1), pp.163-177.

Frisia S., 2015. Microstratigraphic logging of calcite fabrics in speleothems as tool for

Frisia, S. and Borsato, A., 2010. Karst. *Developments in sedimentology*, *61*, pp.269-318.

Frisia, S., 2014. Microstratigraphic logging of calcite fabrics in speleothems as tool for palaeoclimate studies.

Frisia, S., Borsato, A., Fairchild, I.J. and McDermott, F., 2000. Calcite fabrics, growth mechanisms, and environments of formation in speleothems from the Italian Alps and southwestern Ireland. *Journal of Sedimentary Research*, *70*(5), pp.1183-1196.

Ghinassi, M., Colonese, A.C., Giuseppe, Z.D., Govoni, L., Vetro, D.L., Malavasi, G., Martini, F., Ricciardi, S. and Sala, B., 2009. The Late Pleistocene clastic deposits in the Romito Cave, southern Italy: a proxy record of environmental changes and human presence. *Journal of Quaternary Science*, *24*(4), pp.383-398.

Gibbon, R.J., Pickering, T.R., Sutton, M.B., Heaton, J.L., Kuman, K., Clarke, R.J., Brain, C.K. and Granger, D.E., 2014. Cosmogenic nuclide burial dating of hominin-bearing Pleistocene cave deposits at Swartkrans, South Africa. *Quaternary Geochronology*, *24*, pp.10-15.

Godeau, N., Deschamps, P., Guihou, A., Leonide, P., Tendil, A., Gerdes, A., Hamelin, B. and Girard, J.P., 2018. U-Pb dating of calcite cement and diagenetic history in microporous carbonate reservoirs: Case of the Urgonian Limestone, France. *Geology*, *46*(3), pp.247-250.

Goldberg, P., 2000. Micromorphology and site formation at Die Kelders cave I, South Africa. *Journal of Human Evolution*, *38*(1), pp.43-90.

Gommery, D., Senegas, F., Badenhorst, S., Kgasi, L., Potze, S. and Thackeray, J.F., 2012. Preliminary results concerning the discovery of new fossiliferous sites at Bolt's Farm (Cradle of Humankind, South Africa). *Annals of the Ditsong National Museum of Natural History*, *2*(1), pp.33-45.

Goodfellow, B.W., Viola, G., Bingen, B., Nuriel, P. and Kylander-Clark, A.R., 2017. Palaeocene faulting in SE Sweden from U–Pb dating of slickenfibre calcite. *Terra Nova*, *29*(5), pp.321-328.

Gosse, J.C. and Phillips, F.M., 2001. Terrestrial in situ cosmogenic nuclides: theory and application. *Quaternary Science Reviews*, *20*(14), pp.1475-1560.

Grab, S. and Knight, J., 2015. *Landscapes and landforms of South Africa—an overview* (pp. 1-9). Springer International Publishing.

Granger, D. E., 2014. Cosmogenic Nuclide Burial Dating in Archaeology and Paleoanthropology. In: Holland, H. D., Turekian, K. K., (eds.), *Treatise on Geochemistry*, Second Edition, Volume 14: Archaeology and Anthropology: Oxford, Elsevier, p. 81-97. http://dx.doi.org/10.1016/B978-0-08-095975-7.01208-0

Granger, D.E. and Muzikar, P.F., 2001. Dating sediment burial with in situ-produced cosmogenic nuclides: theory, techniques, and limitations. *Earth and Planetary Science Letters*, *188*(1-2), pp.269-281.

Granger, D.E., Gibbon, R.J., Kuman, K., Clarke, R.J., Bruxelles, L. and Caffee, M.W., 2015. New cosmogenic burial ages for Sterkfontein member 2 Australopithecus and member 5 Oldowan. *Nature*, *522*(7554), pp.85-88.

Granger, D.E., Lifton, N.A. and Willenbring, J.K., 2013. A cosmic trip: 25 years of cosmogenic nuclides in geology. *Bulletin*, *125*(9-10), pp.1379-1402.

Granger, D.E., Stratford, D., Bruxelles, L., Gibbon, R.J., Clarke, R.J. and Kuman, K., 2022.

Cosmogenic nuclide dating of Australopithecus at Sterkfontein, South Africa. *Proceedings of the National Academy of Sciences*, *119*(27), p.e2123516119.

Boggs, S., 2009. *Petrology of sedimentary rocks*. Cambridge university press.

Granger, D.E., Stratford, D., Bruxelles, L., Gibbon, R.J., Clarke, R.J. and Kuman, K., 2022. Cosmogenic nuclide dating of Australopithecus at Sterkfontein, South Africa. *Proceedings of the National Academy of Sciences*, *119*(27), p.e2123516119.

Hansman, R.J., Albert, R., Gerdes, A. and Ring, U., 2018. Absolute ages of multiple generations of brittle structures by U-Pb dating of calcite. *Geology*, *46*(3), pp.207-210.

Harmon, R.S., Schwarcz, H.P., Gascoyne, M., Hess, J.W. and Ford, D.C., 2004. Paleoclimate information from speleothems: the present as a guide to the past. In *Studies of Cave Sediments: Physical and Chemical Records of Paleoclimate* (pp. 199-226). Springer US.

Hawks, J., Elliott, M., Schmid, P., Churchill, S.E., Ruiter, D.J.D., Roberts, E.M., Hilbert-Wolf, H., Garvin, H.M., Williams, S.A., Delezene, L.K. and Feuerriegel, E.M., 2017. New fossil remains of Homo naledi from the Lesedi Chamber, South Africa. *Elife*, *6*, p.e24232.

Hellwig, A., Voigt, S., Mulch, A., Frisch, K., Bartenstein, A., Pross, J., Gerdes, A. and Voigt, T., 2018. Late Oligocene to early Miocene humidity change recorded in terrestrial sequences in the Ili Basin (south-eastern Kazakhstan, Central Asia). *Sedimentology*, *65*(2), pp.517-539.

Herman, E.K., Toran, L. and White, W.B., 2012. Clastic sediment transport and storage in fluviokarst aquifers: an essential component of karst hydrogeology. *Carbonates and Evaporites*, *27*, pp.211-241.

Herries, A.I. and Adams, J.W., 2013. Clarifying the context, dating and age range of the Gondolin hominins and Paranthropus in South Africa. *Journal of Human Evolution*, *65*(5), pp.676-681.

Herries, A.I. and Shaw, J., 2011. Palaeomagnetic analysis of the Sterkfontein palaeocave deposits: Implications for the age of the hominin fossils and stone tool industries. *Journal of human evolution*, *60*(5), pp.523-539.

Herries, A.I., 2022. Chronology of the hominin sites of southern Africa. In *Oxford Research Encyclopedia of Anthropology*.

Herries, A.I., Adams, J.W., Kuykendall, K.L. and Shaw, J., 2006. Speleology and magnetobiostratigraphic chronology of the GD 2 locality of the Gondolin hominin-bearing paleocave deposits, North West Province, South Africa. *Journal of Human Evolution*, *51*(6), pp.617-631.

Herries, A.I., Curnoe, D. and Adams, J.W., 2009. A multi-disciplinary seriation of early Homo and Paranthropus bearing palaeocaves in southern Africa. *Quaternary International*, *202*(1-2), pp.14-28.

Herries, A.I., Hopley, P.J., Adams, J.W., Curnoe, D. and Maslin, M.A., 2010. Geochronology and palaeoenvironments of Southern African hominin-bearing localities—A reply to Wrangham et al., 2009. "Shallow-water habitats as sources of fallback foods for hominins". *American Journal of Physical Anthropology*, *143*(4), pp.640-646.

Herries, A.I., Kappen, P., Kegley, A.D., Patterson, D., Howard, D.L., de Jonge, M.D., Potze, S. and Adams, J.W., 2014. Palaeomagnetic and synchrotron analysis of> 1.95 Ma fossil-bearing palaeokarst at Haasgat, South Africa. *South African Journal of Science*, *110*(3-4), pp.01-12.

Herries, A.I., Martin, J.M., Leece, A.B., Adams, J.W., Boschian, G., Joannes-Boyau, R., Edwards, T.R., Mallett, T., Massey, J., Murszewski, A. and Neubauer, S., 2020. Contemporaneity of Australopithecus, Paranthropus, and early Homo erectus in South Africa. *Science*, *368*(6486), p.eaaw7293.

Herries, A.I., Pickering, R., Adams, J.W., Curnoe, D., Warr, G., Latham, A.G. and Shaw, J., 2013. A multi-disciplinary perspective on the age of Australopithecus in southern Africa. *The paleobiology of Australopithecus*, pp.21-40.

Hirschey, S.H., 2015. Speleothem Formation and Composition in Hot and Cool Cave: Assessing the reliability of paleoclimate archives in high CO2 environments.

Holdsworth, R.E., McCaffrey, K.J.W., Dempsey, E., Roberts, N.M.W., Hardman, K., Morton, A., Feely, M., Hunt, J., Conway, A. and Robertson, A., 2019. Natural fracture propping and earthquake-induced oil migration in fractured basement reservoirs. *Geology*, *47*(8), pp.700-704.

Holliday, T.W., Churchill, S.E., Carlson, K.J., DeSilva, J.M., Schmid, P., Walker, C.S. and BERGER, L., 2018. Australopithecus sediba Body Size and Proportions of Australopithecus sediba. *PaleoAnthropology*, *406*(6), pp.406-422.

Hopley, P.J., Reade, H., Parrish, R., De Kock, M. and Adams, J.W., 2019. Speleothem evidence for C3 dominated vegetation during the Late Miocene (Messinian) of South Africa. *Review of Palaeobotany and Palynology*, *264*, pp.75-89.

https://www.thermofisher.com/blog/ask-a-scientist/what-is-xrf-x-ray-fluorescence-and-how-does-it-work/

Ingram, B.A. and Van Tonder, D.M., 2011. *The Geology of the Broederstroom Area*. Council for Geoscience.

Keyser, A.W. and Martini, J., 1991. Haasgat: a new Plio-Pleistocene fossil occurrence. *Palaeoecology of Africa*, *21*, pp.119-129.

Keyser, AW, Menter, CG, Moggi-Cecchi, J., Rayne Pickering, P., Berger, L.R., 2000. Drimolen: a new hominid-bearing site in Gauteng, South Africa. *South African Journal of Science*, *96*(4), pp.193-197.

Kibii, J.M., Churchill, S.E., Schmid, P., Carlson, K.J., Reed, N.D., De Ruiter, D.J. and Berger, L.R., 2011. A partial pelvis of Australopithecus sediba. *Science*, *333*(6048), pp.1407-1411.

Kivell, T.L., Kibii, J.M., Churchill, S.E., Schmid, P. and Berger, L.R., 2011. Australopithecus sediba hand demonstrates mosaic evolution of locomotor and manipulative abilities. *Science*, *333*(6048), pp.1411-1417.

Kuczumow, A., Cukrowska, E., Stachniuk, A., Gawęda, R., Mroczka, R., Paszkowicz, W., Skrzypiec, K., Falkenberg, R. and Backwell, L., 2010. Investigation of chemical changes in bone material from South African fossil hominid deposits. *Journal of Archaeological Science*, *37*(1), pp.107-115.

Kuman, K. and Clarke, R.J., 2000. Stratigraphy, artefact industries and hominid associations for Sterkfontein, Member 5. *Journal of Human Evolution*, *38*(6), pp.827-847.

Kuman, K., Granger, D.E., Gibbon, R.J., Pickering, T.R., Caruana, M.V., Bruxelles, L., Clarke, R.J., Heaton, J.L., Stratford, D. and Brain, C.K., 2021. A new absolute date from Swartkrans Cave for the oldest occurrences of Paranthropus robustus and Oldowan stone tools in South Africa. *Journal of Human Evolution*, *156*, p.103000.

Lal, D., 1991. Cosmic ray labeling of erosion surfaces: in situ nuclide production rates and erosion models. Earth and Planetary Science Letters, 104(2-4), pp.424-439.

Latham, A.G., Herries, A., Quinney, P., Sinclair, A. and Kuykendall, K., 1999. The Makapansgat australopithecine site from a speleological perspective. *Geological Society, London, Special Publications*, *165*(1), pp.61-77.

Leece, A.B., Kegley, A.D., Lacruz, R.S., Herries, A.I., Hemingway, J., Kgasi, L., Potze, S. and Adams, J.W., 2016. The first hominin from the early Pleistocene paleocave of Haasgat, South Africa. *PeerJ*, *4*, p.e2024.

Li, Q., Parrish, R.R., Horstwood, M.S.A. and McArthur, J.M., 2014. U–Pb dating of cements in Mesozoic ammonites. *Chemical Geology*, *376*, pp.76-83.

Loubser, M. and Verryn, S., 2008. Combining XRF and XRD analyses and sample preparation to solve mineralogical problems. *South African Journal of Geology*, *111*(2-3), pp.229-238.

MacDonald, J.M., Faithfull, J.W., Roberts, N.M.W., Davies, A.J., Holdsworth, C.M., Newton, M., Williamson, S., Boyce, A. and John, C.M., 2019. Clumped-isotope palaeothermometry and LA-ICP-MS U–Pb dating of lava-pile hydrothermal calcite veins. *Contributions to Mineralogy and Petrology*, *174*, pp.1-15.

Makhubela, T. V., 2014. 40Ar/39Ar and (U-Th)/He dating attempts on the fossil-bearing cave deposits of the Malapa and Sterkfontein hominin sites of the Cradle of Humankind, South 29 Africa. MSc dissertation (unpublished), University of Johannesburg, P. O. Box 524, Auckland Park, Jhb, 133 pp.

Makhubela, T. V., Winkler, S. R., Mbele, V., Kramers, J. D., Khosa, R. R., Moabi, H. P., & Konyana, S. M. (2021). Development of cosmogenic nuclide capabilities in South Africa and applications in Southern African geomorphology. *South African Geographical Journal*, *103*(1), 99-118.

Makhubela, T.V. and Kramers, J.D., 2022. Testing a new combined (U, Th)–He and U/Th dating approach on Plio-Pleistocene calcite speleothems. *Quaternary Geochronology*, *67*, p.101234.

Makhubela, T.V. and Mavuso, S.S., 2022. An overview of the geology of paleoanthropological and archaeological sites of South Africa. *Integrated Quaternary Stratigraphy*, *7*, p.221.

Makhubela, T.V., Kramers, J.D., Belyanin, G.A., Dirks, P.H.G.M. and Roberts, E.M., 2017a. Proterozoic 40Ar/39Ar ages from cave deposits of the Malapa, Sterkfontein and Dinaledi fossil sites, Cradle of Humankind, South Africa. *South African Journal of Geology 2017*, *120*(1), pp.21-44.

Makhubela, T.V., Kramers, J.D., Scherler, D., Wittmann, H., Dirks, P.H.G.M. and Winkler, S.R., 2019. Effects of long soil surface residence times on apparent cosmogenic nuclide denudation rates and burial ages in the Cradle of Humankind, South Africa. *Earth Surface Processes and Landforms*, *44*(15), pp.2968-2981.

Makhubela, T.V., Kramers, J.D., Scherler, D., Wittmann, H., Dirks, P.H.G.M. and Winkler, S.R., 2017b. Cosmogenic 10BE and 26AL studies of the rising star site, Cradle of Humankind, South Africa: mystery of the true denudation rates.

Makhubela, T.V., Winkler, S.R., Mbele, V., Kramers, J.D., Khosa, R.R., Moabi, H.P. and Konyana, S.M., 2021. Development of cosmogenic nuclide capabilities in South Africa and applications in Southern African geomorphology. *South African Geographical Journal*, *103*(1), pp.99-118.

Mangenot, X., Gasparrini, M., Gerdes, A., Bonifacie, M. and Rouchon, V., 2018. An emerging thermochronometer for carbonate-bearing rocks: Δ 47/(U-Pb). *Geology*, *46*(12), pp.1067-1070.

Martin, J.M., Leece, A.B., Neubauer, S., Baker, S.E., Mongle, C.S., Boschian, G., Schwartz, G.T., Smith, A.L., Ledogar, J.A., Strait, D.S. and Herries, A.I., 2021. Drimolen cranium DNH 155 documents microevolution in an early hominin species. *Nature Ecology & Evolution*, *5*(1), pp.38-45.

Martini, J.E., Wipplinger, P.E., Moen, H.F. and Keyser, A., 2003. Contribution to the speleology of sterkfontein cave, Gauteng Province, South Africa. *International Journal of Speleology*, *32*(1), p.4.

Menter, C.G., Kuykendall, K.L., Keyser, A.W. and Conroy, G.C., 1999. First record of hominid teeth from the Plio-Pleistocene site of Gondolin, South Africa. *Journal of Human Evolution*, *37*(2), pp.299-307.

Merchel, S., & Herpers, U. (1999). An update on radiochemical separation techniques for the determination of long-lived radionuclides via accelerator mass spectrometry. *Radiochimica acta*, *84*(4), 215-220.

Methner, K., Mulch, A., Fiebig, J., Wacker, U., Gerdes, A., Graham, S.A. and Chamberlain, C.P., 2016. Rapid middle Eocene temperature change in western North America. *Earth and Planetary Science Letters*, *450*, pp.132-139.

Meyer, F.M. and Robb, L.J., 1996. The geochemistry of black shales from the Chuniespoort Group, Transvaal sequence, eastern Transvaal, South Africa. *Economic Geology*, *91*(1), pp.111-121.

Michaud, D. (2015) Sample preparation for XRF Application. Available at: https://www.911metallurgist.com/blog/sample-preparation-methods-for-xrf-analysis (Accessed: 25/06/2022)

Murszewski, A., Boschian, G. and Herries, A.I., 2020. Complexities of assessing palaeocave stratigraphy: reconstructing site formation of the~ 2.61 Ma Drimolen Makondo fossil site. *PeerJ*, *8*, p.e10360.

Murszewski, A., Edwards, T.R., Cruden, A.R., Armstrong, B., Boschian, G. and Herries, A.I., 2019. Regional geological formation and speleogenesis of the 'Fossil Hominid Sites of South Africa'UNESCO World Heritage Site. *Earth-Science Reviews*, *188*, pp.498-513.

Nayak, P.S. and Singh, B.K., 2007. Instrumental characterization of clay by FTIR, XRF, BET and TPD-NH3. *Bull. Mater. Sci.*, *30*, pp.235-238.

Nhauro, G., 2010. *Characterization of the elemental deposits in fossils from the Cradle of Humankind in South Africa and modern bones from the same geological area* (Doctoral dissertation, University of the Witwatersrand).

Nicholson, S.L., Pike, A.W., Hosfield, R., Roberts, N., Sahy, D., Woodhead, J., Cheng, H., Edwards, R.L., Affolter, S., Leuenberger, M. and Burns, S.J., 2020. Pluvial periods in Southern Arabia over the last 1.1 million-years. *Quaternary Science Reviews*, *229*, p.106112.

Nuriel, P., Craddock, J., Kylander-Clark, A.R., Uysal, I.T., Karabacak, V., Dirik, R.K., Hacker, B.R. and Weinberger, R., 2019. Reactivation history of the North Anatolian fault zone based on calcite age-strain analyses. *Geology*, *47*(5), pp.465-469.

Nuriel, P., Weinberger, R., Kylander-Clark, A.R.C., Hacker, B.R. and Craddock, J.P., 2017. The onset of the Dead Sea transform based on calcite age-strain analyses. *Geology*, *45*(7), pp.587-590.

O'Connor, S., Barham, A., Aplin, K. and Maloney, T., 2017. Cave stratigraphies and cave breccias: Implications for sediment accumulation and removal models and interpreting the record of human occupation. *Journal of Archaeological Science*, *77*, pp.143-159.

Obbes, A.M. (1995). The structure, stratigraphy and sedimentology of the Black Reef-Malmani-Rooihoogte succession of the Transvaal Supergroup South-West of Pretoria. M.Sc. diss. (unpublished), Rand Afrikaans Univ., Johannesburg, South Africa, 137 pp.

Obbes, A.M., 2000. *The structure, stratigraphy and sedimentology of the Black Reef-Malmani-Rooihoogte succession of the Transvaal Supergroup southwest of Pretoria* (Vol. 127). Pretoria: Council for Geoscience.

palaeoclimate studies. International Journal of Speleology, 44 (1), 1-16, Tampa FL (USA)

Parrish, R., 2014. Uranium–lead dating. In *Encyclopedia of scientific dating methods*. Springer.

Parrish, R., 2015. Early Life on Earth. in WJ Rink & J Thompson (eds), Encyclopedia of Scientific Dating Methods. Springer, The Netherlands, pp. 848-856. https://doi.org/10.1007/978-94-007-6326-5_256-3

Parrish, R.R., Parrish, C.M. and Lasalle, S., 2018. Vein calcite dating reveals Pyrenean orogen as cause of Paleogene deformation in southern England. *Journal of the Geological Society*, *175*(3), pp.425-442.

Partridge, T.C. and Watt, I.B., 1991. The stratigraphy of the Sterkfontein hominid deposit and its relationship to the underground cave system. *Palaeontologia africana*, *28*, pp.35-40.

Partridge, T.C., 1978. Re-appraisal of lithostratigraphy of Sterkfontein hominid site. *Nature*, *275*, pp.282-287.

Partridge, T.C., 1978. Re-appraisal of lithostratigraphy of Sterkfontein hominid site. *Nature*, *275*, pp.282-287.

Partridge, T.C., 1982. Some preliminary observations on the stratigraphy and sedimentology of the Kromdraai B hominid site.

Partridge, T.C., Granger, D.E., Caffee, M.W. and Clarke, R.J., 2003. Lower Pliocene hominid remains from Sterkfontein. *science*, *300*(5619), pp.607-612.

Paul, B., Woodhead, J.D. and Hergt, J., 2005. Improved in situ isotope analysis of low-Pb materials using LA-MC-ICP-MS with parallel ion counter and Faraday detection. *Journal of Analytical Atomic Spectrometry*, *20*(12), pp.1350-1357.

Pickering, R. and Edwards, T.R., 2021. Factors controlling age quality in UPb dated Plio-Pleistocene speleothems from South Africa: The good, the bad and the ugly. *Chemical Geology*, *579*, p.120364.

Pickering, R. and Herries, A.I., 2020. A new multidisciplinary age of 2.61-2.07 Ma for the Sterkfontein Member 4 australopiths. *Hominin Postcranial Remains from Sterkfontein, South Africa, 1936–1995*, pp.21-30.

Pickering, R. and Herries, A.I., 2020. A new multidisciplinary age of 2.61-2.07 Ma for the Sterkfontein Member 4 australopiths. *Hominin Postcranial Remains from Sterkfontein, South Africa, 1936–1995*, pp.21-30.

Herries, A.I., 2022. Chronology of the hominin sites of southern Africa. In *Oxford Research Encyclopedia of Anthropology*.

Pickering, R. and Herries, A.I., 2020. A new multidisciplinary age of 2.61-2.07 Ma for the Sterkfontein Member 4 australopiths. *Hominin Postcranial Remains from Sterkfontein, South Africa, 1936–1995*, pp.21-30.

Pickering, R. and Kramers, J.D., 2010. Re-appraisal of the stratigraphy and determination of new U-Pb dates for the Sterkfontein hominin site, South Africa. *Journal of Human Evolution*, *59*(1), pp.70-86.

Pickering, R., Dirks, P.H., Jinnah, Z., De Ruiter, D.J., Churchill, S.E., Herries, A.I., Woodhead, J.D., Hellstrom, J.C. and Berger, L.R., 2011a. Australopithecus sediba at 1.977 Ma and implications for the origins of the genus Homo. *science*, *333*(6048), pp.1421-1423.

Pickering, R., Hancox, P.J., Lee-Thorp, J.A., Grün, R., Mortimer, G.E., McCulloch, M. and Berger, L.R., 2007. Stratigraphy, U-Th chronology, and paleoenvironments at Gladysvale Cave: insights into the climatic control of South African hominin-bearing cave deposits. *Journal of Human evolution*, *53*(5), pp.602-619.

Pickering, R., Herries, A.I., Woodhead, J.D., Hellstrom, J.C., Green, H.E., Paul, B., Ritzman, T., Strait, D.S., Schoville, B.J. and Hancox, P.J., 2019. U–Pb-dated flowstones restrict South African early hominin record to dry climate phases. *Nature*, *565*(7738), pp.226-229.

Pickering, R., Kramers, J.D., Hancox, P.J., de Ruiter, D.J. and Woodhead, J.D., 2011b. Contemporary flowstone development links early hominin bearing cave deposits in South Africa. *Earth and planetary science letters*, *306*(1-2), pp.23-32.

Pickering, R., Kramers, J.D., Partridge, T., Kodolanyi, J. and Pettke, T., 2010. U–Pb dating of calcite–aragonite layers in speleothems from hominin sites in South Africa by MC-ICP-MS. *Quaternary Geochronology*, *5*(5), pp.544-558.

Pickering, T.R., Heaton, J.L., Clarke, R.J., Sutton, M.B., Brain, C.K. and Kuman, K., 2012. New hominid fossils from Member 1 of the Swartkrans formation, South Africa. *Journal of human evolution*, *62*(5), pp.618-628.

Plug, I.* & Keyser, A., 1994. Haasgat Cave, a Pleistocene site in the central Transvaal: geomorphological, faunal and taphonomic considerations. *Annals of the Transvaal Museum*, *36*(9), pp.139-145.

Pourmand, A., Dauphas, N. and Ireland, T.J., 2012. A novel extraction chromatography and MC-ICP-MS technique for rapid analysis of REE, Sc and Y: Revising CI-chondrite and Post-Archean Australian Shale (PAAS) abundances. *Chemical Geology*, *291*, pp.38-54.

Ray, E. and Paul, D., 2021. Major and Trace Element Characteristics of the Average Indian Post-Archean Shale: Implications for Provenance, Weathering, and Depositional Environment. *ACS Earth and Space Chemistry*, *5*(5), pp.1114-1129.

Reczko, B.F.R. (1994) *The Geochemistry of the sedimentary rocks of the Pretoria Group, Transvaal sequence.* Ph. D. Thesis. University of Pretoria. Available at: https://repository.up.ac.za/handle/2263/82496?show=full (Accessed: 05 January 2013)

Reimer, T.O., 1992. Carbonaceous High-Alumina Shale in the Transvaal Supergroup: Evidence of Early Proterozoic Karstic Wheathering in a Marine Environment. *Early Organic Evolution: Implications for Mineral and Energy Resources*, pp.106-114.

Retallack, G.J., 1990. *Soils of the past: an introduction to paleopedology*. Harper Collins, London, pp. 27

Richards, D.A. and Dorale, J.A., 2003. Uranium-series chronology and environmental applications of speleothems. *Reviews in Mineralogy and Geochemistry*, *52*(1), pp.407-460.

Ring, U. and Gerdes, A., 2016. Kinematics of the Alpenrhein-Bodensee graben system in the Central Alps: Oligocene/Miocene transtension due to formation of the Western Alps arc. *Tectonics*, *35*(6), pp.1367-1391.

Robbins, J.L., Dirks, P.H., Roberts, E.M., Kramers, J.D., Makhubela, T.V., Hilbert-Wolf, H.L., Elliott, M., Wiersma, J.P., Placzek, C.J., Evans, M. and Berger, L.R., 2021. Providing context to the Homo naledi fossils: Constraints from flowstones on the age of sediment deposits in Rising Star Cave, South Africa. *Chemical Geology*, *567*, p.120108.

Roberts, N.M. and Walker, R.J., 2016. U-Pb geochronology of calcite-mineralized faults: Absolute timing of rift-related fault events on the northeast Atlantic margin. *Geology*, *44*(7), pp.531-534.

Rollinson, H.R., 1993. Using geochemical data: evaluation, presentation. *Interpretation*, *352*.

Ronov, A.B. and Migdisov, A.A., 1971. Geochemical history of the crystalline basement and the sedimentary cover of the Russian and North American platforms. *Sedimentology*, *16*(3-4), pp.137-185.

Rudnick, R.L., Gao, S., Holland, H.D. and Turekian, K.K., 2003. Composition of the continental crust. *The crust*, *3*, pp.1-64.

Rugel, G., Pavetich, S., Akhmadaliev, S., Baez, S. M. E., Scharf, A., Ziegenrücker, R., & Merchel, S. (2016). The first four years of the AMS-facility DREAMS: Status and developments for more accurate radionuclide data. *Nuclear Instruments and Methods in Physics Research Section B: Beam Interactions with Materials and Atoms*, *370*, 94-100.

Scardia, G., Parenti, F., Miggins, D.P., Gerdes, A., Araujo, A.G. and Neves, W.A., 2019. Chronologic constraints on hominin dispersal outside Africa since 2.48 Ma from the Zarqa Valley, Jordan. *Quaternary Science Reviews*, *219*, pp.1-19.

Schreiber, U. M. (1990). A palaeoenvironmental study of the Pretoria Group in the eastern Transvaal. Ph. D. thesis (unpubl.), Univ. of Pretoria, South Africa

Shaar, R., Matmon, A., Horwitz, L.K., Ebert, Y., Chazan, M., Arnold, M., Aumaître, G., Bourlès, D. and Keddadouche, K., 2021. Magnetostratigraphy and cosmogenic dating of Wonderwerk Cave: New constraints for the chronology of the South African Earlier Stone Age. *Quaternary Science Reviews*, *259*, p.106907.

South African Council for Stratigraphy (SACS). 1980. Stratigraphy of South Africa, Part 1. Lithostratigraphy of the Republic of South Africa, South West Africa/Namibia and the Republics of Bophuthatswana, Transkei and Venda (L.E. Kent, Compiler): Handbook Geol. Surv. S. Afr., 8,690 p

Springer, G. S., 2005. Clastic sediments in caves. In: Culver, D. & White, W. (eds), Encyclopedia of Caves. Elsevier Academic Press, Burlington, San Diego, London, pp. 102–108.

Springer, G. S., 2012. Clastic sediments in caves. In: White, William B & Culver, D. C. (Eds). *Encyclopedia of Caves* (2nd edition, p. 963). Amsterdam: Elsevier, Academic press.

Steininger, C., Berger, L.R. and Kuhn, B.F., 2008. A partial skull of Paranthropus robustus from Cooper's Cave, South Africa. *South African Journal of Science*, *104*(3), pp.143-146.

Stock, G.M., Granger, D.E., Sasowsky, I.D., Anderson, R.S. and Finkel, R.C., 2005. Comparison of U–Th, paleomagnetism, and cosmogenic burial methods for dating caves: implications for landscape evolution studies. *Earth and Planetary Science Letters*, *236*(1-2), pp.388-403.

Stratford, D., Grab, S. and Pickering, T.R., 2014. The stratigraphy and formation history of fossil-and artefact-bearing sediments in the Milner Hall, Sterkfontein Cave, South Africa: New interpretations and implications for palaeoanthropology and archaeology. *Journal of African Earth Sciences*, *96*, pp.155-167.

Sumner, D.Y. and Beukes, N.J., 2006. Sequence stratigraphic development of the Neoarchean Transvaal carbonate platform, Kaapvaal Craton, South Africa. *South African Journal of Geology*, *109*(1-2), pp.11-22.

Susman, R.L., de Ruiter, D. and Brain, C.K., 2001. Recently identified postcranial remains of Paranthropus and early Homo from Swartkrans Cave, South Africa. *Journal of Human Evolution*, *41*(6), pp.607-629.

Sutton, M.B., Pickering, T.R., Pickering, R., Brain, C.K., Clarke, R.J., Heaton, J.L. and Kuman, K., 2009. Newly discovered fossil-and artifact-bearing deposits, uranium-series ages, and Plio-Pleistocene hominids at Swartkrans Cave, South Africa. *Journal of Human Evolution*, *57*(6), pp.688-696.

Taylor, S.R. and McLennan, S.M., 1985. The continental crust: its composition and evolution.

Thackeray, J.F., Kirschvink, J.L. and Raub, T.D., 2002. Palaeomagnetic analyses of calcified deposits from the Plio-Pleistocene hominid site of Kromdraai, South Africa: news & views. *South African Journal of Science*, *98*(11), pp.537-540.

Tucker, M.E. and Jones, S.J., 2023. *Sedimentary petrology*. John Wiley & Sons.

Walker, J., Cliff, R.A. and Latham, A.G., 2006. U-Pb isotopic age of the StW 573 hominid from Sterkfontein, South Africa. *Science*, *314*(5805), pp.1592-1594.

Walter, B.F., Gerdes, A., Kleinhanns, I.C., Dunkl, I., von Eynatten, H., Kreissl, S. and Markl, G., 2018. The connection between hydrothermal fluids, mineralization, tectonics and magmatism in a

continental rift setting: Fluorite Sm-Nd and hematite and carbonates U-Pb geochronology from the Rhinegraben in SW Germany. *Geochimica et Cosmochimica Acta*, *240*, pp.11-42.

White, W. B., 2007. Cave sediments and paleoclimate. Journal of Cave and Karst Studies, 69: 76–93.

White, W.B., 2012. Speleothems: General Overview. *Encyclopedia of Caves*, pp.777-786.

White, W.B., 2019. Speleothems. In *Encyclopedia of caves* (pp. 1006-1017). Academic Press.

Wiersma, J.P., Roberts, E.M. and Dirks, P.H., 2020. Formation of mud clast breccias and the process of sedimentary autobrecciation in the hominin-bearing (Homo naledi) Rising Star Cave system, South Africa. *Sedimentology*, *67*(2), pp.897-919.

Williams, S.A., Ostrofsky, K.R., Frater, N., Churchill, S.E., Schmid, P. and Berger, L.R., 2013. The vertebral column of Australopithecus sediba. *Science*, *340*(6129), p.1232996.

Woodhead, J. and Petrus, J., 2019. Exploring the advantages and limitations of in situ U–Pb carbonate geochronology using speleothems. *Geochronology*, *1*(1), pp.69-84.

Woodhead, J., Hellstrom, J., Maas, R., Drysdale, R., Zanchetta, G., Devine, P. and Taylor, E., 2006. U–Pb geochronology of speleothems by MC-ICPMS. *Quaternary Geochronology*, *1*(3), pp.208-221.

Woodhead, J., Hellstrom, J., Pickering, R., Drysdale, R., Paul, B. and Bajo, P., 2012. U and Pb variability in older speleothems and strategies for their chronology. *Quaternary Geochronology*, *14*, pp.105-113.

Yokoyama, T., Kimura, J.I., Mitsuguchi, T., Danhara, T., Hirata, T., Sakata, S., Iwano, H., Maruyama, S., Chang, Q., Miyazaki, T. and Murakami, H., 2018. U-Pb dating of calcite using LA-ICP-MS: Instrumental setup for non-matrix-matched age dating and determination of analytical areas using elemental imaging. *Geochemical Journal*, *52*(6), pp.531-540.

Zipfel, B., DeSilva, J.M., Kidd, R.S., Carlson, K.J., Churchill, S.E. and Berger, L.R., 2011. The foot and ankle of Australopithecus sediba. *Science*, *333*(6048), pp.1417-1420.\

ANNEXURES

Annexure A: Analytical protocol for U-Pb-LA-ICP-MS at Wits

Prepared by Robert Bolhar, date: May 2021

Flowstone samples were prepared as polished fragments embedded in epoxy resin mounts. Petrographic examination did not reveal any distinct calcite types and generation or obvious alteration. U-Th-Pb measurements were carried out in the Earthlab at the University of the Witwatersrand, employing an Applied Spectra (formerly Australian Scientific Instruments) Resonetics Resolution 193 nm ArF excimer (SE 155) system coupled to a Thermo Scientific Fisher sector-field ICPMS (Element XR). The U-Th-Pb measurements were performed in low resolution and electrostatic scanning (E-scan) modes. Data were acquired by single spot analysis (100 □m), using a laser repetition rate of 15 Hz and a fluence of 2 Jcm^{-2}. Total signal acquisition time was 40 seconds, allowing data processing and preparation for the next analysis, and comprising two times 5 seconds of pre- and post-ablation (gas blank) and 30 seconds of ablation measurements. Laser sampling took place in a dual-volume ablation cell (Laurin Technic, Canberra, Australia) using a mixed He-Ar atmosphere and a small volume of N_2 to enhance signal stability and sensitivity. The following gas flows were applied: He (350 ml/min), Ar (1050 ml/min) and N_2 (5 ml/min), respectively. Carbonate standard WC-1 (254 Ma; Roberts et al., 2017) served for primary calibration (Woodhead and Petrus, 2019), and Duff Brown limestone, Richard's Spur speleothem and Rio calcite were analyzed as unknown to evaluate accuracy and precision (Hill et al., 2016; Woodhead et al., 2010; Cris Lana, pers. communication). The LA-ICPMS system was optimized during line scans using NIST 612 glass for maximum sensitivity for ^{238}U and ^{206}Pb, while

maintaining oxide levels (ThO^+/Th) <0.15 % and the Th/U ratio >0.95. The primary calibration standard was analyzed at the beginning and end of each sequence, and 30-40 analyses of unknowns were followed by analyses of one primary calibration standard and the secondary standard for quality control purposes. Prior to each spot analysis surface material was removed using 2 laser pulses. The following masses were measured (six samples per peak): ^{206}Pb, ^{207}Pb, ^{208}Pb, ^{232}Th, and ^{238}U. Magnet settling time was 0.001 sec, and sample times range from 0.001 sec (^{232}Th) to 0.005 sec (^{207}Pb). All isotopes were measured in pulse counting mode, except for ^{238}U (analogue or counting mode).

Data reduction was performed using the iolite extension to the software Igor Pro, proceeding in a series of sequential steps, including data import, selection of integrations, baseline subtraction, drift and down-hole fractionation, calibration and error propagation (Paton et al., 2010, 2011). Additionally, the data reduction schemes (DRS) VizualAge and UncomPbine (Petrus and Kamber, 2012) were applied to more carefully select portions of the time-resolved signal within samples with variable $^{238}U/^{206}Pb$ ratios, and to enable correction of variable common lead of the primary standard WC-1, using the ^{207}Pb-based approach (Chew et al., 2014).

Graphic presentation and calculation of lower intercept ages on a Tera-Wasserburg diagram were carried out using the software ISOPLOT-R (Vermeesch, 2018). Uncertainties of individual and mean/regressed ages are 2 SE (standard error, absolute). Intercept ages were based on individual dates and internal errors (not propagated), excluding obvious outliers. Propagated errors on U/Pb ratios can be estimated to be 1.25 times the internal errors for a similar analytical setup as adopted here (Woodhead and Petrus, 2019).

Depth-resolution within each analysis is enabled by using a primary carbonate standard (WC-1), coupled with downhole-fractionation correction; this further allowed to identify (and

exclude) regions of high common Pb and also to separate time intervals with distinctly variable U/Pb during ablations, sometimes resulting in more than one date for each spot (Woodhead and Petrus, 2019), reflecting age heterogeneity or variable common Pb within the carbonate.

References for the protocols

Chew, D.M., Petrus, J.A. and Kamber, B.S., 2014. U–Pb LA–ICPMS dating using accessory mineral standards with variable common Pb. *Chemical Geology*, *363*, pp.185-199.

Hill, C.A., Polyak, V.J., Asmerom, Y. and P. Provencio, P., 2016. Constraints on a Late Cretaceous uplift, denudation, and incision of the Grand Canyon region, southwestern Colorado Plateau, USA, from U-Pb dating of lacustrine limestone. *Tectonics*, *35*(4), pp.896-906.

Petrus, J.A. and Kamber, B.S., 2012. VizualAge: A novel approach to laser ablation ICP-MS U-Pb geochronology data reduction. *Geostandards and Geoanalytical Research*, *36*(3), pp.247-270.

Roberts, N.M., Rasbury, E.T., Parrish, R.R., Smith, C.J., Horstwood, M.S. and Condon, D.J., 2017. A calcite reference material for LA-ICP-MS U-Pb geochronology. *Geochemistry, Geophysics, Geosystems*, *18*(7), pp.2807-2814.

Vermeesch, P., 2018. IsoplotR: A free and open toolbox for geochronology. *Geoscience Frontiers*, *9*(5), pp.1479-1493.

Woodhead, J. and Petrus, J., 2019. Exploring the advantages and limitations of in situ U–Pb carbonate geochronology using speleothems. *Geochronology*, *1*(1), pp.69-84.

Woodhead, J., Reisz, R., Fox, D., Drysdale, R., Hellstrom, J., Maas, R., Cheng, H. and Edwards, R.L., 2010. Speleothem climate records from deep time? Exploring the potential with an example from the Permian. *Geology*, *38*(5), pp.455-458.

Annexure B: Harker diagram data format

	Al2O3	CaO	Fe2O3	K2O	MgO	MnO	P2O5	SiO2	TiO2
MLP1P	**1.01**	**48.5**	**0.82**	**0.08**	**0.61**	**0.35**	**-**	**9.49**	**0.1**
MLP14P	**3.65**	**29.74**	**3.42**	**0.22**	**0.91**	**1.56**	**0.63**	**33.97**	**0.25**
MLP2P	**2.63**	**38.37**	**2.52**	**0.17**	**0.46**	**1.61**	**-**	**22.29**	**0.22**
MLP3P	**2.79**	**36.44**	**2.27**	**0.2**	**0.48**	**0.99**	**-**	**26.37**	**0.23**
MLP7P	**2.99**	**30.02**	**2.49**	**0.2**	**0.53**	**1.15**	**-**	**36.98**	**0.24**
MLP12P	**1.73**	**38.31**	**2.4**	**0.14**	**6.96**	**2**	**-**	**10.21**	**0.13**
MLP9P	**3.27**	**32.37**	**2.96**	**0.2**	**0.71**	**1.6**	**-**	**29.67**	**0.25**
MLP4P	**3.98**	**28.57**	**3.32**	**0.25**	**0.56**	**1.38**	**0.1**	**36.06**	**0.28**
MLP5P	**2.93**	**42.15**	**2.48**	**0.16**	**0.48**	**0.83**	**0.22**	**15.99**	**0.2**
MLP6P	**3.43**	**35.45**	**2.99**	**0.22**	**0.59**	**1.42**	**0.16**	**24.85**	**0.24**

MLP8P	**1.77**	**26.14**	**2.25**	**0.1**	**0.37**	**1.34**	**-**	**45.68**	**0.13**
MLP10P	**4.01**	**27.61**	**3.97**	**0.24**	**0.58**	**1.72**	**-**	**38.62**	**0.32**
MLP11P	**3.22**	**32.86**	**3.44**	**0.21**	**0.81**	**3.09**	**-**	**27.93**	**0.23**
MLP13P	**3.28**	**34.09**	**3.24**	**0.21**	**1.82**	**1.94**	**-**	**25.07**	**0.25**
UCC	**15.4**	**3.59**	**5.61**	**2.8**	**2.48**	**0.1**	**0.15**	**66.6**	**0.64**
NASC	**16.9**	**3.63**	**6.3**	**3.97**	**2.86**	**0.06**	**0.13**	**64.8**	**0.7**
PAAS	**18.9**	**1.3**	**7.24**	**3.7**	**2.2**	**0.11**	**0.16**	**62.8**	**1**
CSW	**17.02**	**3.44**	**6.71**	**3.58**	**2.7**	**0.5**	**0.19**	**64.21**	**0.72**
AEPS	**8.71**	**1.45**	**3.21**	**1.3**	**1.65**	**0.04**	**0.05**	**78.81**	**0.28**
ALPS	**9.79**	**1.37**	**4.9**	**2.94**	**1.67**	**0.09**	**0.07**	**72.78**	**0.56**
SHALE	**15.4**	**3.1**	**4.02**	**3.24**	**2.44**	**0**	**0.17**	**58.11**	**0.65**
SANDSTONE	**4.76**	**5.5**	**1.08**	**1.32**	**1.16**	**0**	**0.08**	**78.31**	**0.25**
LIMESTONE	**0.81**	**42.57**	**0.54**	**0.33**	**7.89**	**0.05**	**0.04**	**5.19**	**0.06**
CSMG	**21.47**	**0.4**	**0.96**	**6.19**	**1.57**	**0.03**	**0.03**	**61.14**	**1.14**
PGS	**19.07**	**2.71**	**7.68**	**3.58**	**3.1**	**0.05**	**0.16**	**62.37**	**0.64**
BSCG	**14.69**	**2.49**	**3.15**	**7.07**	**3.86**	**0.08**	**0.1**	**60.43**	**0.57**